AUTOMATED VISUAL INSPECTION

OF GENERAL CURVATURE SURFACES

USING MOIRÉ INTERFEROMETRY

by

Eric P. Reidemeister

(B.S.M.E.) Worcester Polytechnic Institute (1986)

Submitted to the Department of
Mechanical Engineering
in partial fulfillment of the
requirements for the degree of

MASTER OF SCIENCE
IN MECHANICAL ENGINEERING

at the

MASSACHUSETTS INSTITUTE OF TECHNOLOGY

August 1988

Signature of Author_____
Department of Mechanical Engineering
August 1988

Certified by_____
Steven Dubowsky
Thesis Advisor

Accepted by_____
Ain A. Sonin
Chairman, Department Graduate Committee

Automated Visual Inspection of General Curvature Surfaces Using Moiré Interferometry

by

Eric P. Reidemeister

ABSTRACT

Automated inspection is a growing concern in industry. The combination of design and manufacturing processes seen in the engineering community should include inspection processes as well. One such inspection process, projection Moiré interferometry, has shown a great deal of promise due to its flexibility in the inspection of surface form. The technique uses the interference of two high frequency grids to detect surface errors. In past research, projection Moiré techniques have been developed to inspect faceted objects utilizing the mathematical concept of equiorder surfaces. Optimization routines have been implemented to tailor these equiorder surfaces for particular inspections.

New methods of tailoring equiorder surfaces were developed with this research. The projection Moiré technique was extended to inspection of surfaces with a general curvature. Specifically, a new method utilizing spline representations of the grid lines was developed in order to increase the flexibility of the projection Moiré technique. Theoretical and experimental results with this method are presented.

Results indicate that the technique developed is a feasible method of inspecting surfaces with a general curvature. Several surfaces were successfully inspected including cylinders, flat objects, and surfaces similar to a compressor airfoil. The work showed a few drawbacks to the projection Moiré method, namely the ability to align the inspection grids and calibrate the interferometer.

Thesis Supervisor : Dr. Steven Dubowsky
Title : Professor of Mechanical Engineering

ACKNOWLEDGEMENTS

I would like to thank my thesis advisor Dr. Steven Dubowsky for his guidance with this research. Many thanks to Annie Murray for her assistance with the subject matter. I would also like to thank Digital Equipment Corporation for the financial support and the Laboratory for Manufacturing and Productivity at MIT for the research space.

Thanks to my family and to friendly snoshes. Lastly, I give thanks to Miky for being there and providing support for me throughout my graduate studies.

TABLE OF CONTENTS

LIST OF FIGURES

1 INTRODUCTION

1.1 Background

Automated inspection is a growing concern in industry and it is currently recognized that ideally the designs of a product, its manufacturing system, and its inspection processes should be integrated in a rational manner. Decisions made in the design stage affect the manufacturing and inspection of a product [8]. Specifically, the inspection technique for an object should be specified as part of its description. Lack of proper inspection techniques increases the chance of obtaining lower quality products and inefficient assembly processes. Also, many inspection tasks are still done manually and in an obtrusive manner. In the shift towards automating inspection processes, it is important to outline the goals of an ideal inspection. An ideal inspection process is:

(1) 100% reliable;
(2) 100% accurate;
(3) inexpensive;
(4) not requisite of skilled labor;
(5) high speed;
(6) flexible, having the ability to inspect different objects at different times;
(7) full-field, having the ability to inspect a complete object at one time;
(8) integrated with other production stages;
(9) a monitor for other production processes;
(10) unobtrusive, to avoid sensor wear and part damage.

The focus of this work is on the inspection of three-dimensional surface form of objects. In the past, many methods of inspection have been developed including visual and nonvisual techniques. Some of the limits of these techniques are the requirements for extensive computer processing time and complex electronics. A promising method of surface form inspection which approaches an ideal inspection process without many limitations is Moiré interferometry. Moiré interferometry has been around for a long time and in the past has been used for inspection of faceted objects and objects with a single curvature [24,27]. My work has extended the projection Moiré technique to include inspection of surfaces with a general curvature. The next few sections will give a brief background of some inspection techniques and how I have extended the projection Moiré technique.

1.2 Methods of Inspection

Current methods of non-contact surface inspection include techniques which utilize sound chambers, lasers, and vision systems. Of the visual inspection techniques presented, optical ranging will be outlined and Moiré interferometry will be presented in detail; of the non-visual techniques, an ultrasonic method and a thermal method will be presented.

Ultrasonic nondestructive testing methods utilize high frequency dynamics to detect defects in castings, forgings, and welds. Defects are spotted by sensing echoes and recording the time of flight of vibrations. Other industrial applications of ultrasonic object inspection are object thickness monitoring, corrosion detection, adhesive bond monitoring, and material characterization. Ultrasonic object inspection is a method suited for finding small defects because the wavelength used for testing is approximately equal to defect size. In general, as the size of the defect becomes smaller, the frequency of the testing device used for a particular inspection increases[41].

Another nonvisual technique called *thermal nondestructive testing* measures temperature variations on surfaces to detect flaws. Internal defects, bonds in laminate, etc., can be detected using this method. The method is best suited for plastics as opposed to metals because the temperature gradient can be easily monitored[41]. This describes just a few of the inspection techniques used today. For the study of surface form, these techniques would be inappropriate.

Optical ranging is a visual technique in which a beam (a point or line) of laser light is projected onto an object. The time of reflection of this beam is measured and the process continues over the whole object to construct a three-dimensional image by piecing together the two-dimensional coordinates [38]. Measuring the transit time of the laser light in optical ranging is difficult and the time of inspection increases with the number of points or lines of an object that are analyzed. Other vision-based inspection systems have been discussed in the literature [2,15].

1.3 Moiré Interferometry

The focus of this study is *Moiré interferometry*. The word Moiré (pronounced "mwah ray") is a french word meaning 'watered'. It is a reference to a fabric patterning technique→

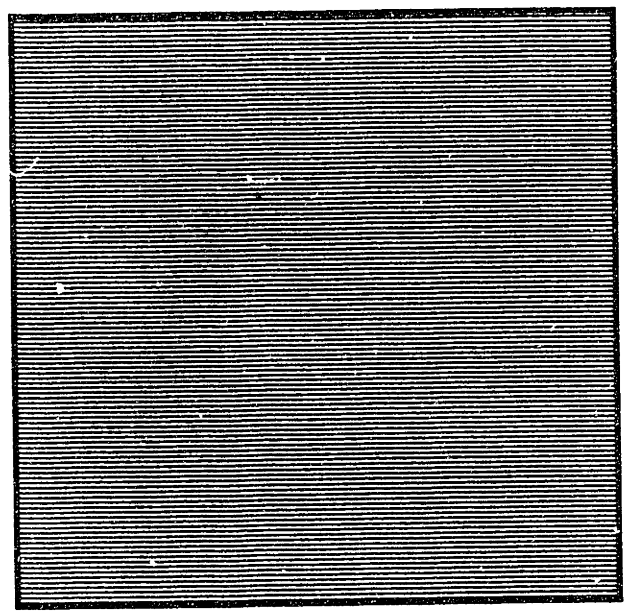

Figure 1.1: Projection Moiré Interference Pattern - Viewing Grid

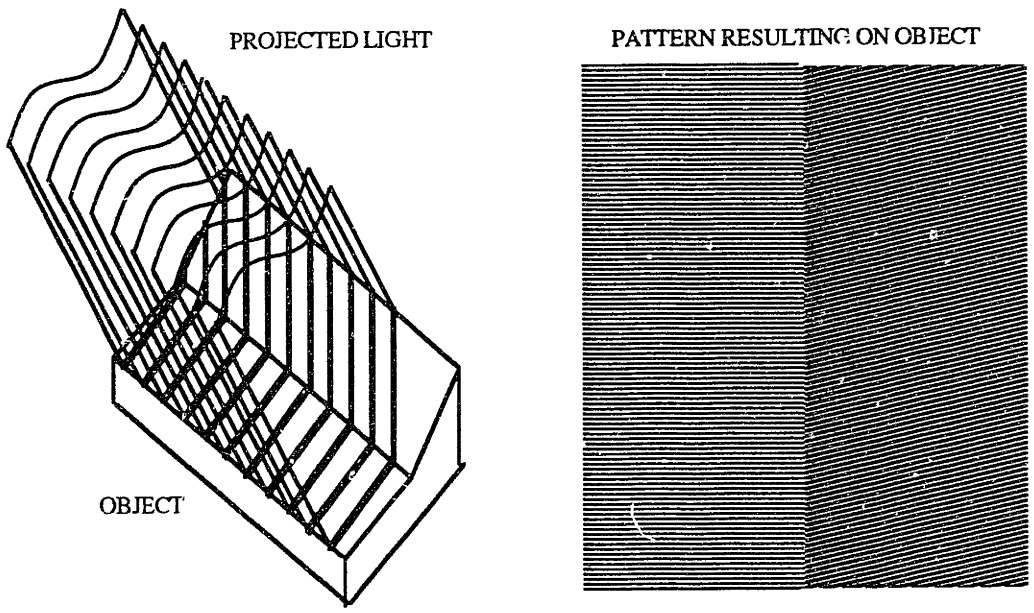

Figure 1.2: Projection Moiré Interference Pattern - Projection Grid

in use for centuries. More than one hundred years ago, in 1874, British scientist Lord Rayleigh first suggested the use of Moiré patterns as a simple and precise way to test the accuracy of manufactured materials [25]. A Moiré pattern is a low frequency line image produced from two high frequency line images or grids. These patterns can be seen in everyday places such as curtains, playground fences, and referees' shirts on television [12]. By projecting a high frequency grid onto an object and viewing the reflection of this projected pattern through another high frequency grid, Moiré interferometry can be used to measure surface form and surface errors [31]. The Moiré patterns that result from the interference of the two grids can be mathematically analyzed and used to design a specific inspection process. Several authors have discussed the use of Moiré interferometry for object inspection [5,6,8,11-14,16,18-22,24,25,27,29,31,33,37,38,40-43].

By placing the transparent grid pattern, Figure 1.1, over the image of Figure 1.2 (the pattern resulting from projecting a grid onto an object), the details of the object become evident in the display of low frequency fringe patterns. In this way, the grid pattern of Figure 1.1 is used as an interpreting grid to distinguish surface form. This interpretation will be used later in Chapter 4 to develop the inspection method.

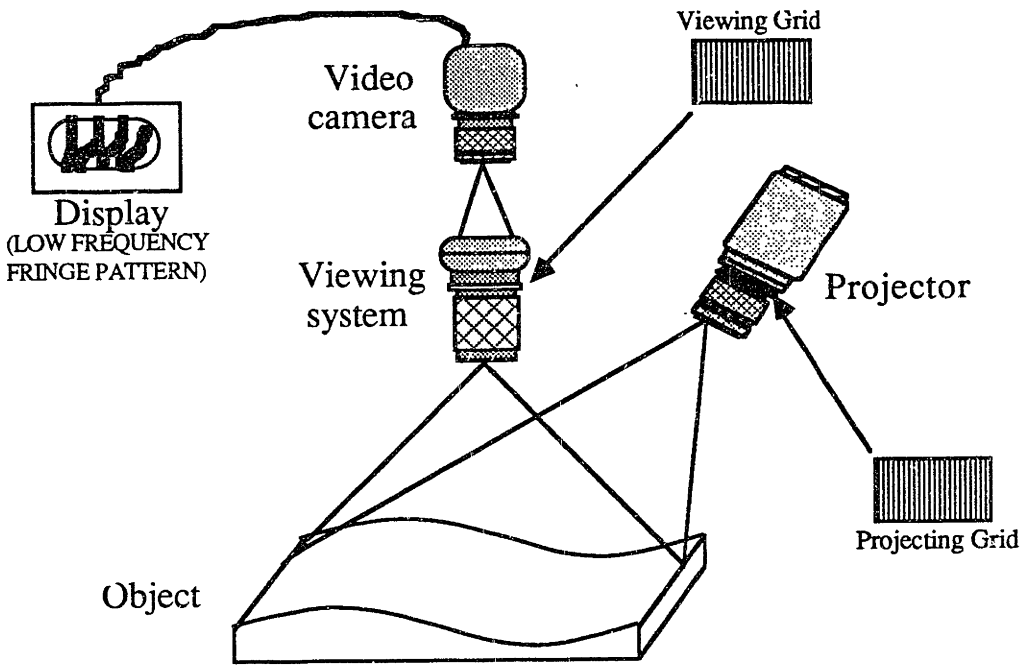

Figure 1.3: Projection Moiré Interferometer

One of the unique advantages of Moiré interferometry is the ability to change the Moiré patterns to modify an inspection process for different objects. This modification is accomplished by adjusting the grid lines, thus producing a different fringe pattern. In this way, Moiré interferometry is quite flexible. Of greater impact is the ability of the grids to be modified to produce no fringes for a properly toleranced object, thus reducing the visual data processing time for the inspection. Another advantage of Moiré interferometry is that great changes occur in the observed fringe patterns with even the slightest object deviation. Thus, the interference of the grid lines acts as an optical lever arm for a more accurate inspection [14].

Current literature shows that extensive research is being undertaken in Moiré methods of object inspection. Below are some of the techniques researchers have utilized to inspect objects:

(1) *projection Moiré* - projecting a grid onto an object and viewing the reflected image through another grid [13,37];

(2) *Moiré gauging or subtraction Moiré* - projecting a grid onto a properly toleranced object and using the photograph of this image in the image plane as the viewing grid. An improperly toleranced object will generate fringes and be rejected [5,31];

(3) *shadow Moiré* - projecting light through a large grid in order to produce a shadow onto the object and then viewing the reflected image through a small grid [16];

(4) *scanning Moiré* - electronic scanning and sampling technique in which there is no reference grating. Interference is produced electronically by storing reflected images [16].

Of these techniques, projection Moiré is the most flexible [31]. The technique offers the ability to use small optical gratings, allowing flexibility in the choice of grid line pitch, orientation, and magnification. The technique produces fringes which are sensitive to the desired object inspection tolerances [20]. Moiré gauging is similar to projection Moiré, but relies on precise photography. Shadow Moiré requires a grid as large as the object being inspected. Scanning Moiré requires more complex electronic equipment and greater time in data processing [20].

Research at M.I.T. has concentrated on the design of inspection processes using the projection Moiré technique. Wander developed a model for analyzing Moiré inspection and experimentally verified the technique [42]. Leonard created CAD simulations of Moiré patterns [20]. Sullivan produced a feasibility study of the projection Moiré technique [40].

The difficulty of distinguishing good and bad objects, particularly planar objects, was then addressed. Murray furthered this early work by designing a technique based on Wander's analytical work and Leonard's concept of tailoreded grids [27]. Working with the idea that a properly toleranced object produces no fringe pattern, Murray developed an optimization routine and inspected planar surfaces and faceted cylinders theoretically utilizing straight-lined grid patterns. Some discontinuities, discussed later, resulted in her inspection technique. Moens furthered the work of Murray by developing an experimental setup and tailoring grids to perform inspection on vertically faceted, single curvature surfaces [24]. As with Murray's work, Moens' work contained discontinuities that limited the technique. In the past, only straight-lined grids have been used to inspect faceted objects and objects with a single curvature. My work has extended the projection Moiré technique by utilizing curved grid lines allowing flexibility in the inspection of surfaces with a general curvature.

1.4 Thesis Overview

Through my work, the tailoring of object inspection has been extended to inspection of objects with a general curvature by using grids composed of cubic polynomials or splines . The technique developed with this work measures errors in surface form, not small cracks or minute perturbations. Aside from the techniques' accuracy and flexibility, the technique is well suited for the design/manufacturing environment, since utilization of object characteristics is intrinsic.

The goal of my research was to inspect objects with general curvatures (i.e. turbine blade). This goal was achieved by utilizing Murray's basic design method and some of Moens' refined programming. I also sought to find a feasible way to produce the grids for inspection and to test the theories using the experimental setup.

The fundamental discussion of the mathematical concepts behind the projection Moiré technique are examined in Chapter 2. Chapter 3 contains methods of manipulating the grid lines which were considered in this thesis. Chapter 4 develops a method of inspection tailoring, the Method of Splines, in detail. Chapter 5 contains the theoretical results in inspecting various objects. Chapter 6 contains details of the experimental setup, the testing results, and the practical considerations for producing a viable inspection system.

2 THE PROJECTION MOIRÉ TECHNIQUE

2.1 General Technique

Projection Moiré Interferometry is a physical phenomena which can be described mathematically. The mathematics have been detailed in previous theses, therefore, the mathematical equations from those theses will only be touched upon here, to describe the overall method. References should be made to Wander, Leonard, Murray, and Moens for more details [20,24,27,42].

The projection Moiré technique utilizes the interference of light in a predictable manner to inspect objects. Through the work in this thesis, it will be shown that if the desired interference pattern for a specific object is known, then the inspection grids can be made to suit this goal. Specifically, the interference pattern of interest in this work is a pattern with no dark fringes on the image plane. If this pattern is produced, the inspection system is then said to be 'tailored' to a specific object. This tailoring is accomplished through the use of the concepts of fringe order and equiorder surface discussed here.

2.2 Concept of Fringe Order

The projecting and viewing grid system setup is shown in Figure 2.1 where

S_p = Projection focal length,

S_v = Viewing focal length,

ζ = Projection to viewing axis angle,

(0,0,0) = Center of optical system,

(x_{po},y_{po},z_{po}) = Center of projecting system,

(x,y,z) = System coordinates,

(x',y',z') = Projecting system coordinates,

(x_p,y_p) = Projecting grid axes,

(x_v,y_v) = Viewing grids axes.

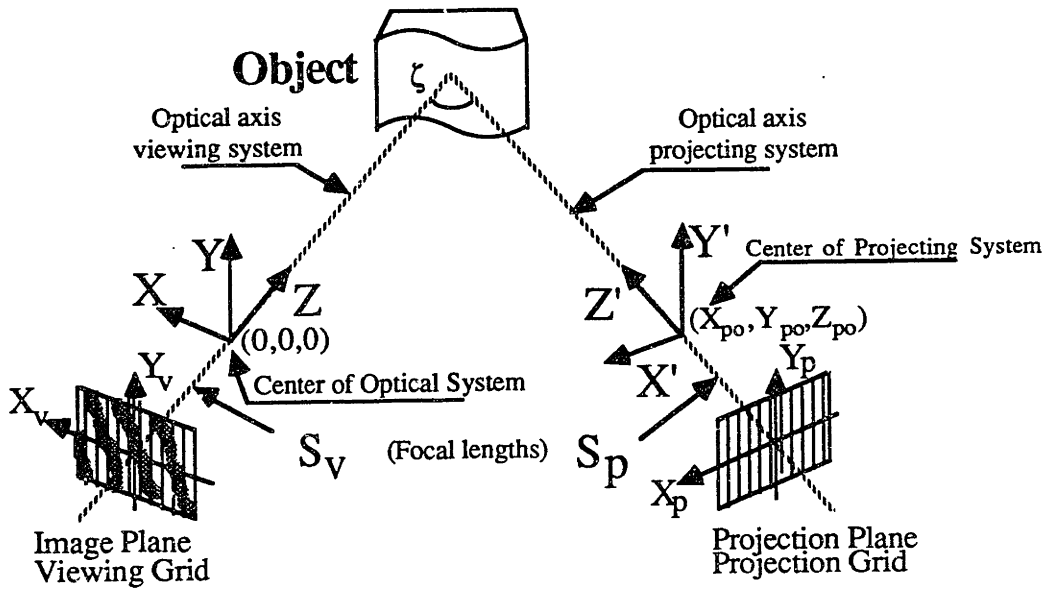

Figure 2.1: Projection Moiré Physical System Setup

The geometry of straight-lined, parallel, equally-spaced grids in this system can be described by three parameters: the grid angle (α), the grid pitch (P), and the grid phase (ϕ) [42]. The angle of the grid lines, as seen in Figure 2.2, is the grid line angle with respect to a local coordinate system measured from the vertical direction. The grid line pitch is defined in this work as twice the line thickness. The phase corresponds to the distance the zero numbered grid line is away from the grid center. In past work, only grids made up of straight lines or line segments have been used. The analysis for these straight-lined grids is presented here with my extension to curved grid lines appearing in Chapter 4.

The *fringe order* (FO) is defined as the difference between viewing grid line number and projecting grid line number,

$$FO = n_v - n_p \tag{2.1}$$

where n_v is the number associated with the dark lines in the viewing grid and n_p is the number associated with the dark lines of the projection grid. The projected grid image reflects off of an object and intersects the viewing image at the image plane of the system. At this intersection, or where each of the numbered grid lines intersects, the fringe order

can be calculated. The dark grid lines have a grid line number equal to an integer while the light grid lines have a grid line number equal to an *integer* ± 0.5. The fringe order is the number that corresponds to the observed fringes on the image plane of the inspection system. Using this numbering scheme, dark fringes will be observed on the image plane when an object intersects with points where the fringe order is equal to an *integer* ± 0.5. In other words, dark fringes occur when a dark projection line intersects with a light viewing line. This fact will be used in the inspection grid optimization in Chapter 4.

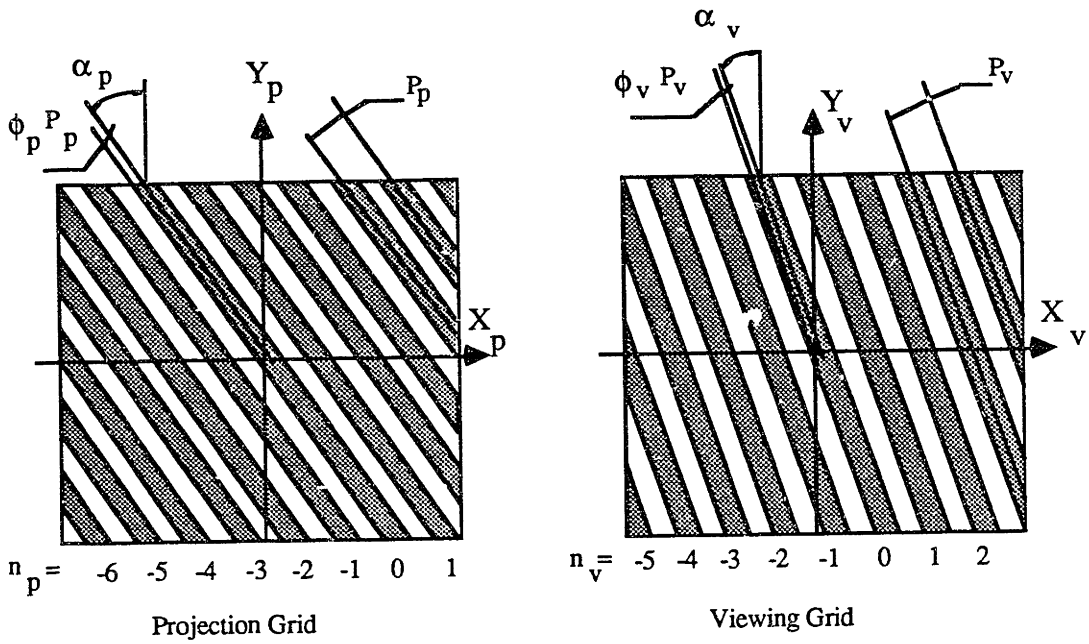

Figure 2.2: Projection and Viewing Grids

2.3 Concept of Equiorder Surface

The projection of the numbered grid lines in space forms imaginary surfaces. The connection of the intersection points in which the fringe orders are equal forms an *equiorder surface*. Figure 2.3 shows the formation of equiorder surfaces. Following from the fringe order concept, if the equiorder surface with a fringe order value equal to an *integer* ± 0.5 intersects with the object under inspection, dark fringes will be observed on the image plane.

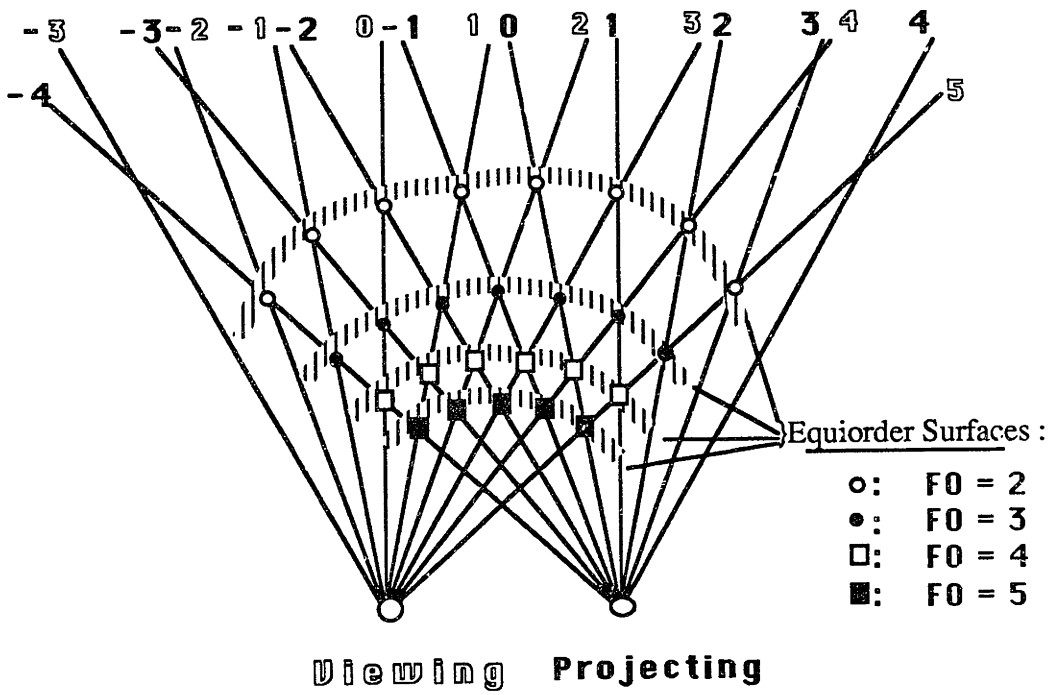

Figure 2.3: Equiorder Surface Development

2.4 Calculation of Fringe Order Using the Equiorder Surface Equation

In order to calculate the fringe order, the equations for the grid line numbers which correspond to the two grids must be derived as a function of the x and y grid positions. The geometry of each grid is described in Figure 2.2. From Moens, the grid line numbers as a function of grid position can be written as

$$n_v = \frac{x_v \cos\alpha_v + y_v \sin\alpha_v}{P_v} - \phi_v \tag{2.2}$$

$$n_p = \frac{x_p \cos\alpha_p + y_p \sin\alpha_p}{P_p} - \phi_p \tag{2.3}$$

where

$$x_v = -S_v\left(\frac{x}{z}\right) \tag{2.4}$$

$$y_v = -S_v\left(\frac{y}{z}\right) \tag{2.5}$$

$$x_p = -S_p\left(\frac{x'}{z'}\right) \tag{2.6}$$

$$y_p = -S_p\left(\frac{y'}{z'}\right) \tag{2.7}$$

are the x and y grid positions with respect to viewing and projecting grid axes respectively [24].

Based on the the transformation described in Wander, and combining the above equations, the equation for the equiorder surface is

$$w(x,y,z) = Ax^2 + By^2 + Cz^2 + Dxy + Eyz + Fxz + Gx + Hy + Iz = 0 \tag{2.8}$$

where

$$A = S_v P_p \sin\zeta\cos\alpha_v \tag{2.8a}$$

$$B = 0.0 \tag{2.8b}$$

$$C = P_v P_p (FO + \phi_v - \phi_p)\cos\zeta + S_p P_v \sin\zeta\cos\alpha_p \tag{2.8c}$$

$$D = S_v P_p \sin\zeta\sin\alpha_v \tag{2.8d}$$

$$E = S_v P_p \cos\zeta\sin\alpha_v - S_p P_v \sin\alpha_p \tag{2.8e}$$

$$F = P_v P_p (FO + \phi_v - \phi_p)\sin\zeta + S_v P_p \cos\zeta\cos\alpha_v - S_p P_v \cos\zeta\cos\alpha_p \tag{2.8f}$$

$$G = -S_v P_p (x_{po}\sin\zeta + z_{po}\cos\zeta)\cos\alpha_v \tag{2.8g}$$

$$H = -S_v P_p (x_{po}\sin\zeta + z_{po}\cos\zeta)\sin\alpha_v \tag{2.8h}$$

$$I = -P_v P_p (x_{po}\sin\zeta + z_{po}\cos\zeta)(FO + \phi_v - \phi_p) + S_p P_v (x_{po}\cos\zeta - z_{po}\sin\zeta)\cos\alpha_p \tag{2.8i}$$

Solving for fringe order at a point in object space (x,y,z),

$$FO = \frac{\begin{pmatrix} -Ax^2 - Dxy - Eyz - Gx - Hy - S_pP_vN\cos\alpha_p z \\ -S_pP_v\sin\zeta z^2 - (P_pS_v\cos\alpha_v - S_pP_v\cos\alpha_p)\cos\zeta xz \end{pmatrix}}{P_vP_p(-Mz + \cos\zeta z^2 + \sin\zeta xz)} \tag{2.9}$$

where $$M = x_{po}\sin\zeta + z_{po}\cos\zeta \tag{2.9a}$$

and $$N = x_{po}\cos\zeta - z_{po}\sin\zeta. \tag{2.9b}$$

This corresponds to the fringe order at a point in the object space based on the interferometer geometry and the grid parameters of Figure 2.1 [24,42].

2.5 Inspection Method

By using the concepts of fringe order and equiorder surface, this analysis shows that the surfaces of objects can be inspected based on the fringe pattern observed on the image plane of the system. A fringe pattern can be changed and analyzed by adjusting the grid parameters. By knowing the mathematical basis for the resulting fringe patterns described here, inspection without dark fringes can be achieved resulting in minimal computation of inspection images. Because dark fringes on the image plane occur when there is an equiorder surface of order *integer ± 0.5* intersecting with the object being inspected, forcing the equiorder surfaces associated with these fringe orders to surround the object results in no dark fringes on the image plane and, hence, a properly toleranced object is inspected. If an improperly toleranced object is placed in the system, the same equiorder surfaces will intersect the object and dark fringes will be produced on the image plane. The equiorder surfaces are said to be tailored for a given object when the image plane shows no dark fringes. This tailoring is the main goal of my work. Tailoring of equiorder surfaces is examined in Chapter 3.

3 TAILORED EQUIORDER SURFACES

3.1 Principles of Tailored Equiorder Surfaces

The tolerance of the inspection is met by spacing the equiorder surfaces appropriately to completely surround an object [27]. The object under inspection is required to be situated between equiorder surfaces of fringe order equal to an *integer* ± 0.5 so that no dark fringes appear on the image plane of the system. This is done by 'tailoring' the equiorder surfaces for a given object. By simple visual detection the projection Moiré inspection system measures the error in the surface form of objects [24]. In other words, the system is suitable for comparing the shape of different objects, e.g. measuring the difference in surface profile between a product specimen and a master object.

The equiorder surface equation (2.8) was derived from straight, parallel, equally-spaced lines [27]. Note that this same equiorder surface equation can be used with patches of straight grid lines, as discussed in Murray and in Moens. My work uses the same equation with curved grid lines, and the tailoring of the equiorder surfaces begins by manipulating the curved grid lines. The difficulty in deriving the same equiorder surface equation from curved grid lines is too great. The equiorder surface equation is valid at a point, and, thus, a discrete approach is taken. In Chapter 4, my method of tailoring will be presented.

3.2 Tailoring Methods

In general, the tailoring methods followed at M.I.T. have taken a two step form, interferometer optimization and grid optimization. The interferometer optimization comes from the work of Murray and Moens, and remains unchanged [24,27]. The interferometer optimization program takes as input the object data and physical interferometer parameters. The object in this optimization is a flat plate in which there is one patch, the seed patch. By adjusting the physical parameters and seed patch location, the parameters are optimized and the physical setup of the inspection is checked for feasibility. The grid optimization program, the central point of my work, tailors the equiorder surfaces for a specific object. The program also serves in the generation of the equiorder surface plots and of the grid plots. My grid optimization program will be discussed in Chapter 4.

The interferometer setup used for this research is the same throughout this work. Below are the interferometer parameters:

Tolerance of inspection	= TOL = 10 mm (5 mm on each side of object);
Projection focal length	= S_p= 135 mm;
Viewing focal length	= S_v= 135 mm;
Object location at center	= (x,y,z) = (0 mm,0 mm,567.5 mm);
Projector location	= (x´,y´,z´) = (-147.5 mm, 0 mm, -50.0 mm);
Projector angle	= ζ = .25 radians;
Projection grid pitch	= P_p = .50 mm;
Viewing grid pitch	= P_v = .58 mm.

3.2.1 Previous Tailoring Methods

The tailoring method of Murray utilized object characteristics and interferometer geometry, combined with grid properties, to optimize the inspection system [27]. From the grid line angle, pitch, and phase, a number of grid patches were mapped into equiorder surface elements. These surface elements were compared to object facets, and the differences in the two resulted in Murray's cost function. The cost function was a comparison of the spacing of equiorder surfaces and their angles to the object angle and its positioning. The equiorder surfaces were tailored by changing the standard Moiré parameters of angle, pitch, and phase. Murray found that by changing the grid line angles, the equiorder surfaces could be rotated about the x and y axes [27]. Also, the spacing of the equiorder surfaces could be changed by changing the pitch of the grid line. Changing the grid line phase translates the equiorder surfaces in the z direction. These three parameters offer enough flexibility to manipulate the equiorder surfaces in any way. A flowchart of her conceptual plan is in Figure 3.1.

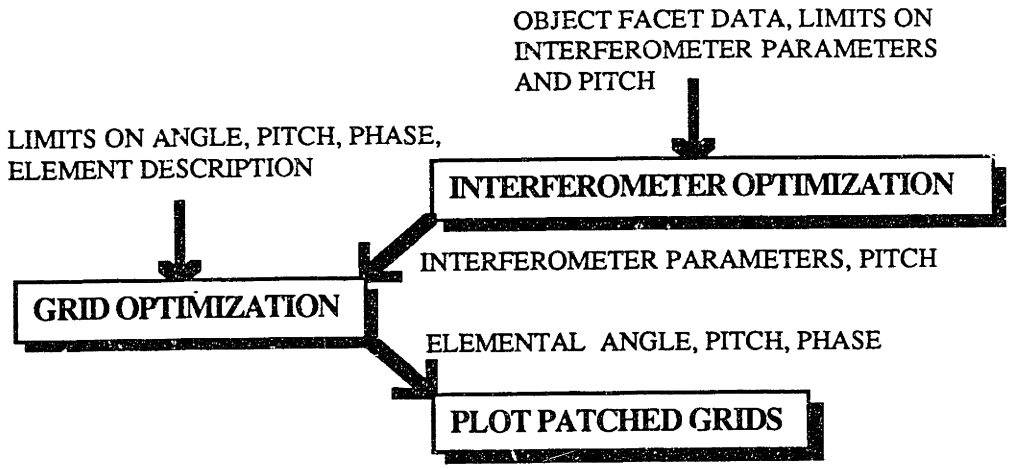

Figure 3.1: Murray - Conceptual Plan

Curved equiorder surfaces are needed to inspect curved surfaces. Curved equiorder surfaces can be obtained from curved grid patterns. Murray used a series of object facets and broke the total grid into patches [27]. These patches are shown in Figure 3.2. In order to match the object with greater detail, the grids were broken down (see Figure 3.3 in which a cylindrical object made up of 89 facets has been optimized). The patches enabled the global grid lines to curve resulting in curved equiorder surfaces. See Figure 3.4. The grid parameters in each patch were optimized for independently and discontinuities occured between grid lines in succesive patches. The local angle of the grid lines in these patches did not match the global grid line angle. In other words, the discontinuities resulted in high frequency changes in grid line angles which failed with the low frequency Moiré phenomena.

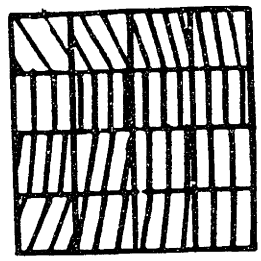

VIEWING
GRID

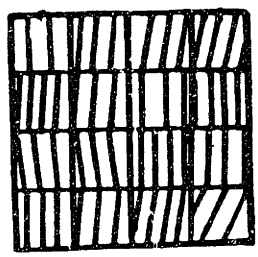

PROJECTING
GRID

Figure 3.2: Murray - Grid Patches

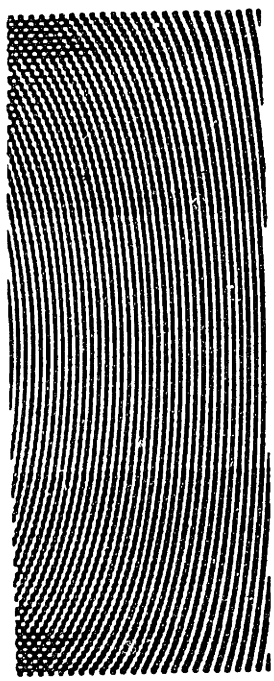

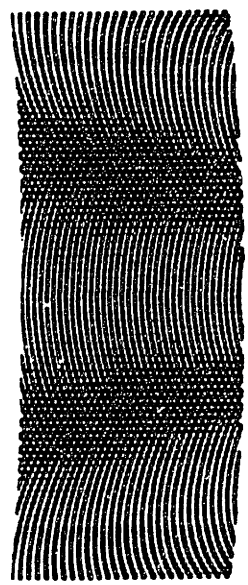

a. Viewing Grid.

b. Projecting Grid.

Figure 3.3: Murray - Discontinuous Patches

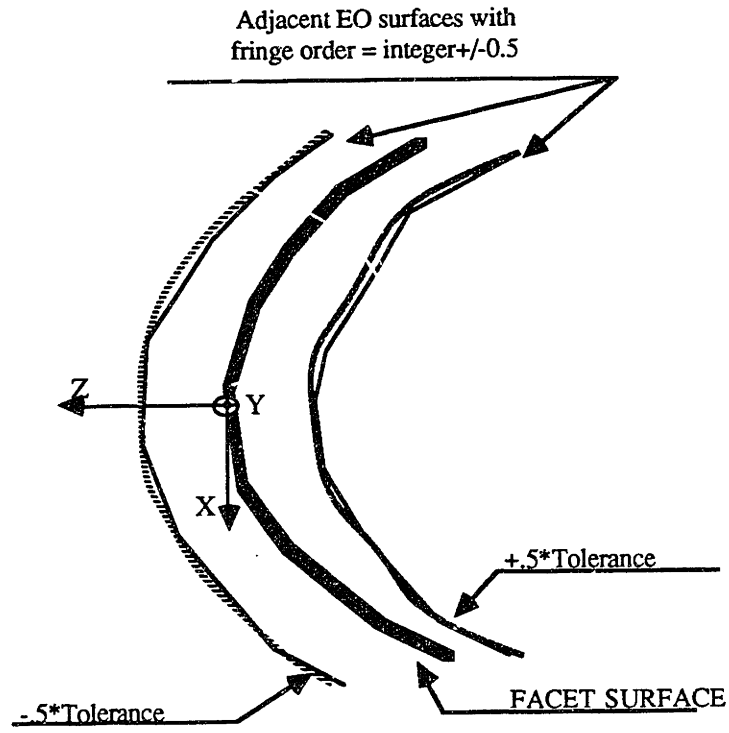

Figure 3.4: Equiorder Surface/Object Matching

Moens' approach was similar. Figure 3.5 shows Moens conceptual plan utilizing a patch approach as well (see Figure 3.6). There were no longer any discontinuities from patch to patch because his patches were not optimized for independently [24]. Optimization occured vertically from patch to patch. Since his optimization was limited to surfaces with a constant cross section (curvature in one direction only), he needed only vertical patches. He found that, by using grid patches composed of straight lines, the equiorder surfaces were able to match neither flat objects, unless a special geometry existed, nor curved surfaces. For instance, when inspecting a cylinder, the grid optimization only performed well at a cross-section through the center point of the facets of the cylinder. There were dark fringes produced from equiorder surface/object interference at other spots along the cylinder. There was a lack of flexibility in tailoring the equiorder surfaces with Moens' approach. The next few sections describe some potential new approaches of equiorder surface tailoring for grid optimization.

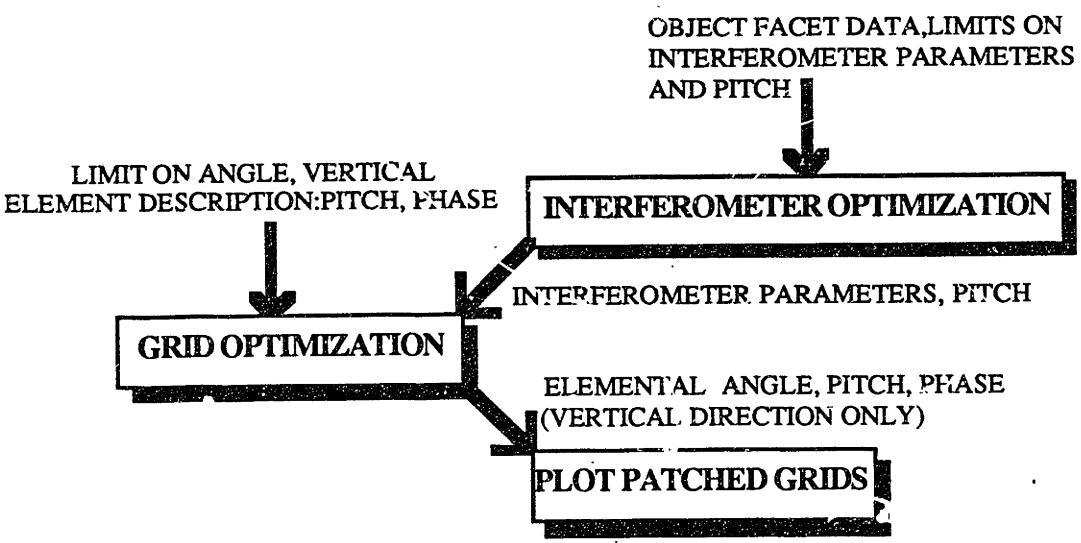

Figure 3.5: Moens - Conceptual Plan

3.2.2 Two-Dimensional Optimization

The first attempt at optimizing the grids dealt with Moens' method of patch to patch optimization; his ideas was modified, the intent being an improvement upon Murray's angle discontinuities in grids and also upon Moens' lack of flexibility in matching the equiorder surfaces to an object. The feasibility of optimizing object tolerances to equiorder surfaces surrounding an object using grids that were composed of patches of equally-spaced straight lines extending vertically *and* horizontally was investigated. Figure 3.7 shows equiorder surface tailoring by two-dimensional optimization.

A general configuration (shown in Figure 3.7) was analysed in detail. This configuration represents only one two-by-two portion of a globally patched grid, but the feasibility can be checked with this subsection. The setup of Figure 3.7 differs from that of Moens' because the grid patch parameters were optimized in a two-dimensional grid. Moens optimized for the grid patch angles, and pitch and phase were calculated based on patch to patch correspondence. The setup of Figure 3.7 can be analyzed first by placing grid lines in patch #1 at angle α_1 and extending them into patches #2 and #3 at arbitrary

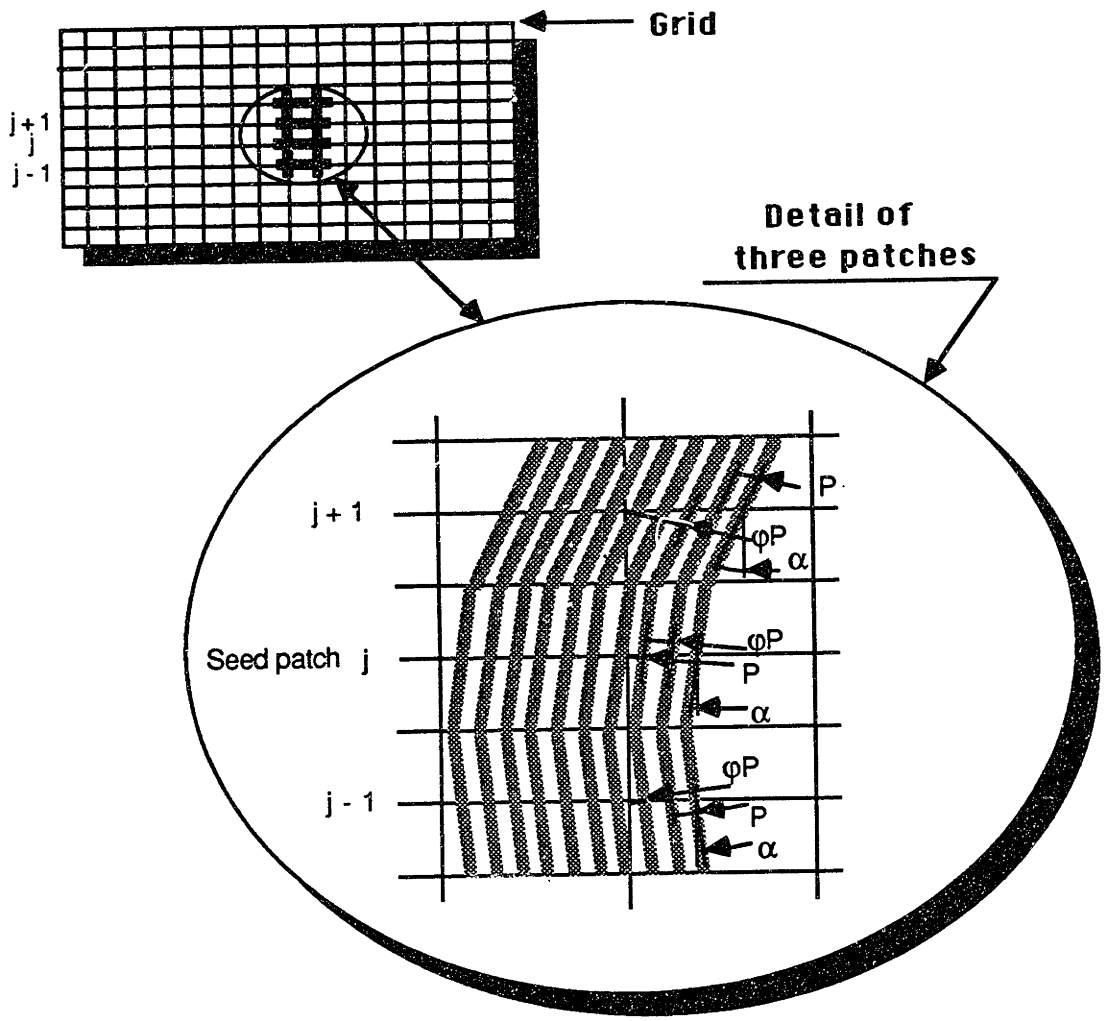

Figure 3.6: Moens - Grid Patches

angles α_2 and α_3 respectively. Grid patch angles for patches #2 and #3 can be optimized from knowledge of object characteristics and the equiorder surface equation [24]. Pitches P_2 and P_3 as well as phases ϕ_2 and ϕ_3 can be calculated from the angles [24]. To determine is the grid angle of patch #4 is predetermined, the following analysis must be performed.

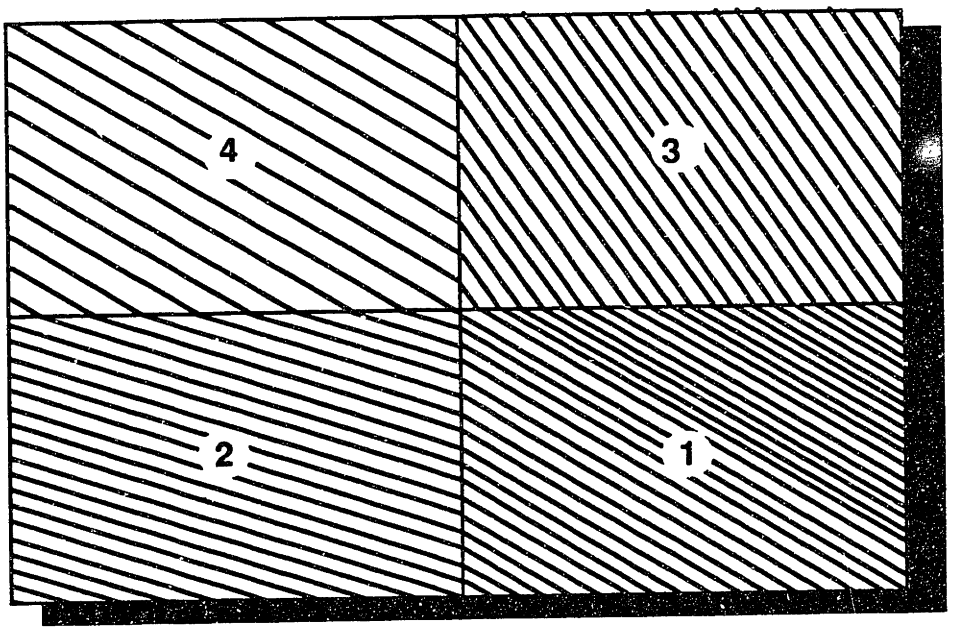

Figure 3.7: Equiorder Surface Tailoring - Two-Dimensional Optimization

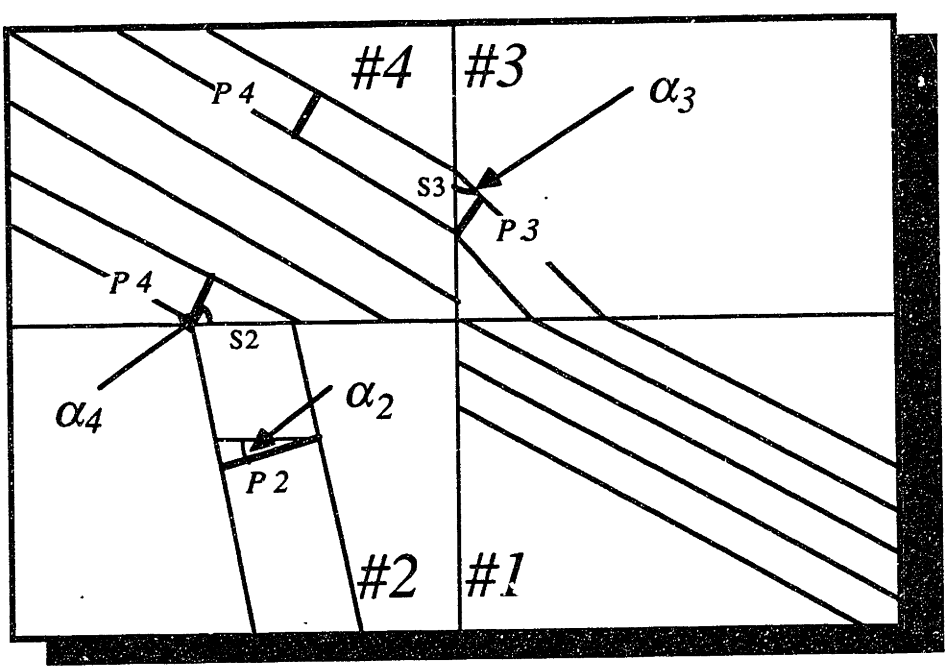

Figure 3.8: Boundary Configuration - Two-Dimensional Optimization

From Figure 3.8, it can be shown with simple geometry that

$$\alpha_4 = \tan^{-1}\left(\frac{P_2 \sin\alpha_3}{P_3 \cos\alpha_2}\right) \tag{3.1}$$

and

$$P_4 = \frac{P_2 \cos\alpha_4}{\cos\alpha_2}. \tag{3.2}$$

All terms on the right side of equation 3.1 are already known. Thus, the angle of patch #4 cannot be optimized.

Hence, it is clear that only one solution exists for grid patch parameters of patch #4. Therefore, no optimization can occur between patches #2 and #3, and patch #4. That is, this approach would not be adequate for tailoring the equiorder surfaces. The equiorder surface is predetermined in patches where the grid line angle is not variable.

3.2.3 Finite Patched Grid Optimization

Another method to attack the grid development problem is depicted in Figure 3.9. The 'Finite Patched Grid' borrows concepts from finite element analysis in establishing boundary conditions for each side of each patch in the total grid. Slope matching and spacing continuity at the edge of each patch would be preserved for a grid of patches composed of continuous grid lines. This method was forgone because of the high number of boundary conditions to satisfy and because of the limitations observed on the previous optimization methods.

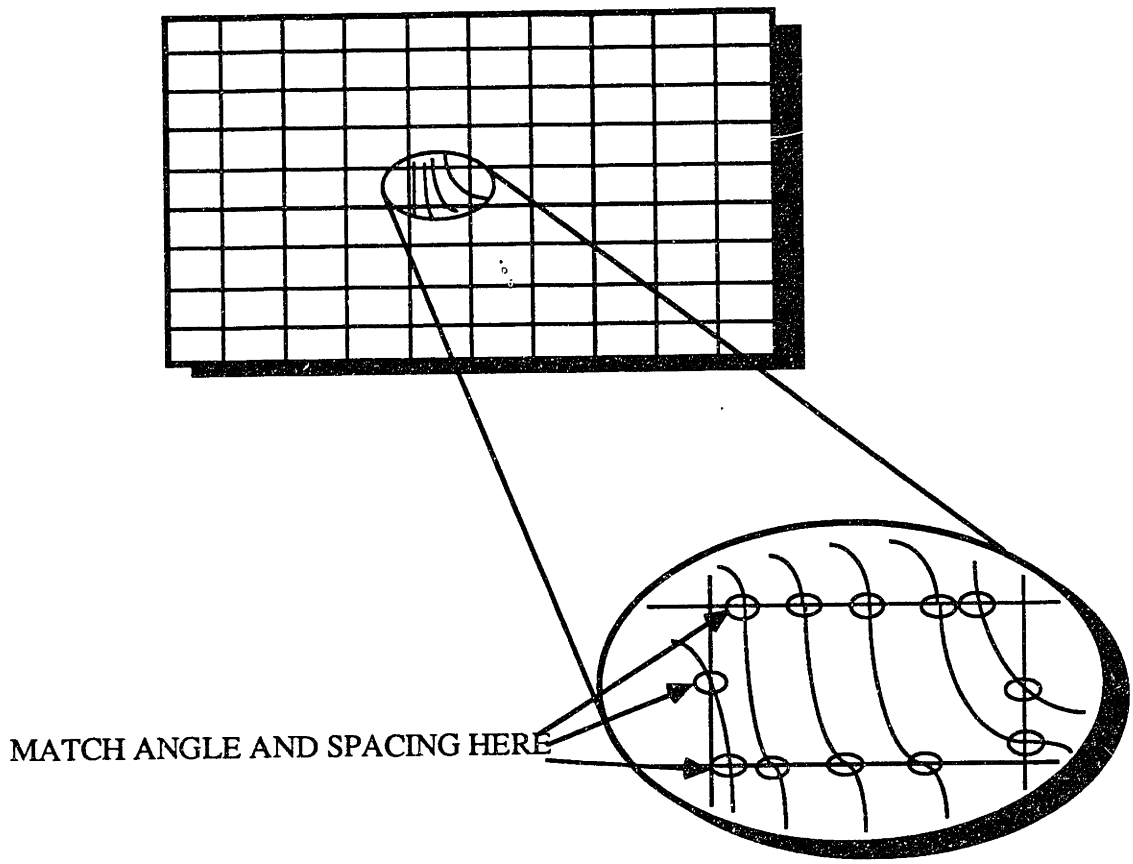

Figure 3.9: Equiorder Surface Tailoring - Finite Patched Grid

3.2.4 Global Parameterized Curves

The Global Parameterized Curve Method resolves the problem of angle discontinuities by using continuous grid lines over single, global grid (Figure 3.10). The parameters of several curves are optimized to obtain the correct equiorder surface tailoring. Because the number of parameters, N, to decribe such a curve can be tremendously large, a topographical method is employed in which the complexity of the optimization is reduced. The topographical method breaks the global grid into a small number of principal curves which are in turn optimized. From these principal curves, similar filling curves are derived by interpolating between the principal curves. In this way, a total grid is completely mapped for inspection purposes with the advantage of relatively few parameters necessitating optimization. This method will allow the minimization of the equiorder

surface to object toloerance error with a practical amount of computational effort. This method will be described in Chapter 4.

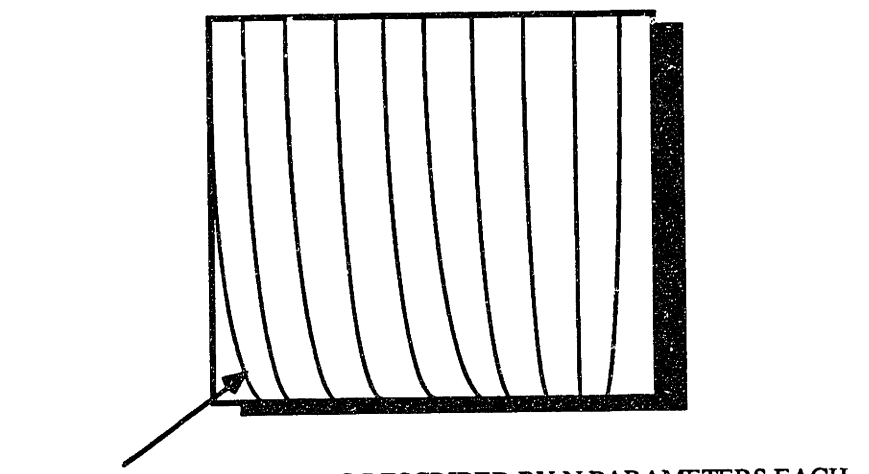

Figure 3.10: Equiorder Surface Tailoring - Global Parameterized Curves

4 METHOD OF SPLINES

4.1 Introduction

The Global Parameterized Curve Method, described in Section 3.2.4, was adopted as the method of optimizing the grids. The methods of Murray and Moens were investigated with the intent of implementing slight curves to the grid lines in place of the existing patches of straight lines [24,27]. Matching any surface contour with an equiorder surface requires high flexibility in grid curve generation. Also, transfering the chosen curve parameters to standard Moiré parameters of grid angle, pitch, and phase is necessary to utilize the equation of the equiorder surface (2.8). These conditions suggested the use of Bézier splines as the basic curve in generating grid patterns.

Because computation time is a critical aspect of inspection, a small number of object evaluation points were chosen to constitute the cost function. To evaluate a cost function at each point along a spline would require a great deal of computer time. *Sixteen* object evaluation points corresponding to sixteen viewing and projecting grid evaluation points were chosen. Figure 4.1 shows the object evaluation points for a typical object, in this case a flat plate. Note also that the results in Chapter 5 will show four cross-sections of each object. The cross-sections occur at the four y values shown. Three principal splines

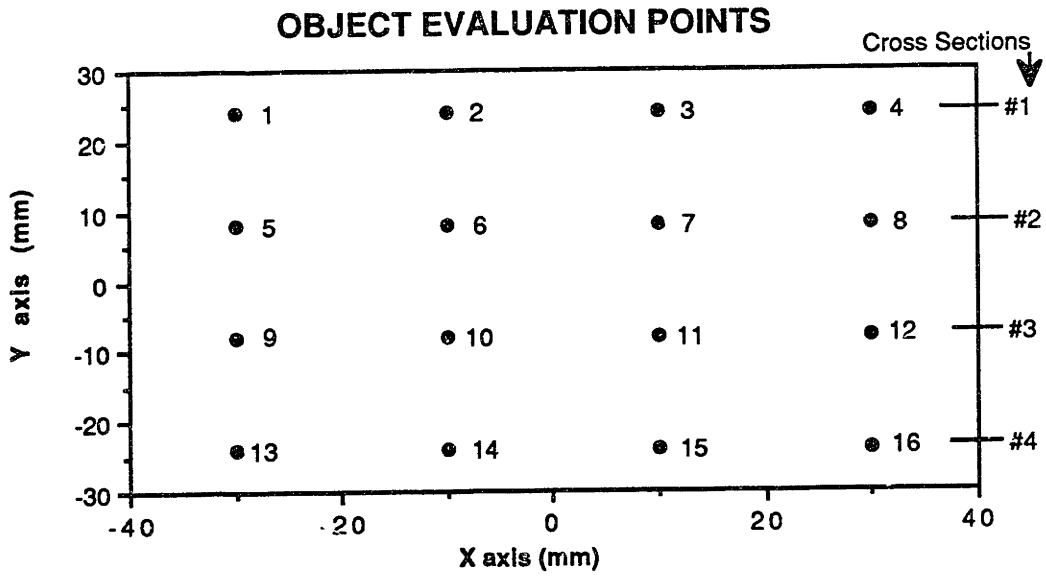

Figure 4.1: Object Evaluation Regions

were chosen as the basis of the grid due to computational constraints. Each spline is described by four control points (x,y). These control points define the inspection grid. They are allowed to vary until an optimal grid setup is found. The optimization routine is described later in this chapter. The x values of the control points of these three splines are the optimized parameters in the grid optimization program. The 24 x values of these control points correspond to the x values of 12 control points from each grid. Restricting optimization to only x values was a result of the optimization routine having an upper limit of 30 optimized parameters. The effects of allowing only the x values of the control points to move was checked (the y values were constant). Note that there is no flexibility lost in determining the standard Moiré parameters when only the x values of the control points were allowed to move rather than x and y. From the three principal splines, filling splines are generated by linearly interpolating between spline control points (Figure 4.2). Once the optimization is complete, the curved grids are generated by inputting the control points and plotting the splines.

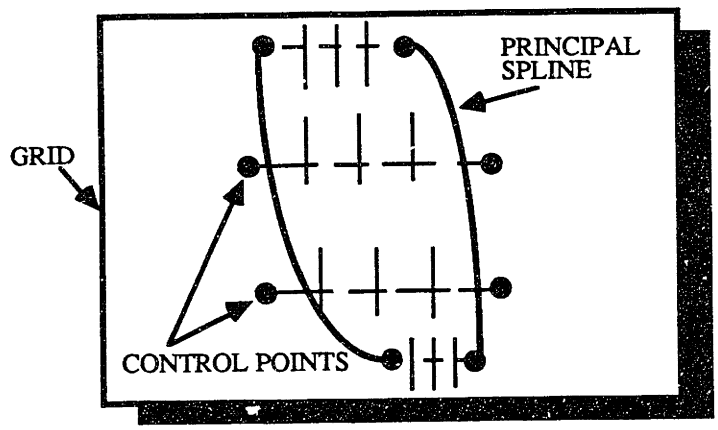

Figure 4.2: Linear Interpolation Between Principal Spline Control Points

The Method of Splines consist of a conversion of spline parameters (control points) to standard straight-lined Moiré parameters (angle, pitch, and phase) at various points along the curved grid lines. The equation of the equiorder surface (2.8) is used in this analysis

for curved grid lines at discrete points with those points taking on the characteristics of straight lines. Summarizing the constraints that were placed on the method:

(1) the object was not faceted, but was continuously curved;
(2) a grid without patches was used;
(3) splines were used to generate the projecting and viewing grids;
(4) sixteen object (and grid) evaluation points were chosen;
and (5) the overall cost function was the sum of the sixteen evaluated cost functions (described later).

Figure 4.3 shows the program flow chart for the method of splines.

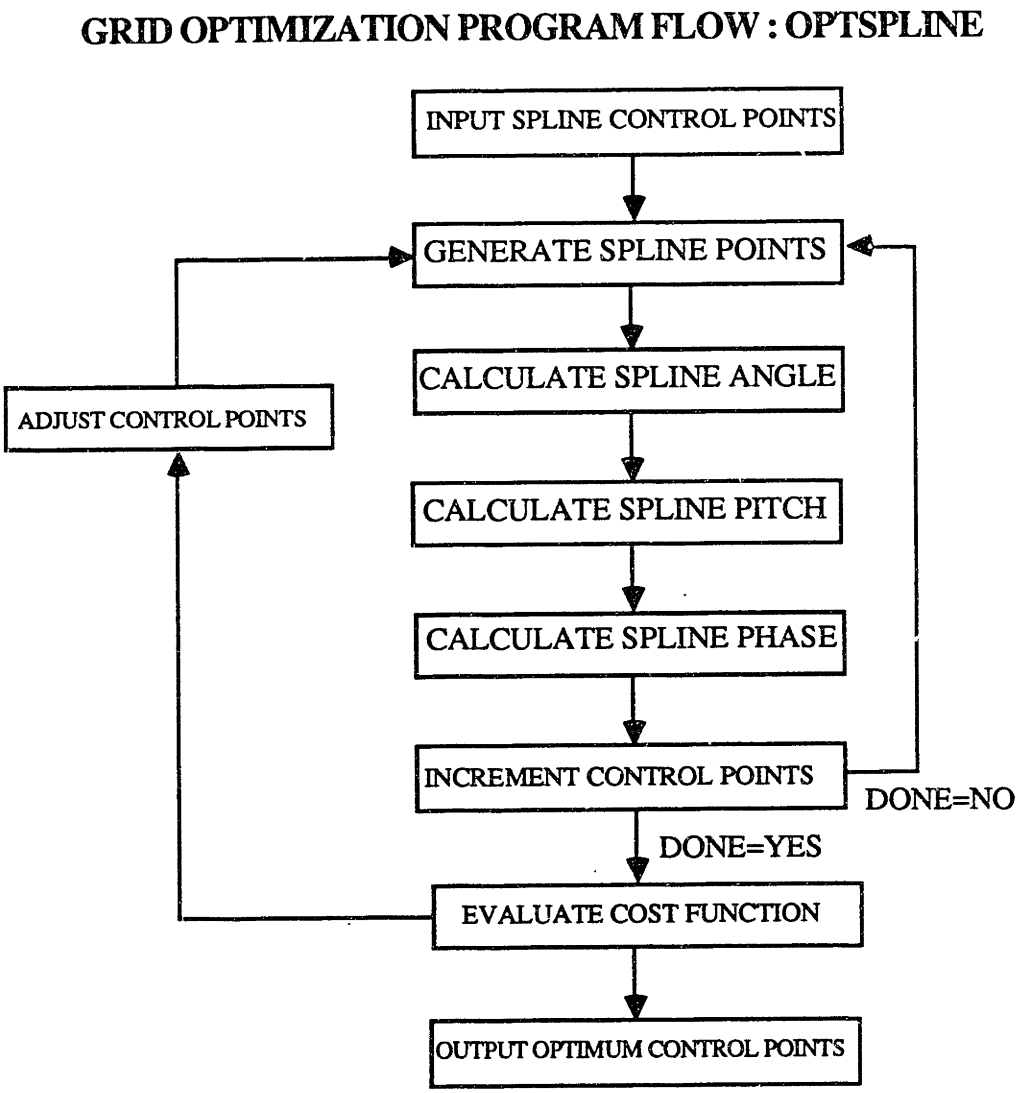

Figure 4.3: Method of Splines - Program Flow Chart

4.2 Bézier Splines

Bézier splines are a commonly used cubic spline that are of the form

$$RX(u) = (1-u)^3X_1 + 3u(1-u)^2X_2 + 3u^2(1-u)X_3 + u^3X_4 \qquad (4.1)$$

$$RY(u) = (1-u)^3Y_1 + 3u(1-u)^2Y_2 + 3u^2(1-u)Y_3 + u^3Y_4. \qquad (4.2)$$

They are defined by the four control points (**X**,**Y**) and are generated by incrementing a path parameter, u, from zero to one [28]. A general Bézier spline is shown in Figure 4.4. The flexibility of spline functions is discussed in a number of texts [1,3,7,26,30,36,39].

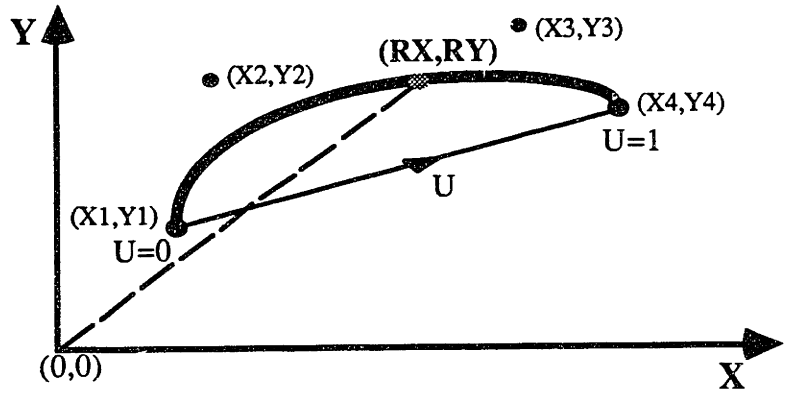

Figure 4.4: Bézier Spline

The curve of the Bézier spline passes through the first and last control points. The curve is tangent to the lines that connect both the first and second and the third and fourth control points. The curve lies inside its control polygon (the polygon defined by the four control points). Bézier splines were chosen because of their flexibility and ease of manipulation. Spline curves are piecewise smooth and continuous. The two center control points are repositioned and the curve adjusts to produce any contour. This method provides a way to change the spline angles, pitches, and phases in order to tailor the equiorder surfaces in a flexible manner.

4.3 Obtaining Standard Moiré Parameters

The standard Moiré parameters are the grid angle, pitch, and phase (first described in Wander) [42]. These parameters are used in the equiorder surface equation (2.8) that was derived for straight line grids. The spline parameters must be delineated into corresponding standard parameters at each of the sixteen locations of evaluation in order to utilize the equiorder surface equation. The next few sections address this problem.

4.3.1 Correspondence: Object to Grid Points

After generating grids that are composed of splines, the equiorder surfaces have to be computed at distinct points on the grids. The correspondence between projecting and viewing grids and the object was examined.

The correspondence was found by scrutinizing the equations describing the object points, the grid points, and the transformation between viewing and projecting systems. Object to grid correspondences are derived from equations (2.4) to (2.7). The grid positions are a function of the object positions.

The object to grid correspondence points were plotted (Figure 4.5). The corresponding object is shown in Figure 4.1. For the case shown, a flat plate was used. In general, the correspondence depends on the object under inspection. The sixteen grid points were used for evaluation purposes when computing grid angles,pitches, and phases.

4.3.2 Angle Formulation

The grid line angles are not calculated at each point along the splines to avoid unnecessary computation time. Instead, the angles as well as the other Moiré parameters are computed at the sixteen evaluation points in the grid.

The angle of a spline can be found using the equation:

$$\text{Slope} = \frac{\partial RY}{\partial u} * \frac{\partial u}{\partial RX} = \frac{\partial RY}{\partial RX} =$$

$$= \frac{-\mathbf{Y_1}(1-u)^2 + \mathbf{Y_2}(3u-1)(u-1) + \mathbf{Y_3}u(-3u+2) + \mathbf{Y_4}(u^2)}{-\mathbf{X_1}(1-u)^2 + \mathbf{X_2}(3u-1)(u-1) + \mathbf{X_3}u(-3u+2) + \mathbf{X_4}}. \qquad (4.3)$$

The (X,Y) values represent the x and y values of four spline control points. The angle formulation is shown in Figure 4.6.

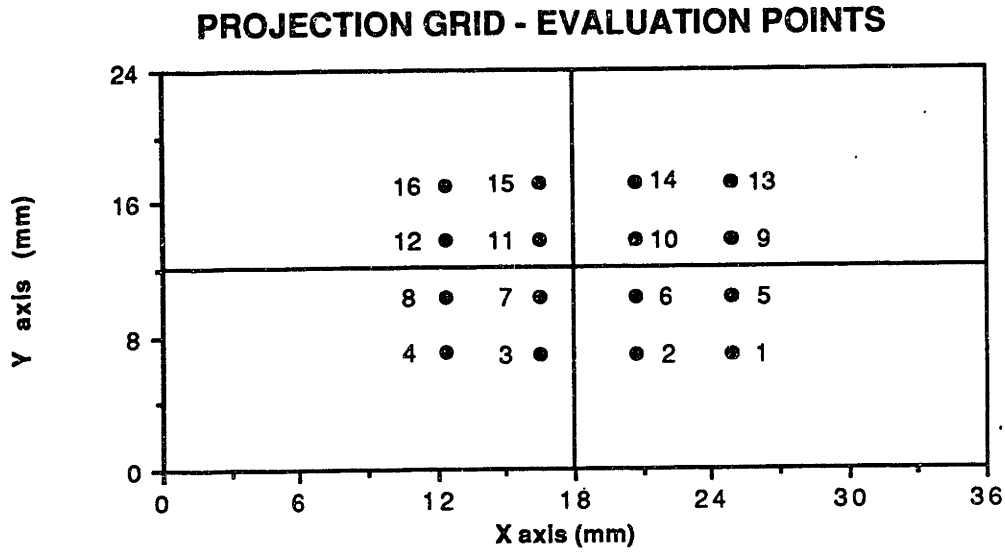

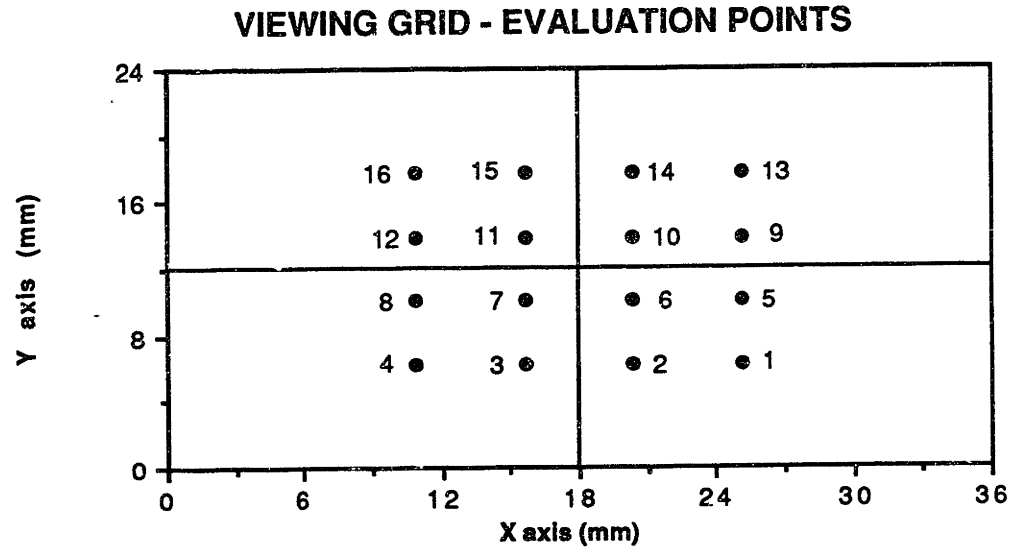

Figure 4.5: Object to Grid Correspondence

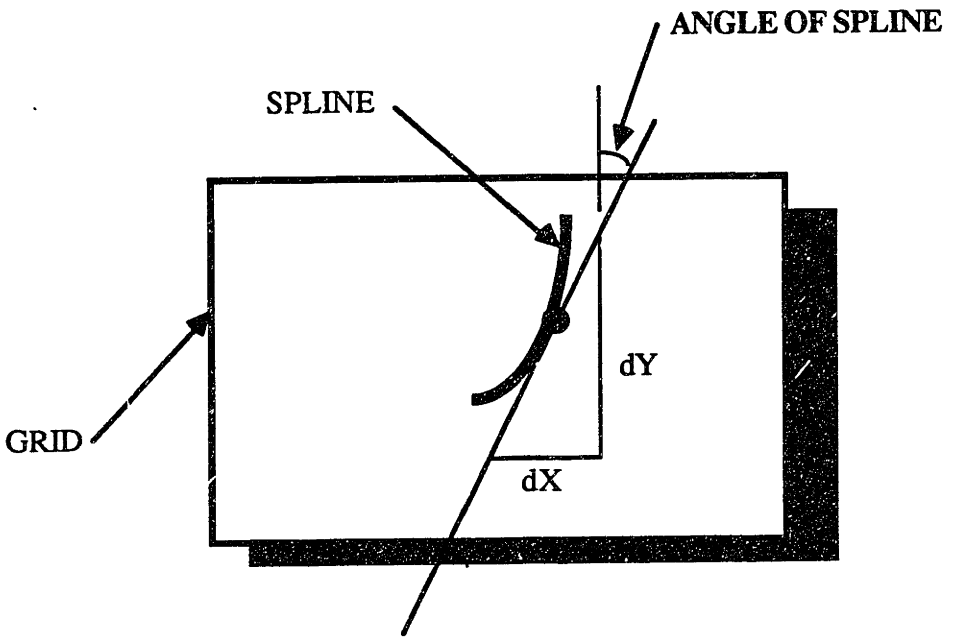

Figure 4.6: Spline Grid Angle Formulation

When a spline point is computed and it falls within one of the sixteen grid evaluation regions, the angle is computed. The x and y values of the point of this evaluation, along with the corresponding path parameter, u, are stored for use in the pitch and phase calculations.

4.3.3 Pitch Formulation

The pitch of the splines is determined by computing the spacing between adjacent splines at the point, u, stored in the previous angle calculation. The spacing and accompanying pitch are shown in Figure 4.7. The pitch can be found using the equation:

$$\text{Pitch} = P = \cos\alpha * \text{spacing} \tag{4.4}$$

where α is the grid line angle, and the *spacing* comes from equation 4.5:

$$\text{spacing} = \sqrt{(RX-x)^2+(RY-y)^2}. \tag{4.5}$$

This is the equation for the distance between two points, derived from the Pythagorean Theorem. Again, sixteen pitches are computed. The pitch is allowed to vary freely as the spline control points migrate in this procedure.

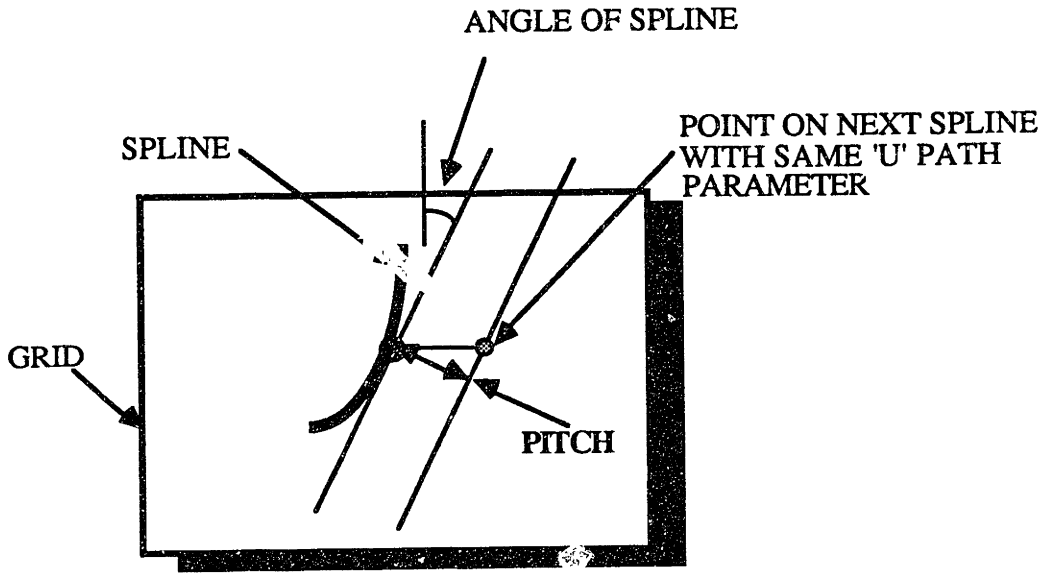

Figure 4.7: Spline Grid Pitch Formulation

4.3.4 Phase Formulation

The phase at the grid evaluation regions is determined by referencing a local point on the spline to the center of the grid in all cases. This follows the definitions set by Wander and Leonard for straight line grids [20,42]. The phase is a local one referenced to a common center point. The calculation utilizes the spacing and angle formulations described in Sections 4.3.2 and 4.3.3. The phase is found using the equation:

$$\text{Phase} = \phi = \frac{\text{factor} * \cos\alpha}{P}. \qquad (4.6)$$

The *factor* is the distance from the closest dark grid line to the grid center. The phase can be positive or negative, if the distance *factor* falls to the left side of the grid center. The details of the method of phase formulation appear in Figure 4.8.

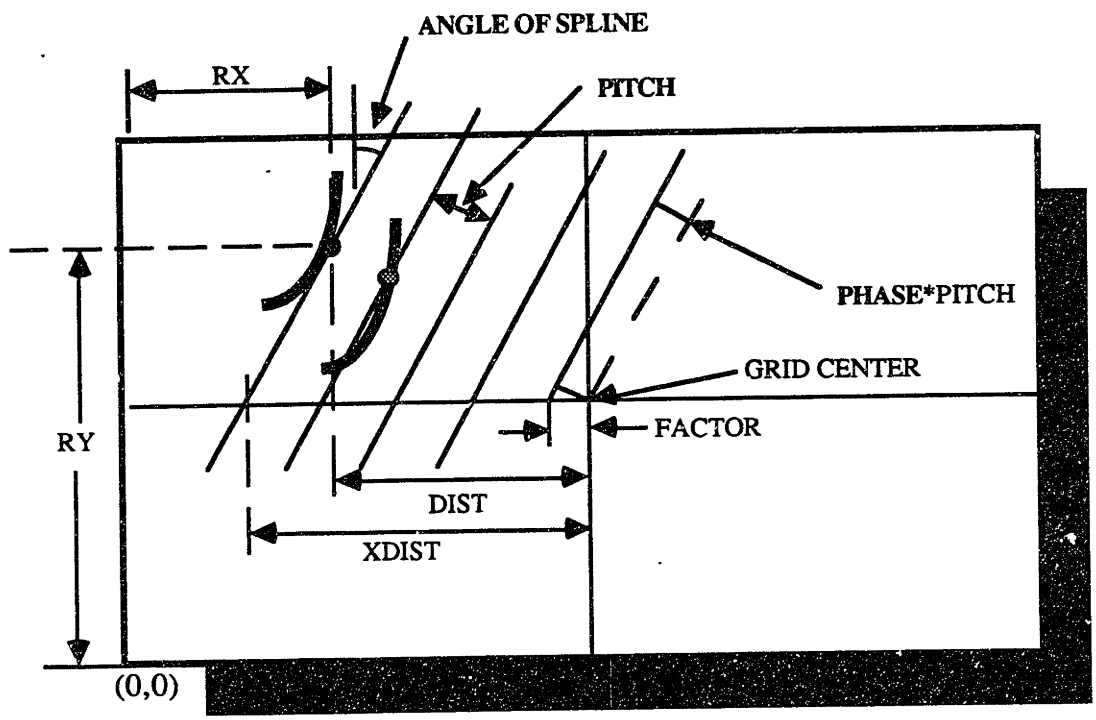

Figure 4.8: Spline Grid Phase Formulation

4.4 Grid Optimization

Once the standard Moiré parameters are obtained at the sixteen evaluation points, the grid optimization can be performed. Limits are placed on the spline control points. These limits define the upper and lower bounds within which the points can wander while searching for the optimum tailored equiorder surface solution. The optimization routine finds a global minimum, within specified limits, of a function of N variables. The subroutine ZXMWD, obtained from IMSL, was used to perform the optimization. This subroutine identifies a number of starting points within the specified limits of the variables then optimizes the cost function using a quasi-Newton method [17]. Several articles were examined which describe this optimization procedure in detail [4,10,34]. The number of starting points and significant digits of accuracy can be varied as required to reach an

acceptable solution. The multi-variable optimization can begin when the object's tolerance and it's characteristics (location, points, and normals), derived from an equation representing the object, are obtained.

First, by using the tolerance of the inspection and normals to the object, points at a half tolerance width from the sixteen object evaluation points can be obtained from:

$$x_5 = x_c + x_n \frac{TOL}{2} \tag{4.8}$$

$$y_5 = y_c + y_n \frac{TOL}{2} \tag{4.9}$$

$$z_5 = z_c + z_n \frac{TOL}{2} \tag{4.10}$$

where (x_n,y_n,z_n) and (x_c,y_c,z_c) are the object normals and points shown in Figure 4.9. Before the optimization can proceed further, an angle criterion is checked. This criterion states that the difference in the grid line angles $(\alpha_p-\alpha_v)$ must be less than 45 degrees. If this angle becomes too large, obtaining a fringe image becomes difficult.

At the sixteen calculated points, (x_5,y_5,z_5), the fringe orders corresponding to the nearest equiorder surfaces associated with dark fringes are calculated. The fringe orders at these points constitute the first part of the cost function that defines the optimization. Part 1 of the cost function is defined by the equation:

$$\text{Part 1} = \sum_{i=1}^{16} \left(FO(i) - FO_{desired}(i) \right)^2 \tag{4.11}$$

where $FO_{desired}(i) = integer \pm 0.5$ and the FO(i) are the sixteen fringe orders corresponding to the sixteen evaluation points. This part of the cost function ensures that the equiorder surface calculated at the above point will produce a dark fringe if it intersects the object.

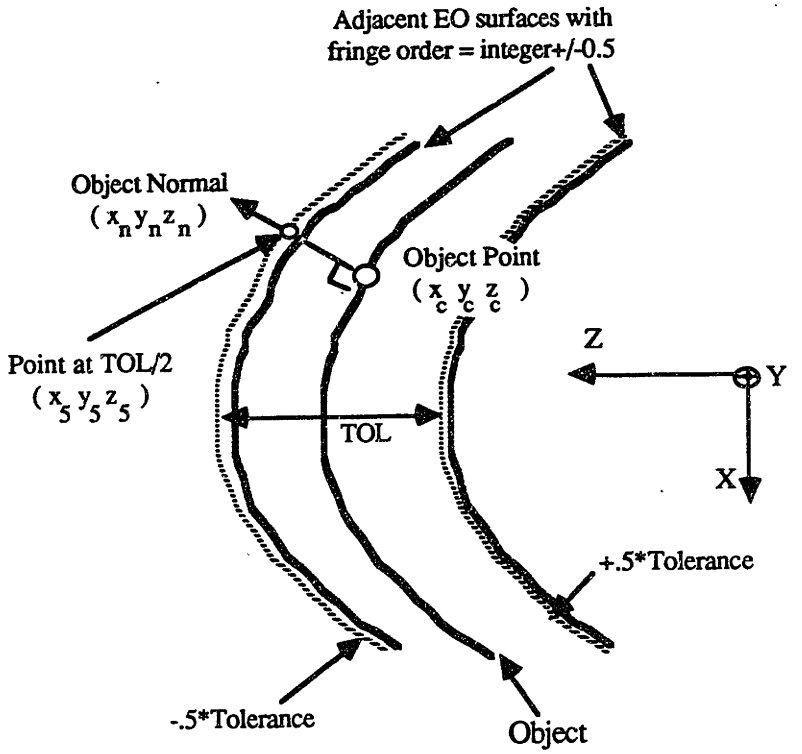

Figure 4.9: Object Definition

Part 2 of the cost function ensures that the spacing of adjacent equiorder surfaces (with a fringe order equal to an *integer ± 0.5*) equals twice the tolerance of the inspection. The difference between the distance from the above equiorder surface with a fringe order equal to an *integer ± 0.5* to the equiorder surface with a fringe order equal to an *integer ± 0.5 + 1* and twice the tolerance band of the inspection is squared. That is,

$$\text{Part 2} = \sum_{i=1}^{16} (\text{adjacent equiorder surfaces with FO}=\textit{integer}\pm 0.5(i) - 2*\text{Tolerance})^2 \qquad (4.12)$$

Finally, summing these two parts generates the total cost function over a sixteen point evaluation space:

$$\text{Cost Function} = J = \text{Part 1} + \text{Part 2} \tag{4.13}$$

The cost function is minimized over the space that is defined by the control point limits described earlier. The control points defining the projection and viewing grids can be utilized to plot the grids when the minimum is obtained and the physical inspection process can now begin.

5 ANALYTICAL RESULTS

5.1 General

This chapter describes the grid optimization program and typical analytical results obtained using the Method of Splines. The program output consists of (1) the cost function summed over the sixteen evaluation regions (Equation 4.13), (2) the plots of object, tolerance surfaces, and equiorder surfaces at four cross sections of the object (before and after optimization), and (3) projecting and viewing grids. Five objects will be presented to demonstrate the technique: an object similar to the equiorder surface shape obtained with straight line grids, a flat object, a cylindrical object, an object representing a turbine blade, and a turbine blade with some twist. Sixteen object points (x_c,y_c,z_c) as well as sixteen object normals (x_n,y_n,z_n) at these points are needed for the grid optimization and equiorder surface plot programs.

5.2 Case 1: Object Similar to Equiorder Surface Shape Obtained with Straight Line Grids

5.2.1 Object Definition

This object matches the shape of the equiorder surfaces obtained when projecting and viewing grids are made up of straight grid lines. This object was inspected first to give confidence in the method. Note that each of the cases presented began with grids made up of straight lines. Because this object is so similar to the equiorder surfaces surrounding it, the optimal cost is expected to be low and the optimization should be successful. This object serves as a starting point for all other optimizations. The object is pictured in Figure 5.1. This picture represents only one cross-section. The object is the same at all other cross-sections.

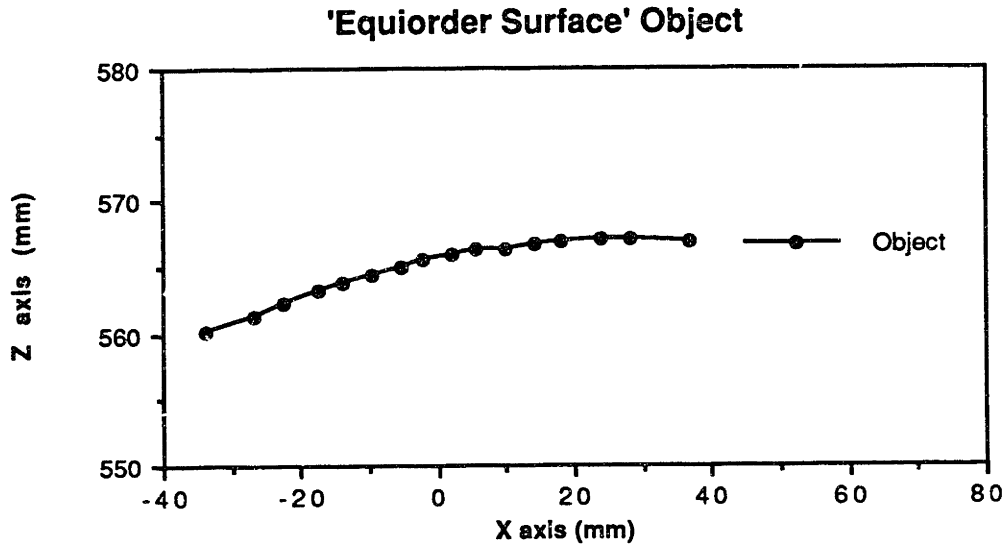

Figure 5.1: Object Similar to Equiorder Surfaces Obtained with Straight Lined Grids

5.2.2 Cost Function

The cost function defined in equation 4.13 and output from the grid optimization program for this object are shown in Figure 5.2. The distance errors are in millimeters. Note that the interferometer parameters for all optimizations are the same and are shown in Figure 3.1.

5.2.3 Projecting and Viewing Grids

The optimized projecting and viewing grids are shown in Figures 5.3 and 5.4 respectively. The grids in this chapter contain lines used to align the interferometer. Also, the grid coordinates are standard Cartesian coordinates (x $\rightarrow$, y $\uparrow$).

****
GRID OPTIMIZATION RESULTS
****

COST= 1.1591694E-02 # ITER= 20700.00

PROJECTING GRID CONTROL POINTS

1	2	3
8.000001	18.00000	28.00000
8.000001	18.00000	28.00000
8.000001	18.00000	28.00000
8.000001	18.00000	28.00000

VIEWING GRID CONTROL POINTS

1	2	3
8.000001	18.00000	28.00000
8.000001	18.00000	28.00000
8.000001	18.00000	28.00000
8.000001	18.00000	28.00000

EVAL #	F0	DISTANCE ERROR
1	-4.536616	0.2560348
2	-4.518379	8.4051780E-02
3	-4.500882	0.0000000E+00
4	-4.465094	0.2669685
5	-4.536612	0.2560348
6	-4.518373	8.4051780E-02
7	-4.500875	0.0000000E+00
8	-4.465091	0.2669685
9	-4.536622	0.2560348
10	-4.518375	8.4051780E-02
11	-4.500883	0.0000000E+00
12	-4.465084	0.2669685
13	-4.536616	0.2560348
14	-4.518374	8.4051780E-02
15	-4.500878	0.0000000E+00
16	-4.465091	0.2669685

Figure 5.2: Cost Function and Grid Optimization Results - Object Similar to Equiorder Surfaces Obtained with Straight Lined Grids

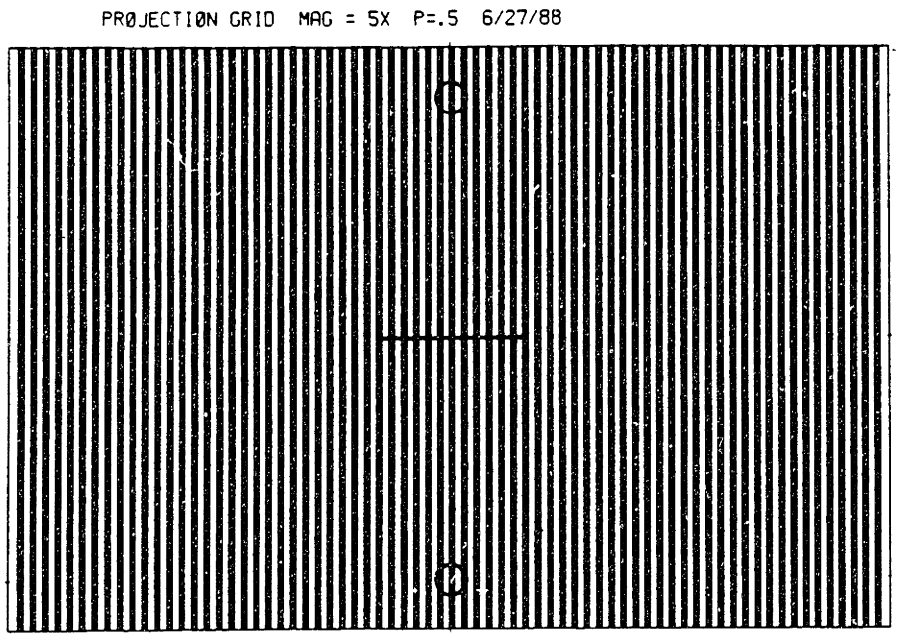

Figure 5.3: Projection Grid - Object Similar to Equiorder Surfaces Obtained with Straight Lined Grids

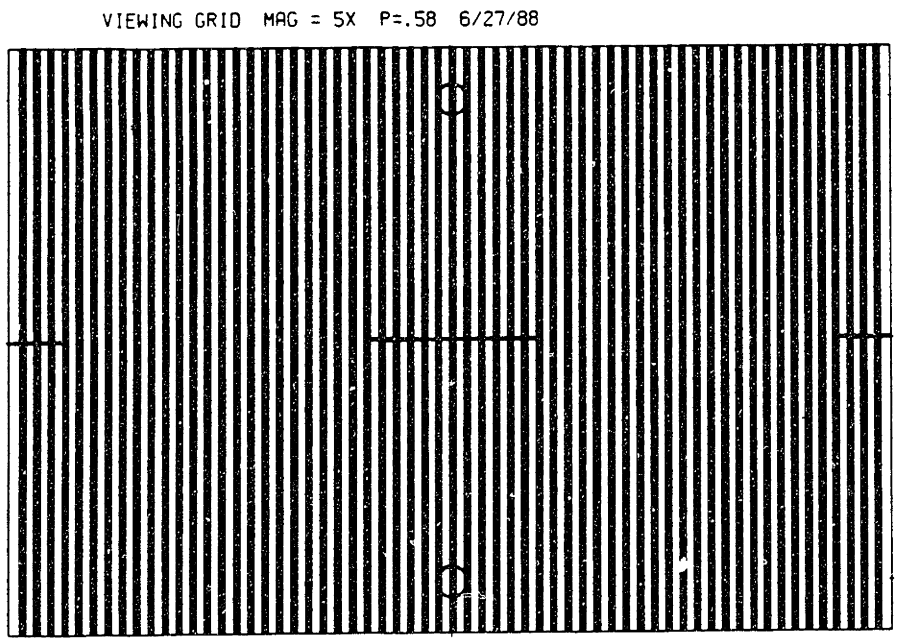

Figure 5.4: Viewing Grid - Object Similar to Equiorder Surfaces Obtained with Straight Lined Grids

5.3 Case 2: Flat Object

5.3.1 Object Definition

The flat object points are defined as (refer to Figure 4.9)

$$x_c, y_c = \text{equally spaced object points of Figure 4.1,} \quad (5.1)$$

$$z_c = \text{constant} = 567.5 \text{ mm} = z_{ref}, \quad (5.2)$$

with object normals at those points

$$x_n = 0.0, \quad (5.3)$$

$$y_n = 0.0, \quad (5.4)$$

and

$$z_n = 1.0. \quad (5.5)$$

5.3.2 Cost Function

The cost function defined in equation 4.13 and the output from the grid optimization program for this object are shown in Figure 5.5.

5.3.3 Equiorder Surface Plots

The equiorder surface plots for this object before and after optimization are shown in Figures 5.6 and 5.7 respectively. Note that the surrounding equiorder surfaces associated with dark fringes were found to be -4.5 and -3.5 based on the interferometer setup. Also, all cross-sections shown are top views looking into the negative y-axis. The four cross-sections are made at equally spaced heights along the object. Refer to Figure 4.1.

5.3.4 Projecting and Viewing Grids

The optimized projecting and viewing grids are shown in Figures 5.8 and 5.9 respectively.

****
GRID OPTIMIZATION RESULTS - FLAT OBJECT
****

COST= 0.3171028 # ITER= 15181.00

PROJECTING GRID CONTROL POINTS

1	2	3
9.091278	18.58176	28.69157
9.052814	18.71411	28.86842
9.190651	18.72667	28.84046
8.858123	18.58706	28.75296

VIEWING GRID CONTROL POINTS

1	2	3
7.544037	17.23527	26.10326
7.432324	16.30068	27.54992
7.383679	17.83882	26.21345
7.225279	16.19466	27.04792

EVAL #	FO	DISTANCE ERROR
1	-4.494431	0.0000000E+00
2	-4.448259	0.4299927
3	-4.532153	0.2219849
4	-4.464925	0.2589722
5	-4.540205	0.3029785
6	-4.499671	0.0000000E+00
7	-4.585787	0.7569580
8	-4.505454	0.0000000E+00
9	-4.580655	0.7089233
10	-4.461293	0.2959595
11	-4.512534	2.6000977E-02
12	-4.510036	9.7656250E-04
13	-4.527174	0.1729736
14	-4.426691	0.6509399
15	-4.507802	0.0000000E+00
16	-4.553776	0.4499512

Figure 5.5: Cost Function and Grid Optimization Results - Flat Object

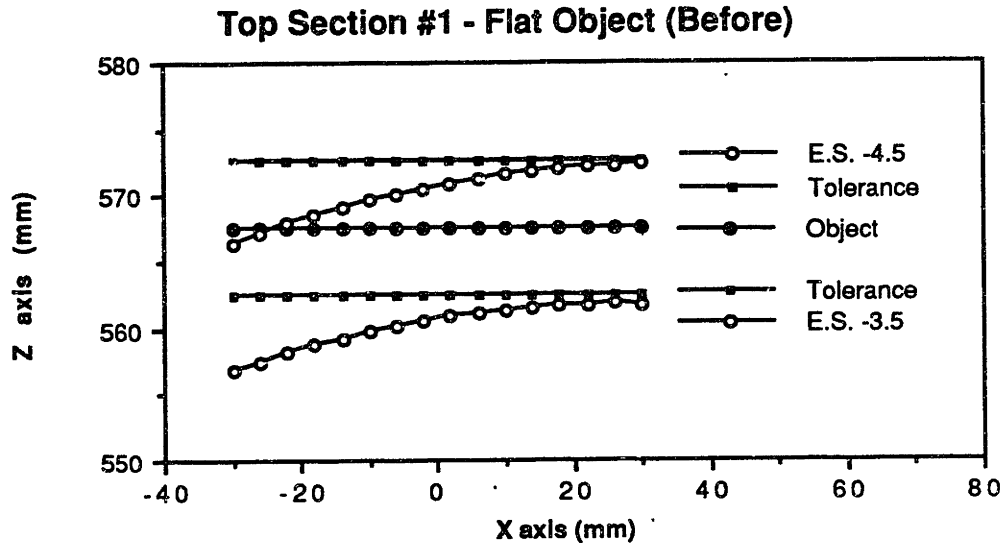

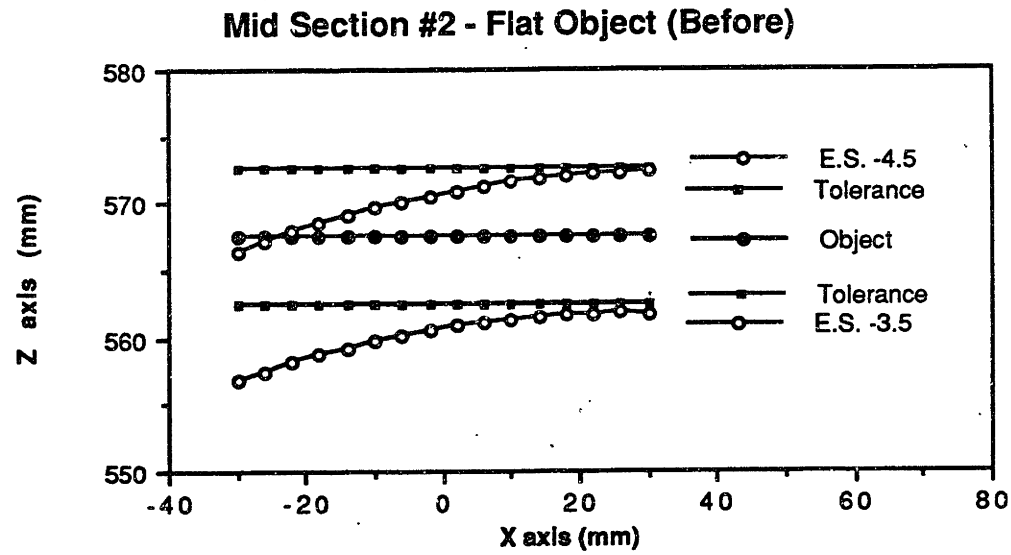

Figure 5.6: Equiorder Surface Plots - Before Optimization
Flat Object

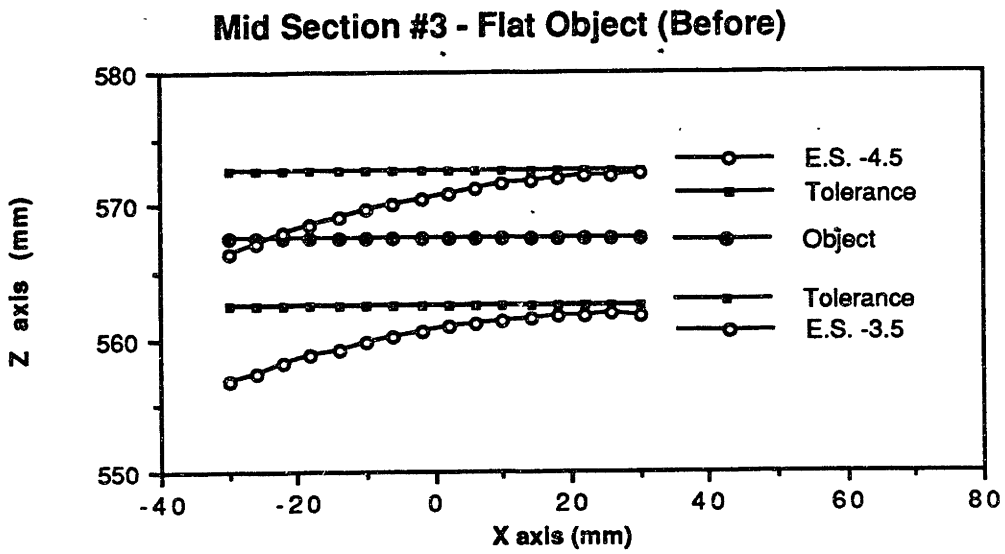

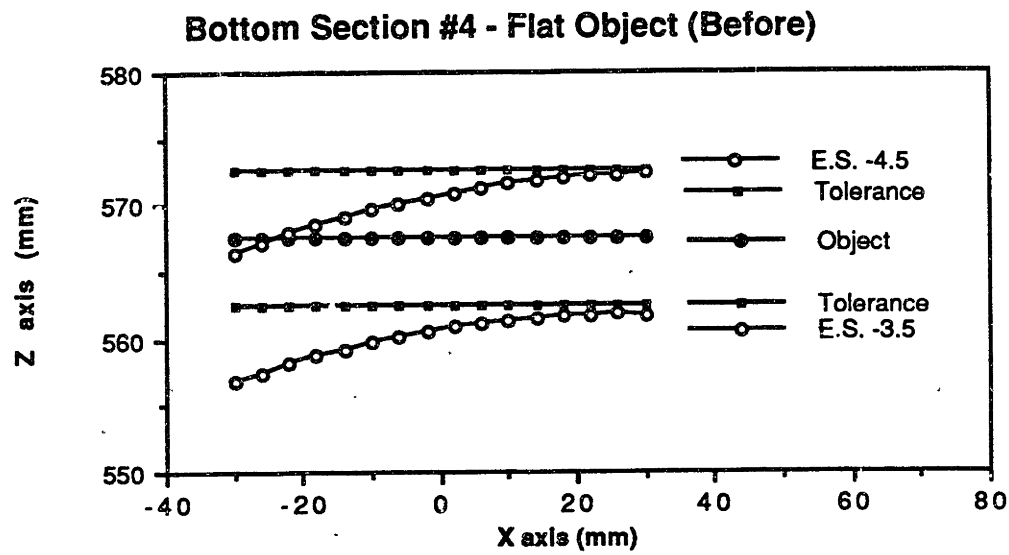

Figure 5.6 cont.: Equiorder Surface Plots - Before Optimization
Flat Object

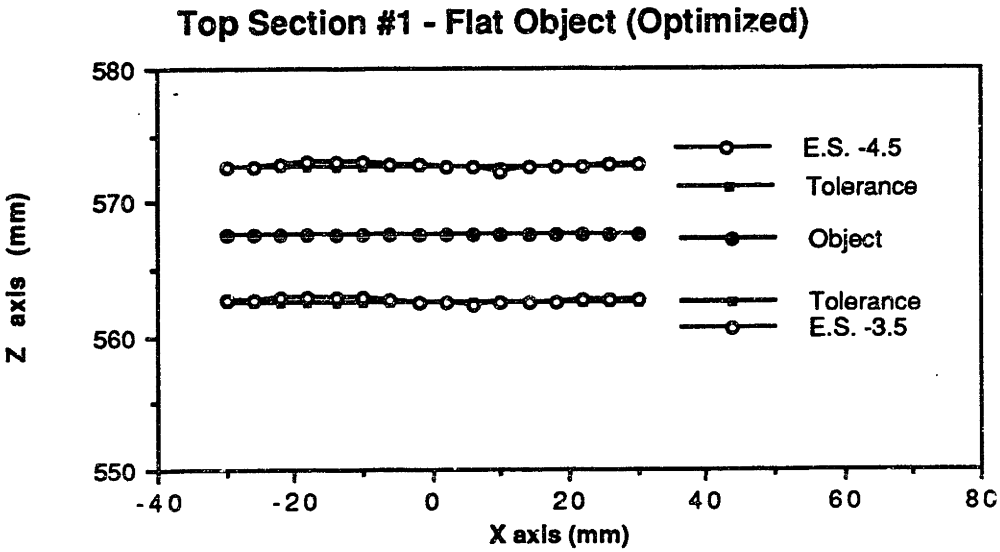

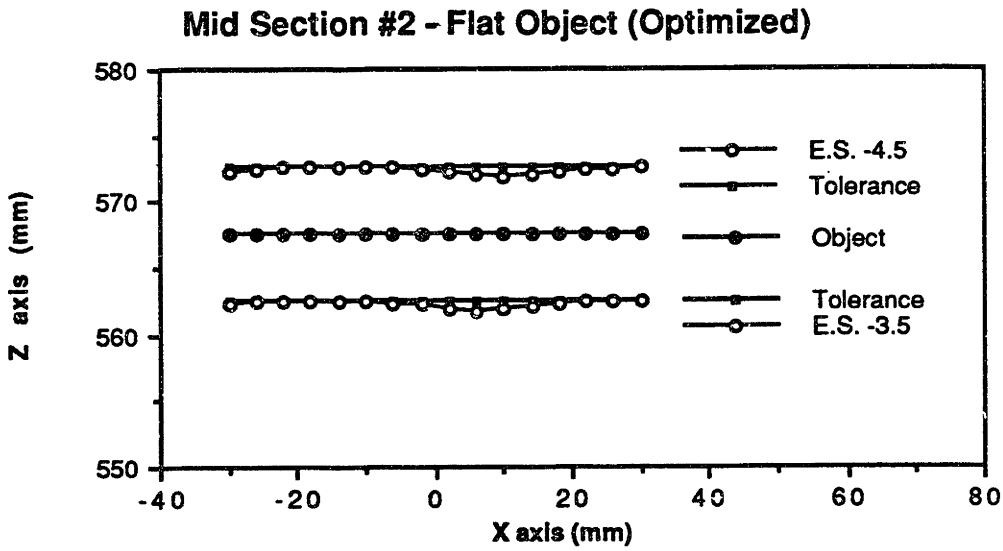

Figure 5.7: Equiorder Surface Plots - After Optimization
Flat Object

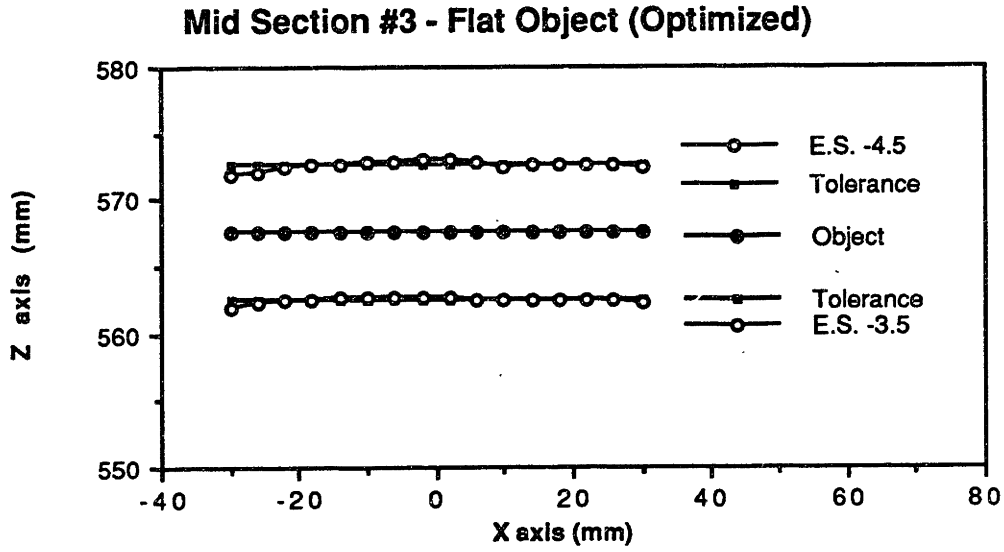

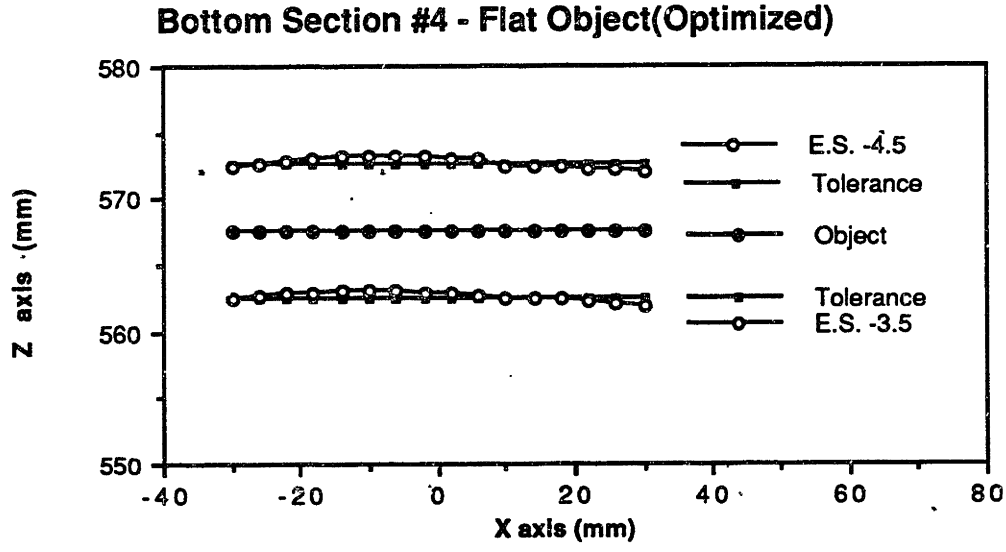

Figure 5.7 cont.: Equiorder Surface Plots - After Optimization
Flat Object

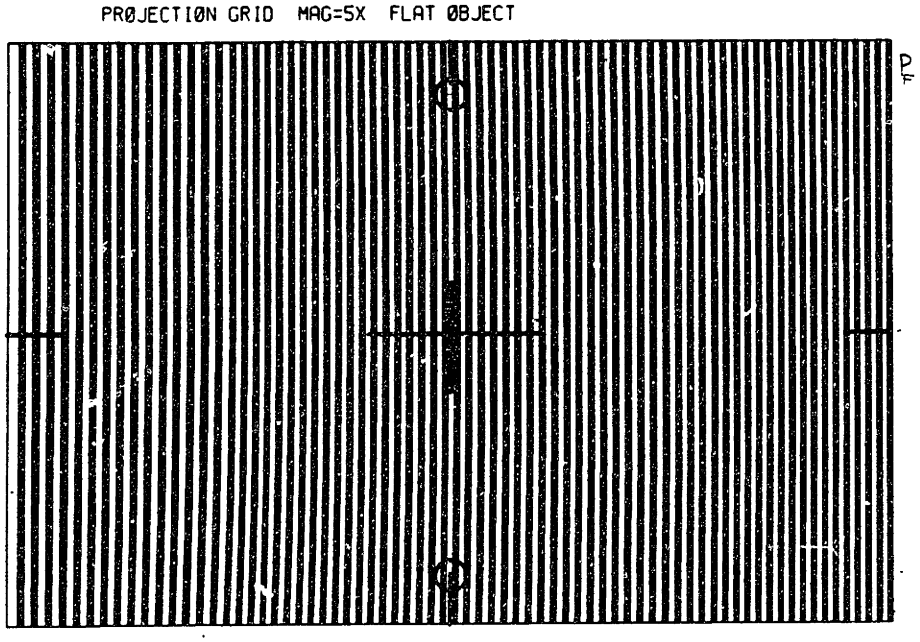

Figure 5.8: Projection Grid - Flat Object

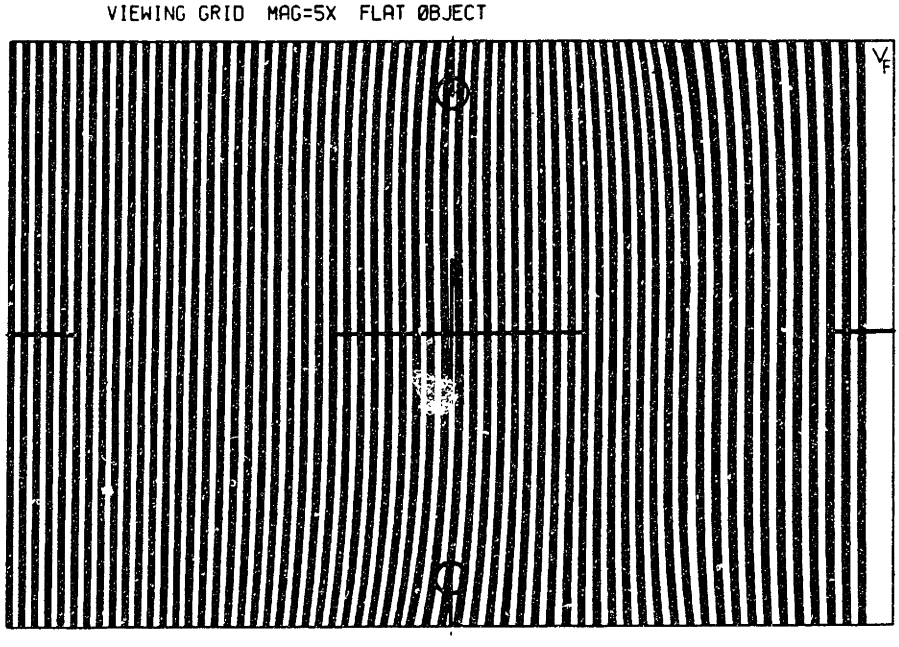

Figure 5.9: Viewing Grid - Flat Object

5.4 Case 3: Cylindrical Object

5.4.1 Object Definition

Figure 5.10 shows the object configuration for theoretical inspection of the cylinder. The chord length, CL, is the object width and is equal to 76.2 mm. The chord height, CH, is constant for this case. The radius (RADIUS) of the object is 50 mm. The x and y object points, x_c and y_c, are predetermined, equally spaced points on the object surface (Figure 4.1). The z object point, z_c, is found using

$$z_c = z_{ref} + \sqrt{RADIUS^2 - x_c^2} - RADIUS \tag{5.6}$$

The three object normals (x_n, y_n, z_n) are defined as

$$x_n = 1 \sin\beta \cos\alpha, \tag{5.7}$$

$$y_n = 0.0, \tag{5.8}$$

and

$$z_n = 1 \cos\beta \cos\alpha. \tag{5.9}$$

With the object defined, the grid optimization for a cylinder can take place.

5.4.2 Cost Function

The cost function defined in equation 4.13 and the output from the grid optimization program for this object are shown in Figure 5.11.

5.4.3 Equiorder Surface Plots

The equiorder surface plots for this object before and after optimization are shown in Figures 5.12 and 5.13 respectively.

5.4.4 Projecting and Viewing Grids

The optimized projecting and viewing grids are shown in Figures 5.14 and 5.15 respectively.

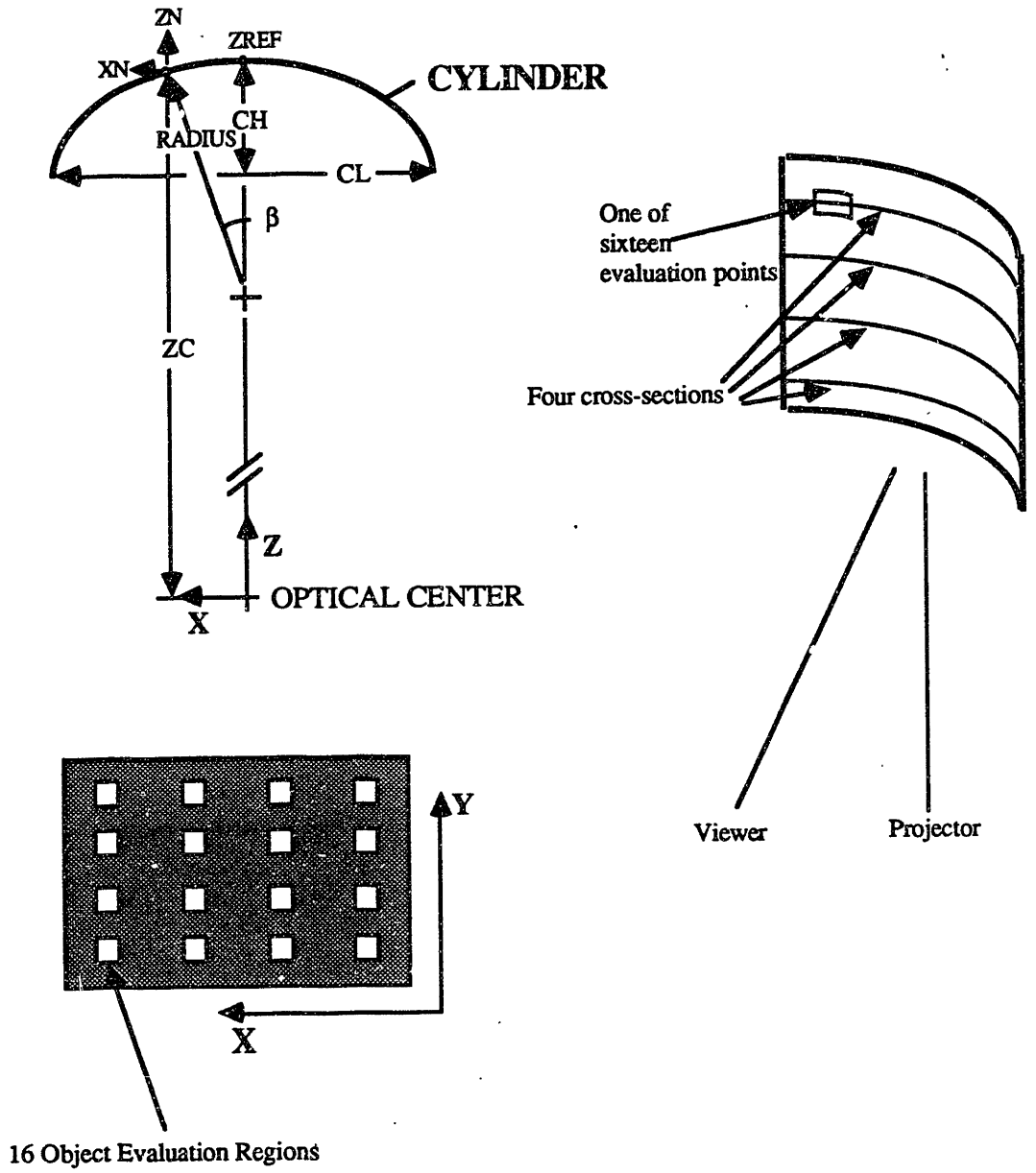

Figure 5.10: Cylindrical Object

****
GRID OPTIMIZATION RESULTS - CYLINDER
****

COST= 0.1600991 # ITER= 16205.00

PROJECTING GRID CONTROL POINTS

1	2	3
7.867037	18.04398	28.69347
7.520161	17.83287	28.14184
7.672017	17.81244	28.28487
8.112299	18.19753	28.82935

VIEWING GRID CONTROL POINTS

1	2	3
7.983391	17.31903	28.77431
7.873570	17.08838	27.34466
7.880857	17.20838	28.72961
8.193884	17.34223	28.05313

EVAL #	FO	DISTANCE ERROR	SPACING
1	-4.378957	1.106937	9.943771
2	-4.595564	0.8729228	10.08442
3	-4.548594	0.3929498	10.01696
4	-4.456887	0.3349953	9.967194
5	-4.408009	0.8139175	9.905930
6	-4.627988	1.198906	10.04717
7	-4.550771	0.4159367	10.02848
8	-4.470992	0.1930099	9.975204
9	-4.364922	1.248925	9.968948
10	-4.614754	1.065909	10.05957
11	-4.545635	0.3639821	10.03384
12	-4.481392	8.6981967E-02	9.961243
13	-4.377948	1.116934	9.943161
14	-4.609117	1.008910	10.06486
15	-4.528522	0.1899955	10.04667
16	-4.468875	0.2139976	9.978180

Figure 5.11: Cost Function and Grid Optimization Results - Cylinder

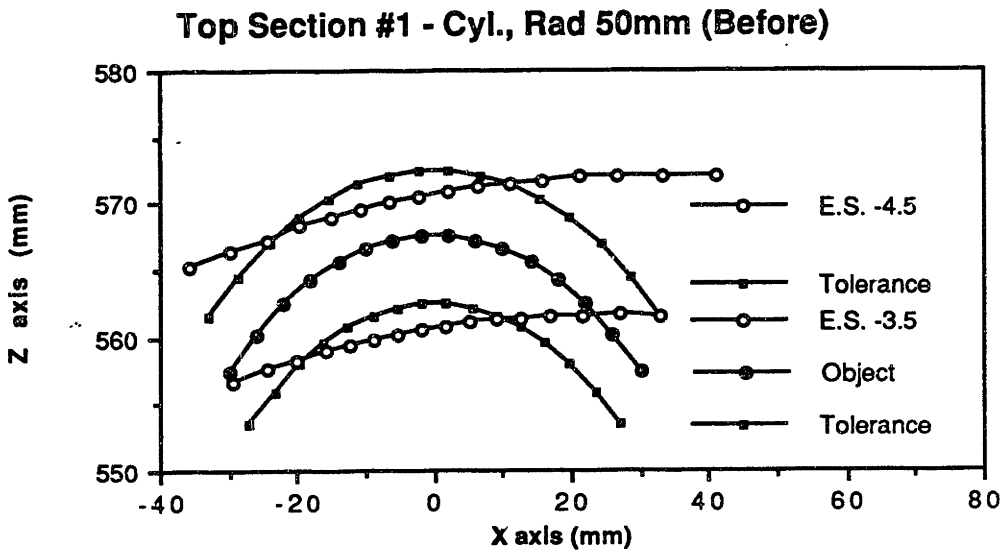

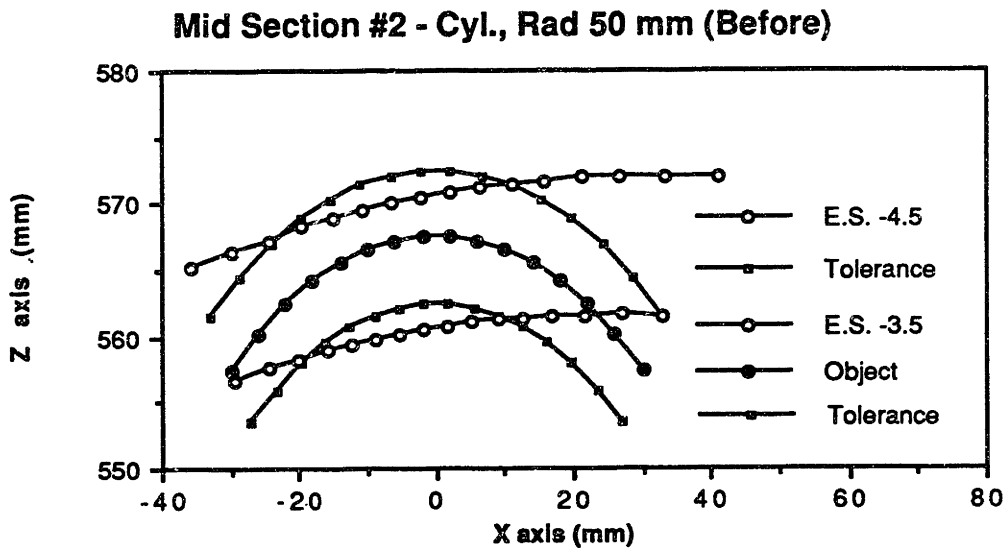

Figure 5.12: Equiorder Surface Plots - Before Optimization Cylinder

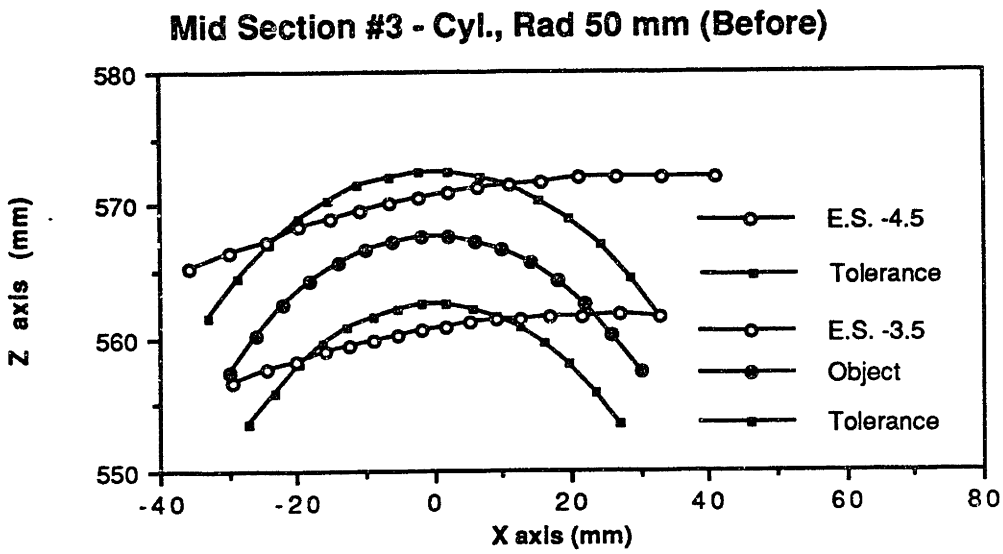

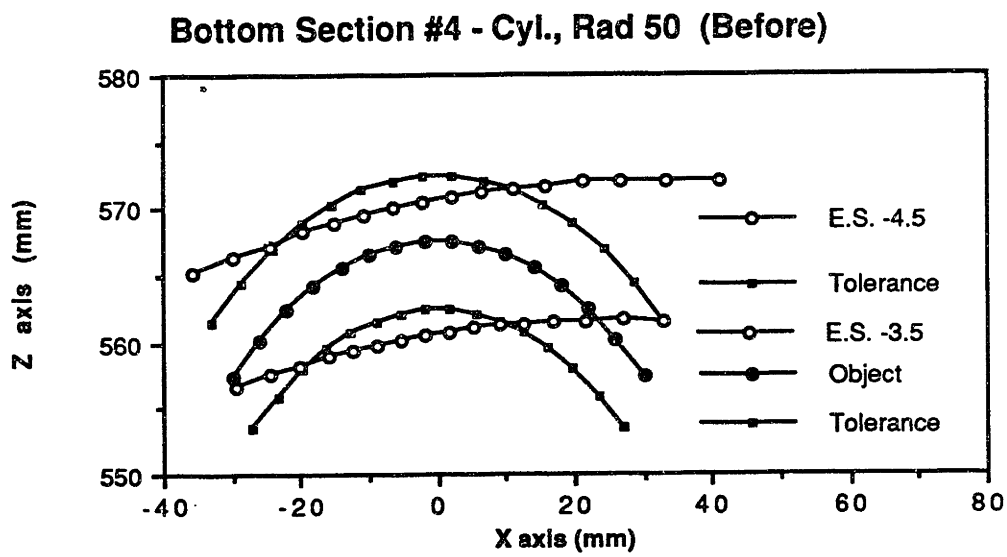

Figure 5.12 cont.: Equiorder Surface Plots - Before Optimization
Cylinder

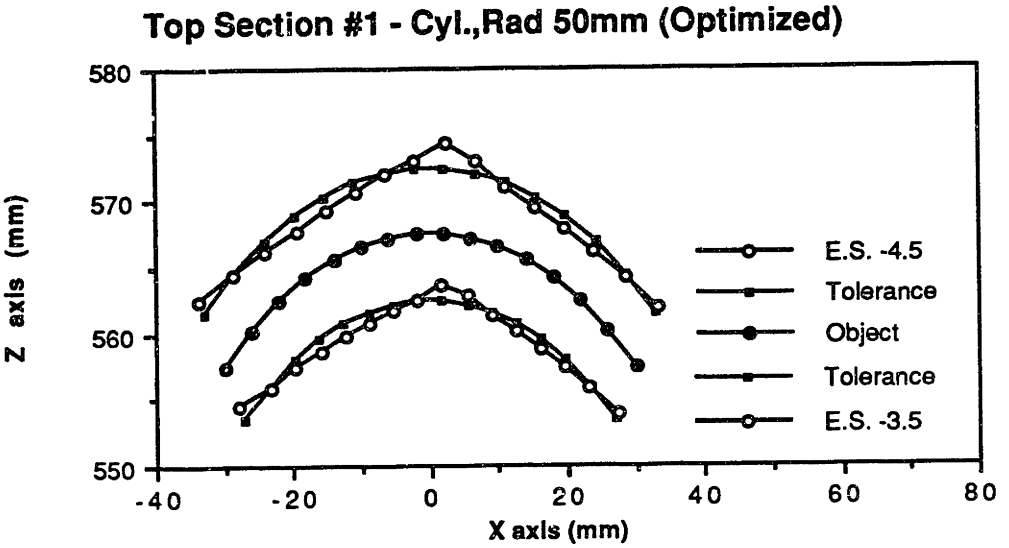

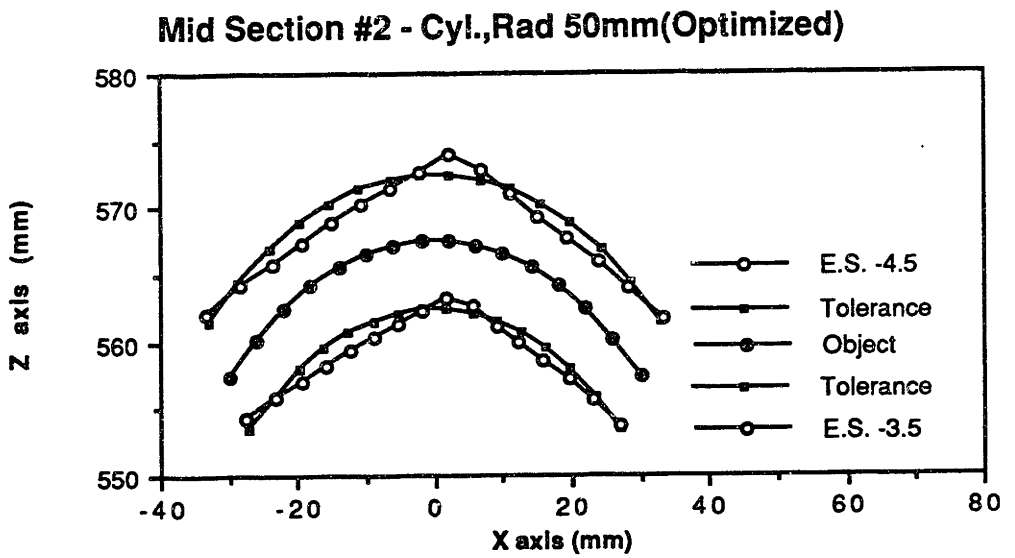

Figure 5.13: Equiorder Surface Plots - After Optimization - Cylinder

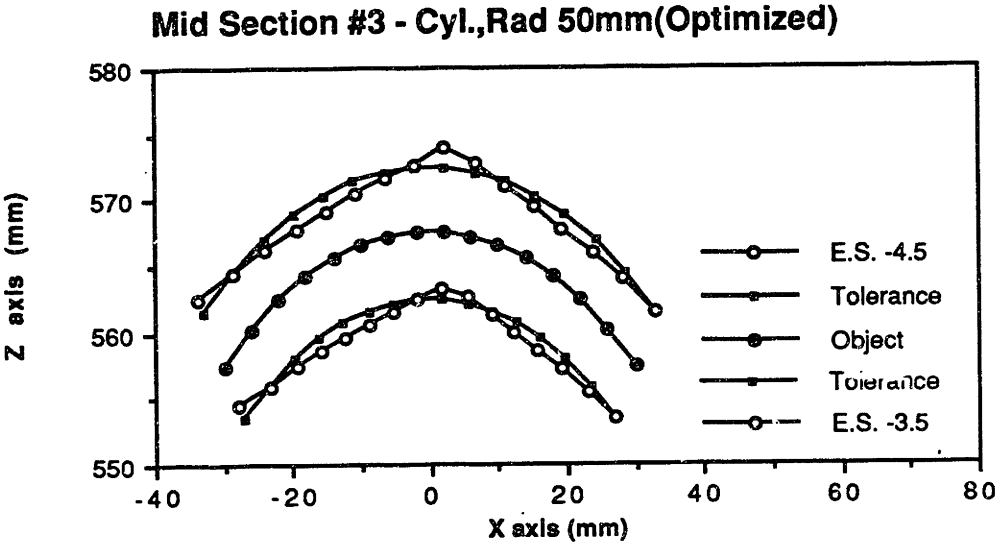

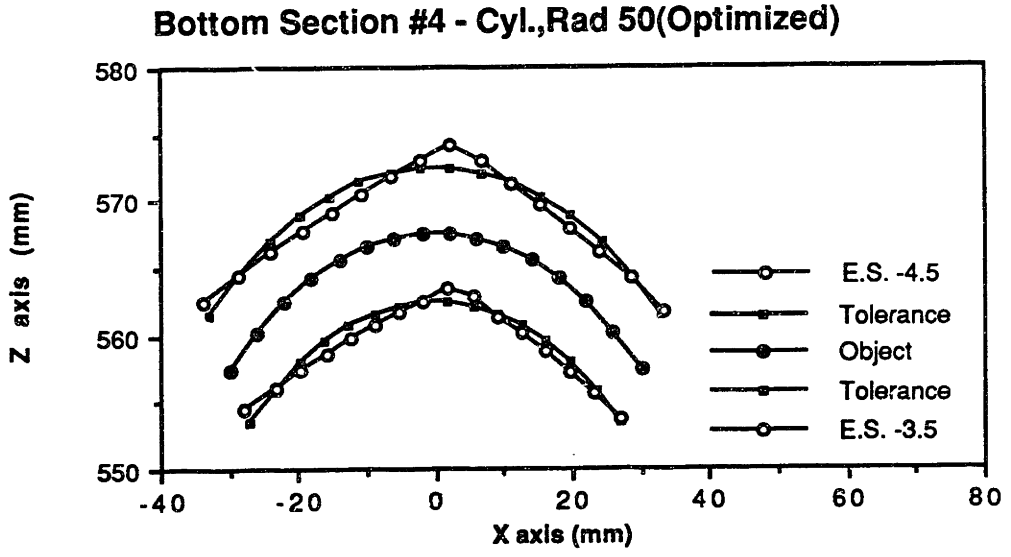

Figure 5.13 cont.: Equiorder Surface Plots - After Optimization - Cylinder

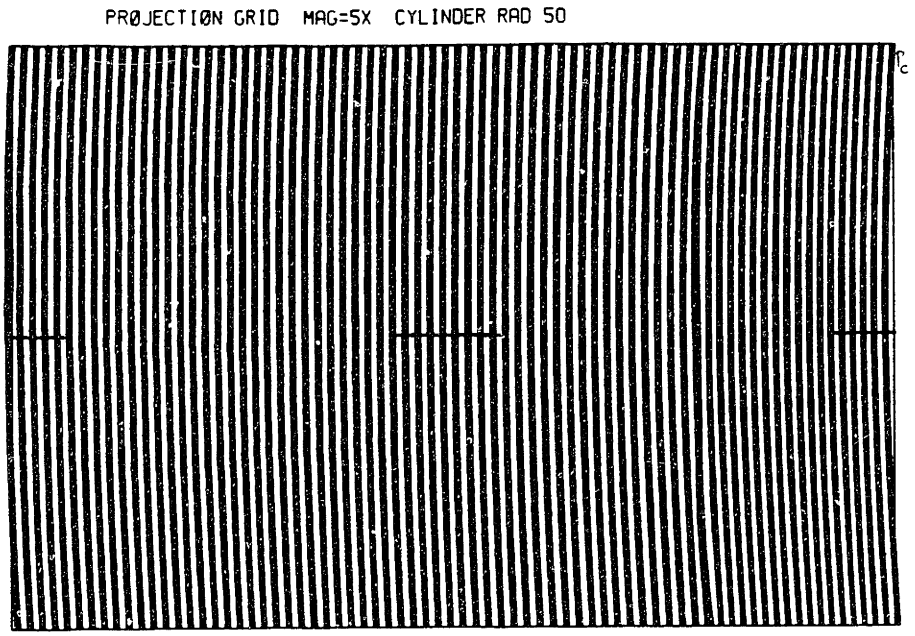

Figure 5.14: Projection Grid - Cylinder

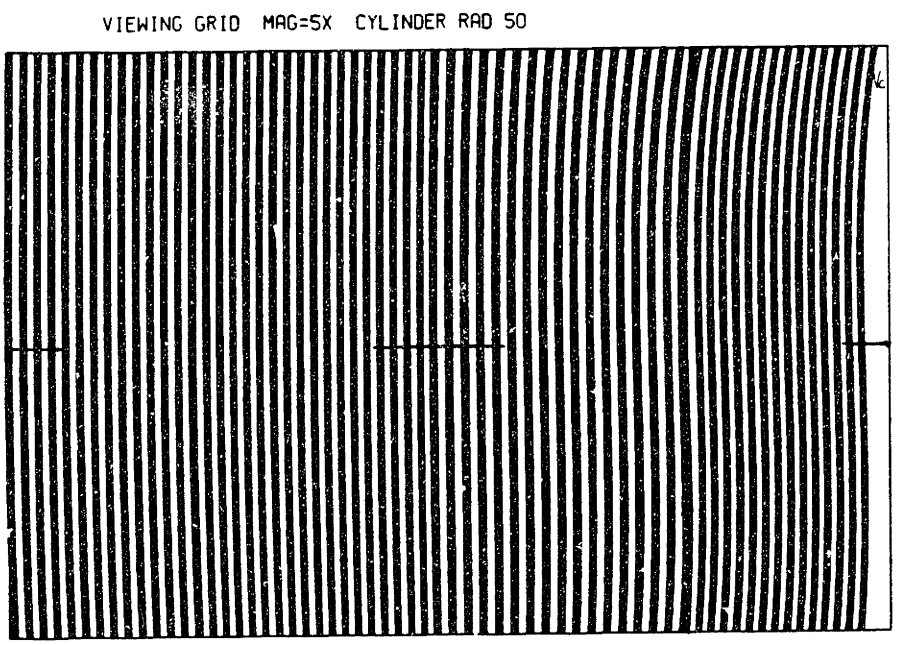

Figure 5.15: Viewing Grid - Cylinder

5.5 Case 4: Object Similar to a Turbine Blade

5.5.1 Object Definition

Figure 5.16 shows the object configuration for theoretical inspection of an object similar to a turbine blade. The chord length, CL, is the object width and is equal to 76.2 mm. The chord height, CH, is a function of the height along the object:

$$CH = -\frac{\text{Base Chord Length}}{\text{Total Object Height}} * \text{Height Along Object} + \text{Base Chord Length} \qquad (5.10)$$

The radius of the object for this chord height is

$$RADIUS = \frac{CL^2}{8*CH} + \frac{CH}{2} \; . \qquad (5.11)$$

The x and y object points, x_c and y_c, are predetermined, equally spaced points on the object surface (Figure 4.1). The z object point, z_c, is found using the equation:

$$z_c = z_{ref} + \sqrt{RADIUS^2 - x_c^2} - RADIUS \qquad (5.12)$$

The object angles α and β are defined by:

$$\alpha = \tan^{-1}\left(\frac{RADIUS - \sqrt{RADIUS^2 - x_c^2}}{50.8}\right), \qquad (5.13)$$

$$\beta = \sin^{-1}\left(\frac{x_c}{RADIUS}\right) \; . \qquad (5.14)$$

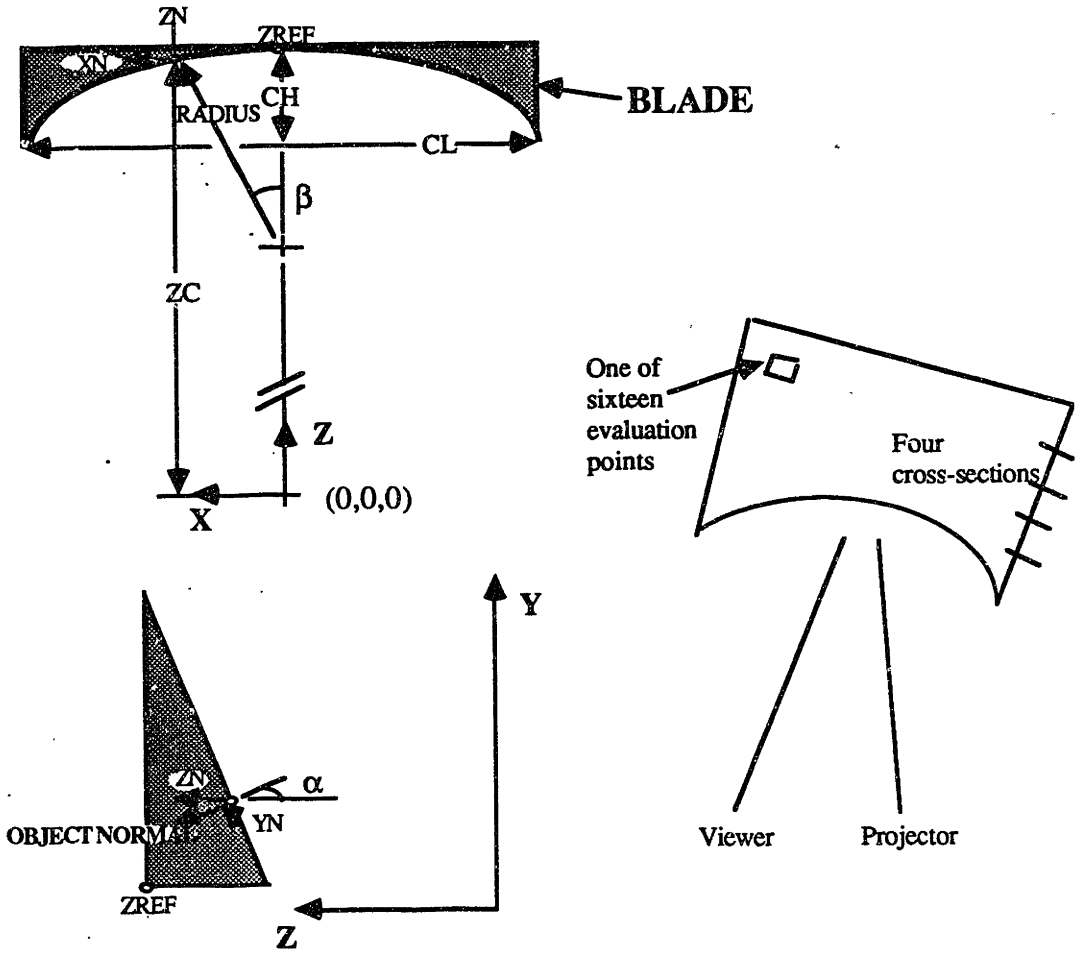

Figure 5.16: Object Similar to a Turbine Blade

The three object normals (x_n, y_n, z_n) are defined as

$$x_n = 1\sin\beta\cos\alpha, \tag{5.15}$$

$$y_n = 1\cos\beta\sin\alpha, \text{ or} \tag{5.16}$$

$$y_n = -1\cos\beta\sin\alpha \quad \text{if } \sqrt{RADIUS^2 - x_c^2} - RADIUS < 0.0 \tag{5.17}$$

and

$$z_n = 1\cos\beta\cos\alpha. \tag{5.18}$$

With the object defined, the grid optimization for the blade can take place.

5.5.2 Cost Function

The cost function defined in equation 4.13 and the output from the grid optimization program for this object are shown in Figure 5.17.

5.5.3 Equiorder Surface Plots

The equiorder surface plots for this object before and after optimization are shown in Figures 5.18 and 5.19 respectively.

5.5.4 Projecting and Viewing Grids

The optimized projecting and viewing grids are shown in Figures 5.20 and 5.21 respectively.

****
GRID OPTIMIZATION RESULTS - BLADE
****

COST= 0.8633196 # ITER= 3990.00

PROJECTING GRID CONTROL POINTS

1	2	3
8.181549	18.21753	28.47138
8.334944	18.05663	28.19461
8.620850	18.04202	28.17180
8.563906	17.91726	28.01119

VIEWING GRID CONTROL POINTS

1	2	3
8.237719	17.62327	29.19836
8.085158	17.15170	26.43070
7.900487	17.93613	27.89574
7.801102	16.59993	26.43694

EVAL #	FO	DISTANCE ERROR	SPACING
1	-4.471490	0.1859851	9.856049
2	-4.395091	0.9759585	10.10224
3	-4.565571	0.5879555	10.41627
4	-4.581667	0.7269715	10.00004
5	-4.439849	0.4994243	9.815905
6	-4.518945	9.2071690E-02	10.11561
7	-4.687314	1.856708	10.33005
8	-4.563330	0.5458617	10.06602
9	-4.417261	0.7233107	9.822911
10	-4.540171	0.3100559	10.11240
11	-4.669112	1.654713	10.25150
12	-4.511246	1.3434083E-02	10.15227
13	-4.653482	1.388835	9.605271
14	-4.633843	1.254074	10.00265
15	-4.625168	1.188594	10.16521
16	-4.504557	0.0000000E+00	10.15672

Figure 5.17: Cost Function and Grid Optimization Results - Object Similar to a Turbine Blade

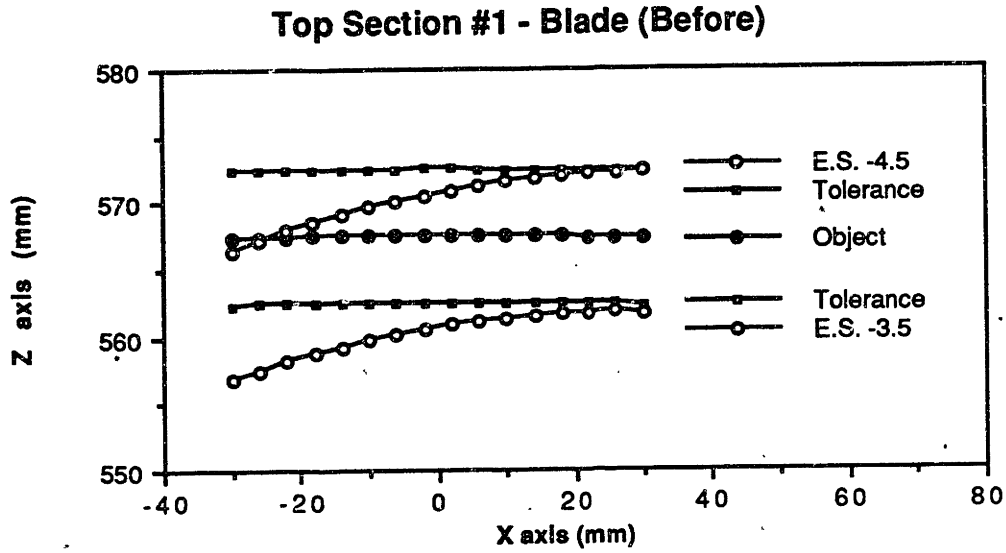

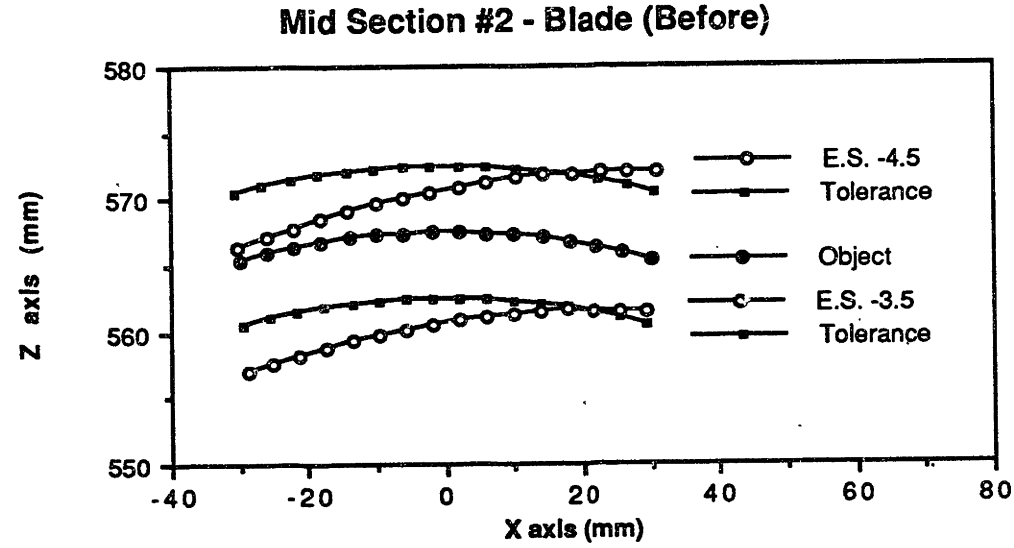

Figure 5.18: Equiorder Surface Plots - Before Optimization
Object Similar to a Turbine Blade

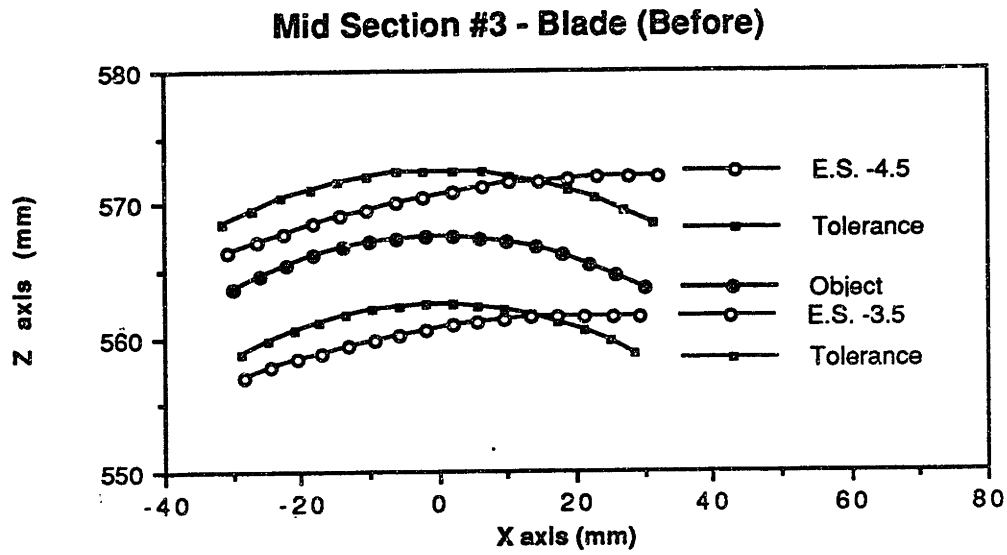

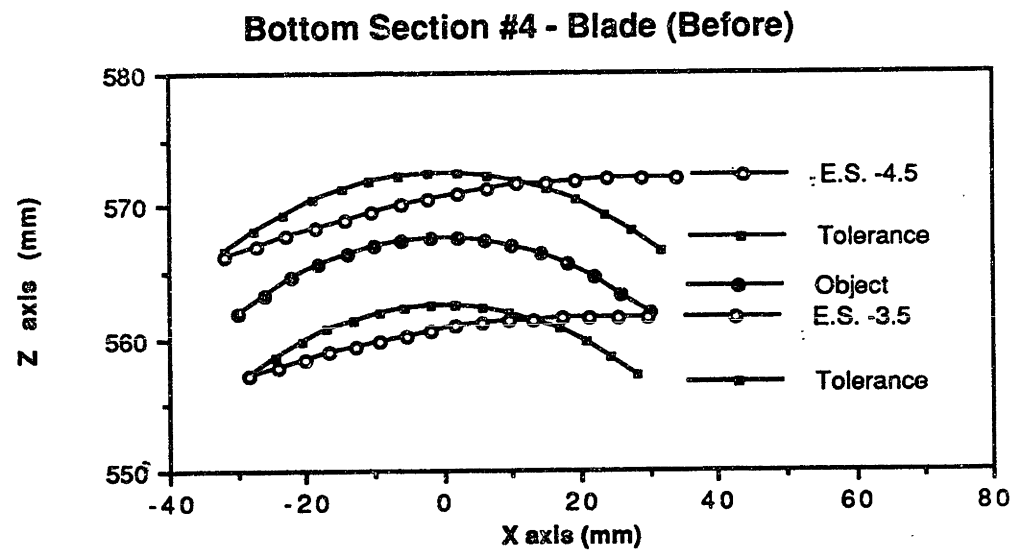

Figure 5.18 cont.: Equiorder Surface Plots - Before Optimization
Object Similar to a Turbine Blade

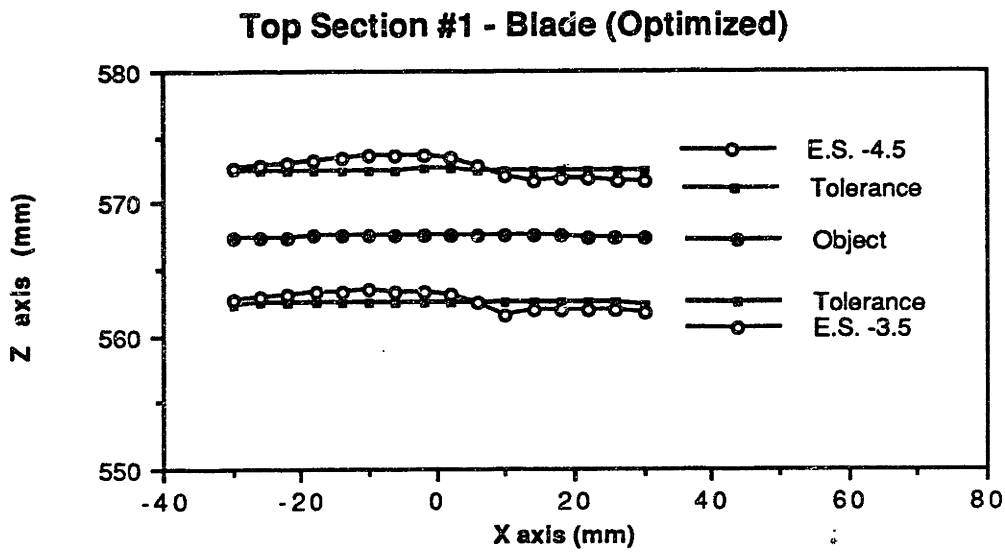

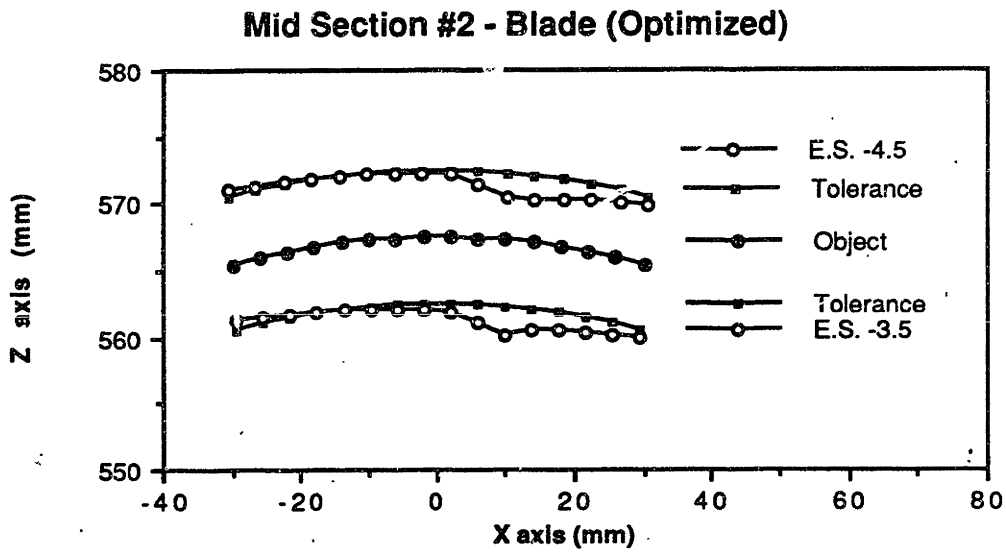

Figure 5.19: Equiorder Surface Plots - After Optimization
Object Similar to a Turbine Blade

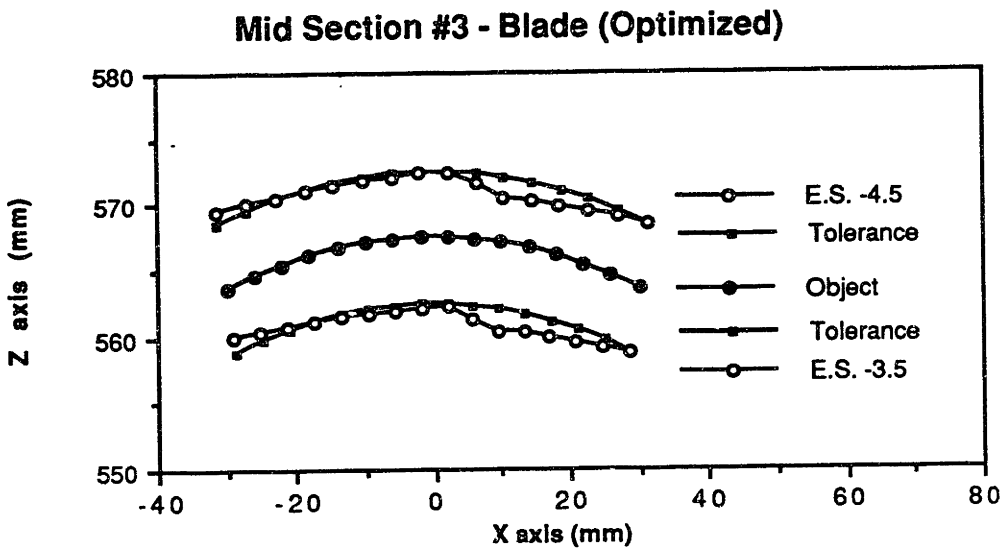

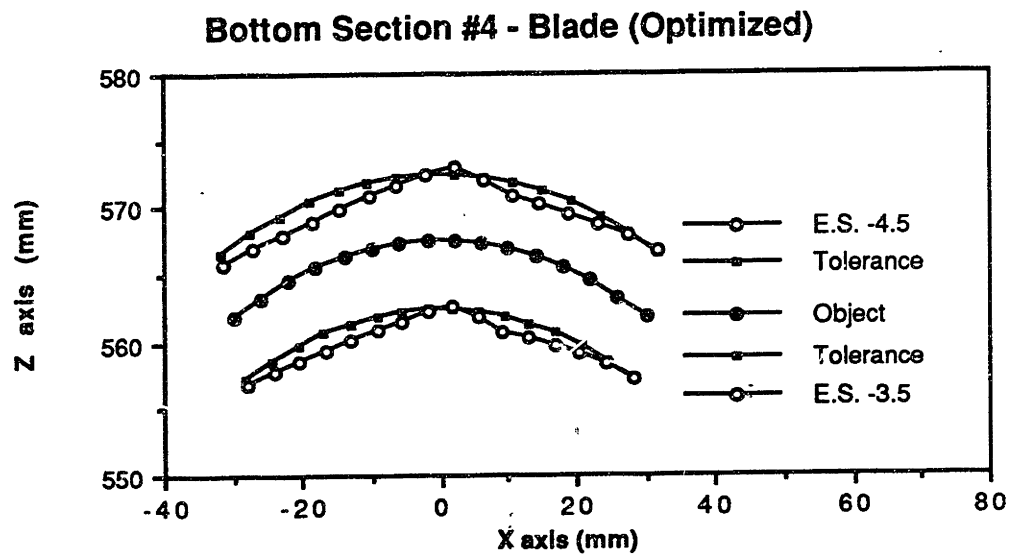

Figure 5.19 cont.: Equiorder Surface Plots - After Optimization
Object Similar to a Turbine Blade

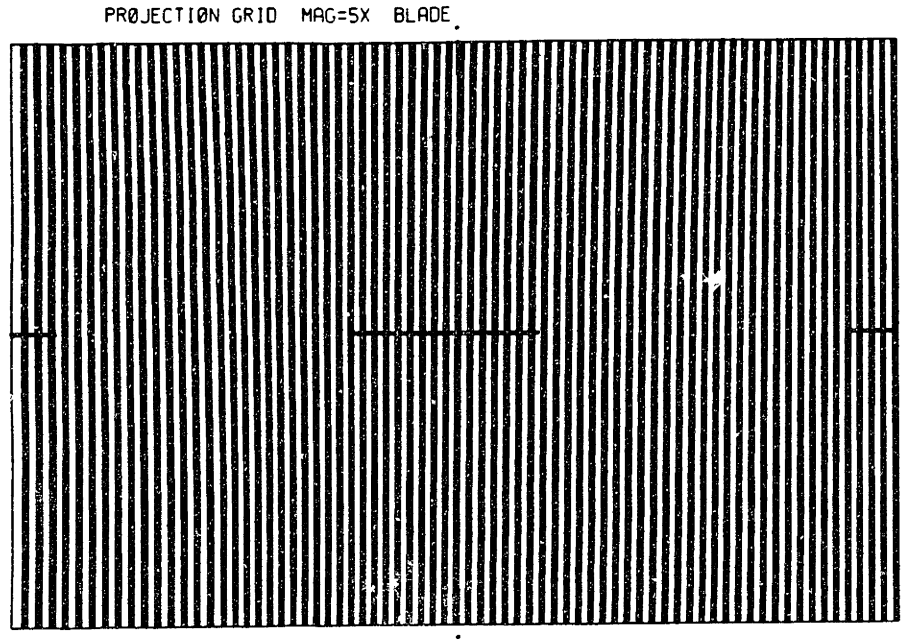

Figure 5.20: Projection Grid - Object Similar to a Turbine Blade

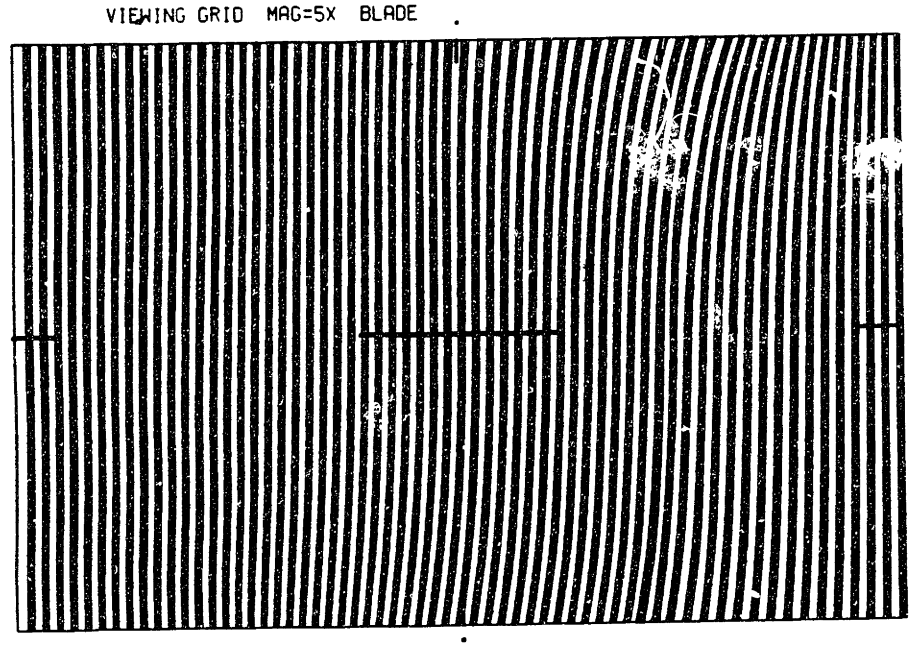

Figure 5.21: Viewing Grid - Object Similar to a Turbine Blade

5.6 Case 5: Object Similar to a Turbine Blade with Twist

5.6.1 Object Definition

Figure 5.22 shows the object configuration for theoretical inspection of an object similar to a turbine blade with some twist. The chord length, CL, is the object width and is equal to 76.2 mm. The chord height, CH, is a function of the height along the object:

$$CH = -\frac{\text{Base Chord Length}}{\text{Total Object Height}} * \text{Height Along Object} + \text{Base Chord Length} \qquad (5.19)$$

The radius of the object for this chord height is

$$\text{RADIUS} = \frac{CL^2}{8*CH} + \frac{CH}{2} \; . \qquad (5.20)$$

The y object points, y_c, are predetermined, equally spaced points on the object surface (Figure 4.1). The x and z object points, x_c and z_c, are found using the equations (refer to Figure 5.22):

$$\gamma = \tan^{-1}\left(\frac{\text{RADIUS} - \sqrt{\text{RADIUS}^2 - x^2}}{x}\right), \qquad (5.21)$$

$$\theta = \frac{\text{Height Along Object}}{5} \text{radians} = \text{twist of blade}, \qquad (5.22)$$

$$\text{DIST} = \sqrt{x^2 + (\text{RADIUS} - \sqrt{\text{RADIUS}^2 - x^2})^2} \; , \qquad (5.23)$$

such that

$$x_c = -\,\text{DIST} * \cos(\theta - \gamma) \qquad (5.24)$$

and

$$z_c = z_{ref} + \text{DIST} * \sin(\theta - \gamma) \; . \qquad (5.25)$$

The object angles α and β are defined by:

$$\alpha = \tan^{-1}\left(\frac{\text{RADIUS} - \sqrt{\text{RADIUS}^2 - x^2}}{50.8}\right), \tag{526}$$

$$\beta = \sin^{-1}\left(\frac{x}{\text{RADIUS}}\right). \tag{5.27}$$

The three object normals (x_n, y_n, z_n) are defined as

$$x_n = 1\sin(\beta + \theta)\cos\alpha, \tag{5.28}$$

$$y_n = 1\cos(\beta + \theta)\sin\alpha, \text{ or} \tag{5.29}$$

and $$z_n = 1\cos(\beta + \theta)\cos\alpha. \tag{5.30}$$

The twist in the object, θ, is approximately 10 degrees at the top of the blade. With the object defined, the grid optimization for the blade with twist can take place.

5.6.2 Cost Function

The cost function defined in equation 4.13 and the output from the grid optimization program for this object are shown in Figure 5.23.

5.6.3 Equiorder Surface Plots

The equiorder surface plots for this object before and after optimization are shown in Figures 5.24 and 5.25 respectively.

5.6.4 Projecting and Viewing Grids

The optimized projecting and viewing grids are shown in Figures 5.26 and 5.27 respectively.

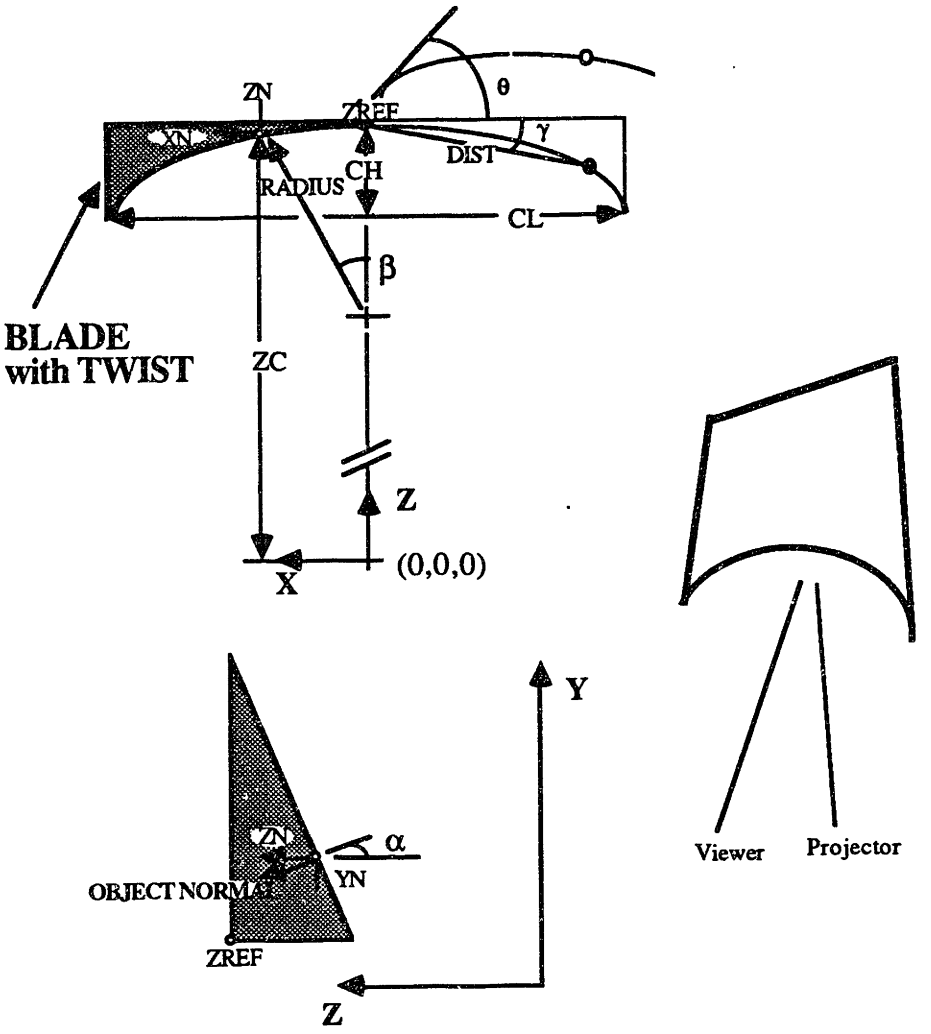

Figure 5.22: Object Similar to a Turbine Blade with Twist

****
GRID OPTIMIZATION RESULTS - BLADE W/TWIST
****

COST= 0.1652495 # ITER= 23061.00

PROJECTING GRID CONTROL POINTS

1	2	3
8.211411	17.85746	27.97567
8.314090	17.85044	28.04719
8.273876	18.23189	28.25714
8.710235	18.39341	28.62190

VIEWING GRID CONTROL POINTS

1	2	3
8.062284	17.20735	27.68762
8.004951	17.18541	27.17842
8.153462	17.44863	27.02657
8.447009	17.88903	27.00614

EVAL #	FO	DISTANCE ERROR	SPACING
1	-4.581639	0.7259425	9.968602
2	-4.456232	0.3459465	10.03974
3	-4.528126	0.1849633	10.02510
4	-4.508766	0.0000000E+00	10.03214
5	-4.476783	0.1330035	9.892849
6	-4.438978	0.5259572	10.11568
7	-4.523700	0.1400196	10.01496
8	-4.482590	7.6005057E-02	9.979941
9	-4.405209	0.8468775	9.847916
10	-4.469531	0.2110070	10.11509
11	-4.562659	0.5369402	10.02578
12	-4.480494	9.6916504E-02	9.977799
13	-4.365217	1.240957	9.840776
14	-4.539306	0.2989649	10.04553
15	-4.632607	1.251958	10.05861
16	-4.508341	0.0000000E+00	10.03126

Figure 5.23: Cost Function and Grid Optimization Results - Object Similar to a Turbine Blade with Twist

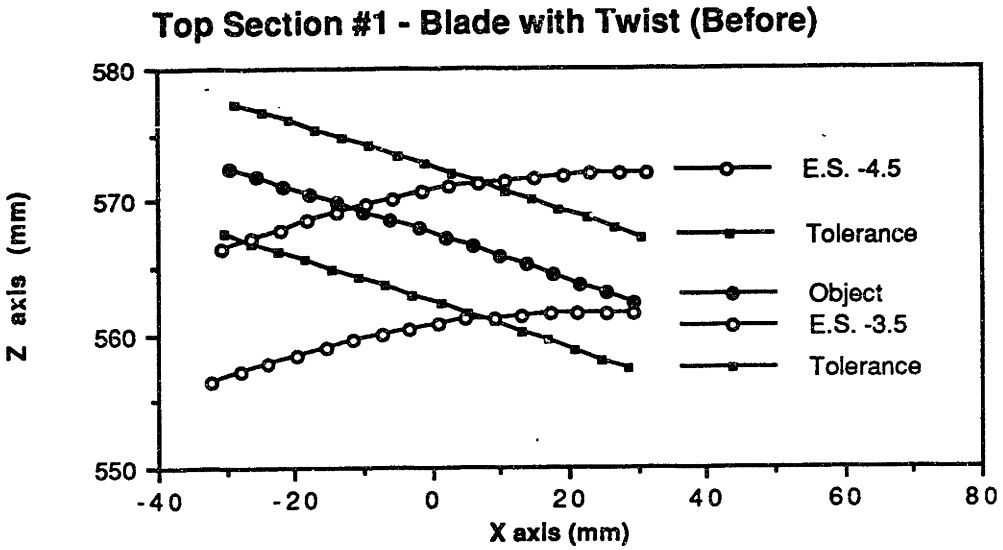

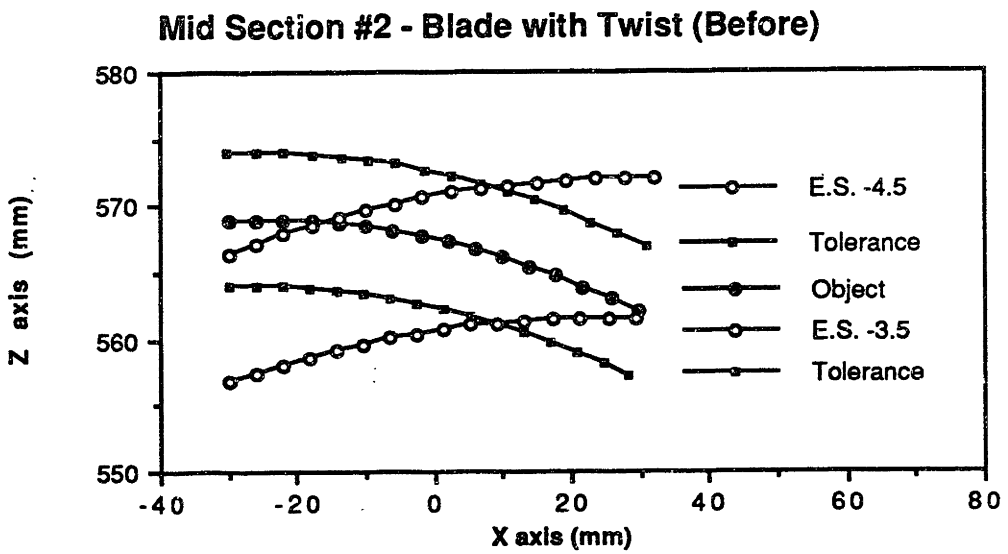

Figure 5.24: Equiorder Surface Plots - Before Optimization
Object Similar to a Turbine Blade with Twist

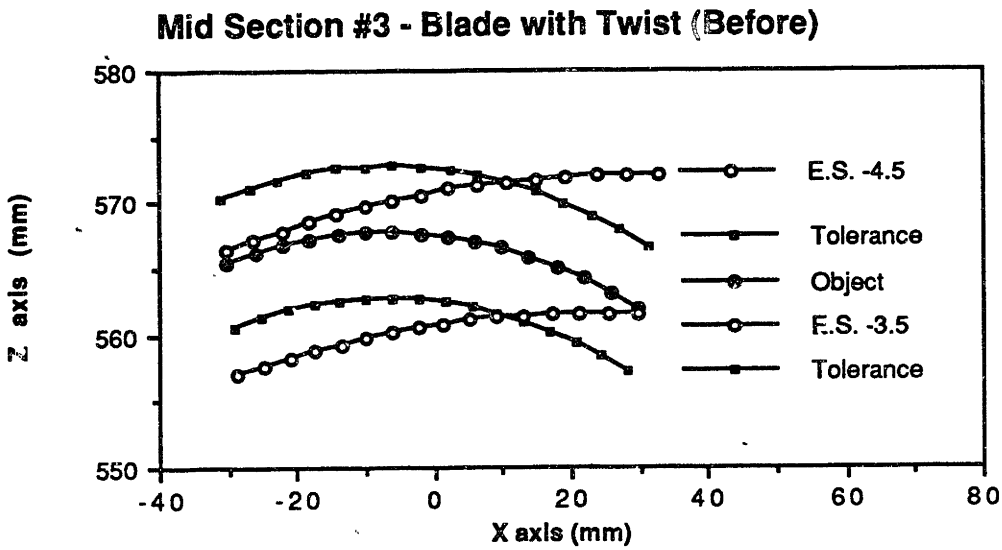

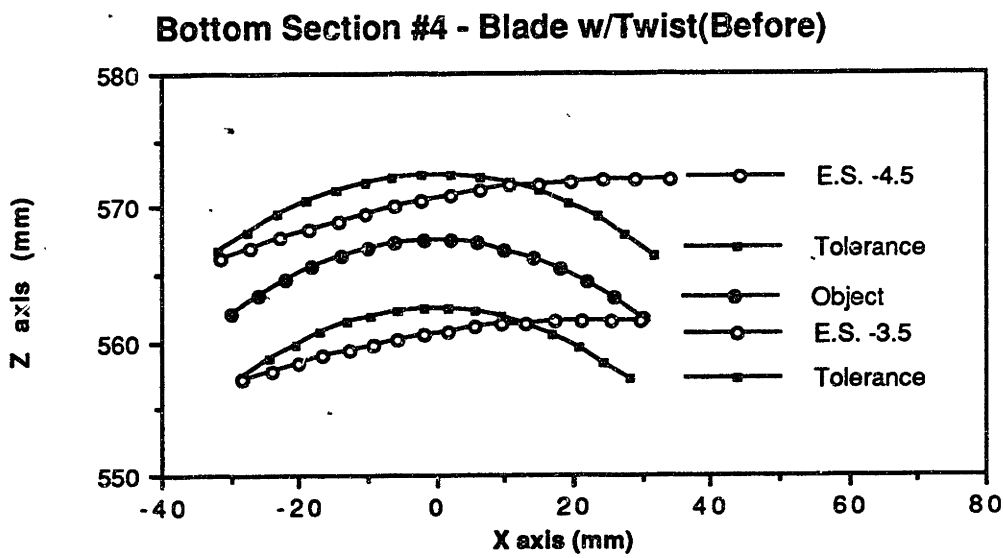

Figure 5.24 cont: Equiorder Surface Plots - Before Optimization
Object Similar to a Turbine Blade with Twist

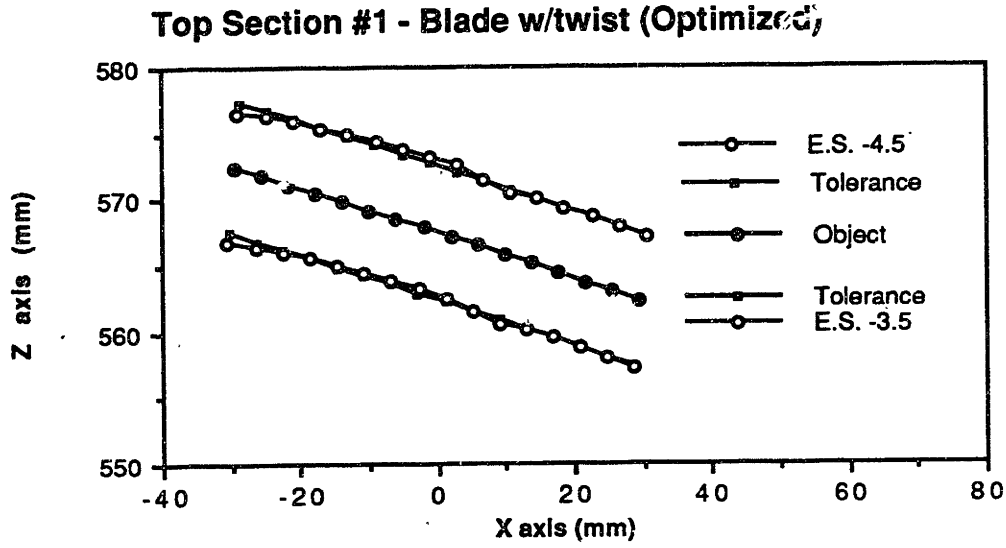

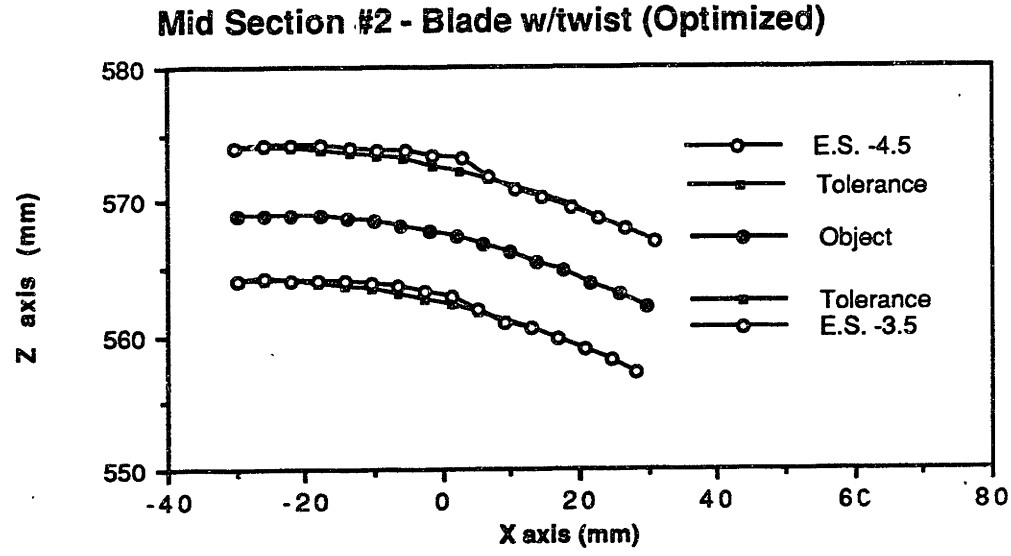

Figure 5.25: Equiorder Surface Plots - After Optimization
Object Similar to a Turbine Blade with Twist

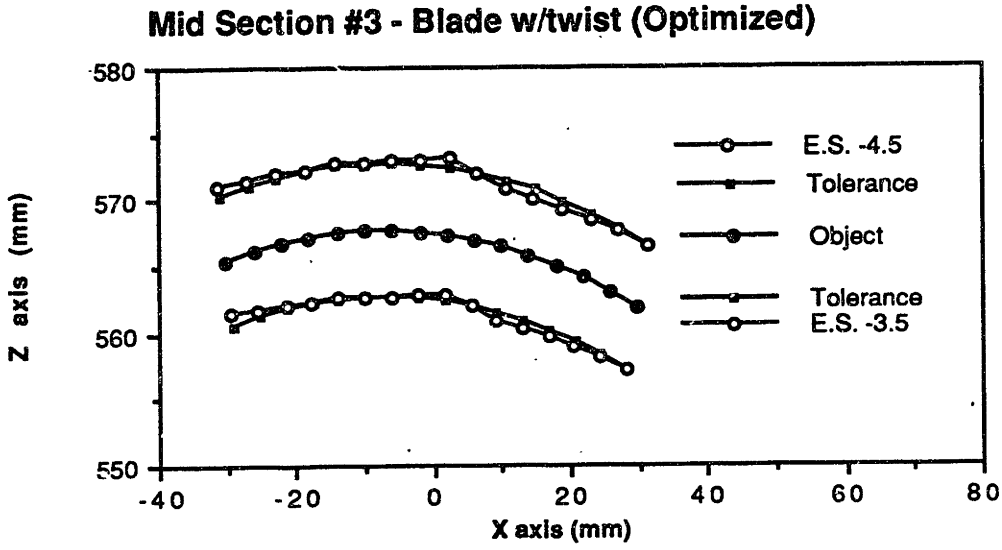

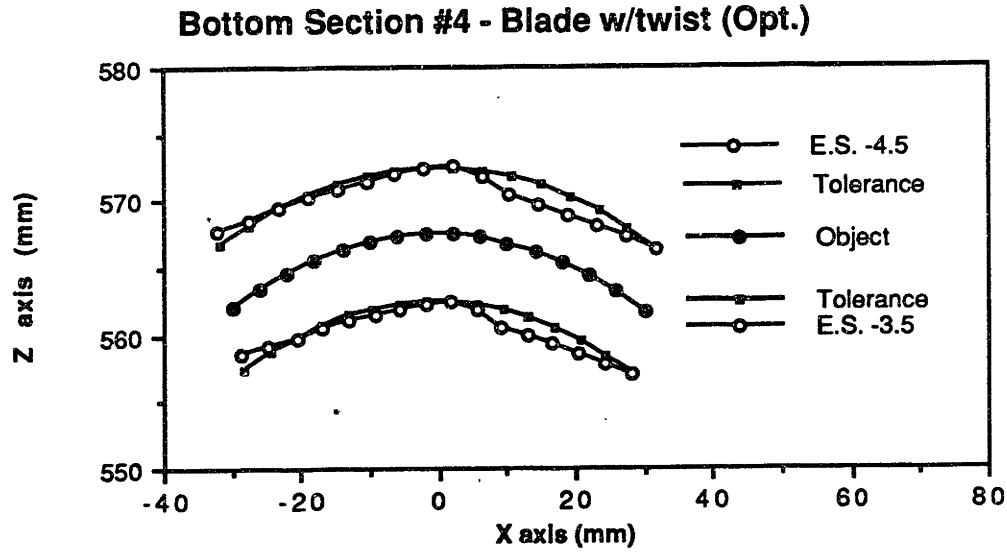

Figure 5.25 cont: Equiorder Surface Plots - After Optimization
Object Similar to a Turbine Blade with Twist

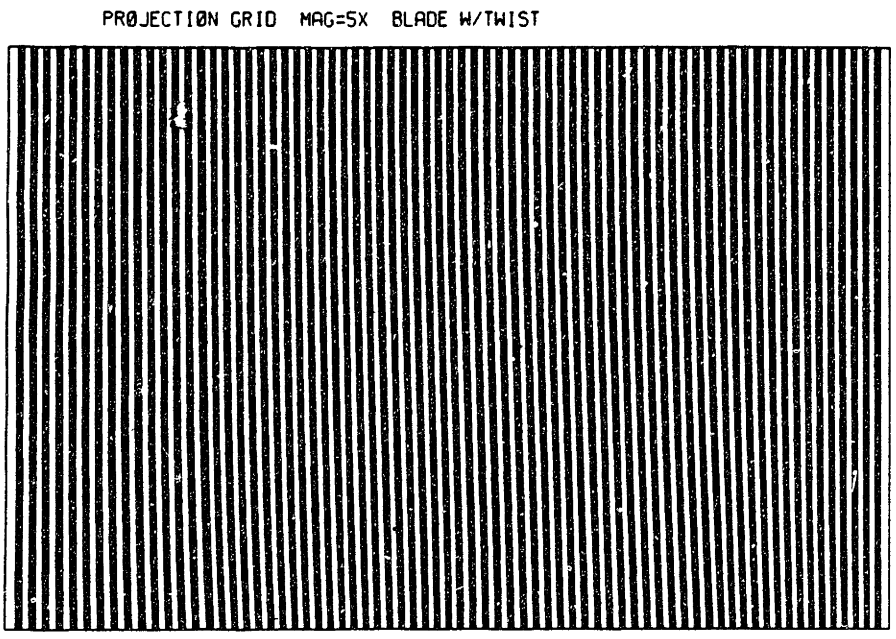

Figure 5.26: Projection Grid - Object
Similar to a Turbine Blade with Twist

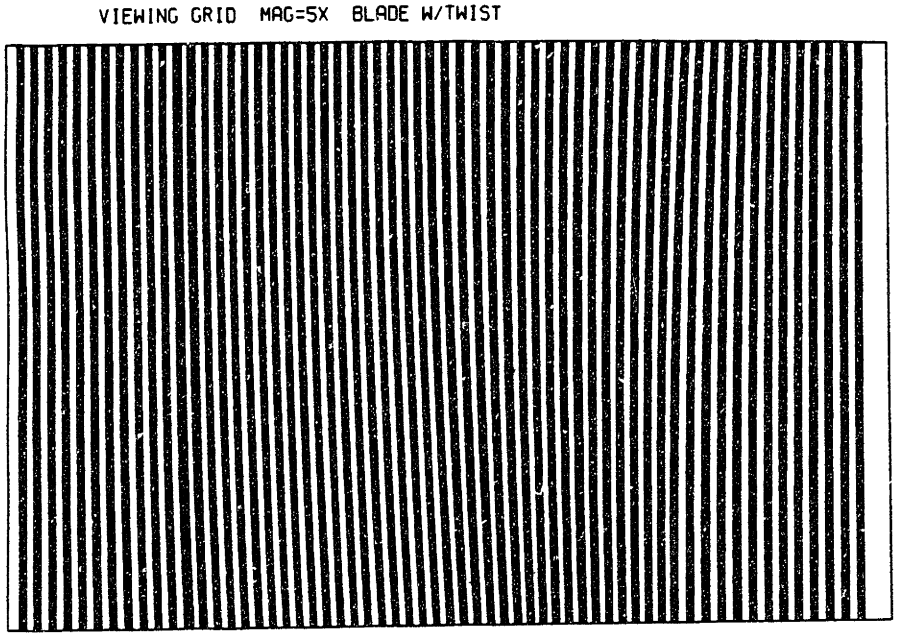

Figure 5.27: Viewing Grid- Object
Similar to a Turbine Blade with Twist

5.7 Discussion

The theoretical results indicate that this method of tailoring the equiorder surfaces is quite successful. Inspection of surfaces with a general curvature is feasible with this method. Each grid optimization run begins with control points defining straight line grids and the control points are varied in successive optimization runs until the cost function indicates the tolerance of the inspection is met. For the cases presented here, the optimizations were terminated when the minimum of the cost function was found and the distance errors from object tolerance surfaces and equiorder surfaces associated with fringe orders equal to an *integer* ± 0.5 were less than a few millimeters. The computation time for complete inspection of an object is a few days.

The great changes that occured from before to after optimization show the overall flexibility of the technique. As expected, the optimization of the object similar to equiorder surfaces obtained with straight lined grids resulted in a very low cost. This is a promising result for the development of this method. Note that the flat object was adequately inspected without implementing special geometry - contradicting the result of Moens [24]. The cylinder was by far the most difficult object to inspect because of its great curvature. The equiorder surface shape obtained with straight lined grids is relatively flat, thus, successive optimizations had to be made in the theoretical inspection of the cylinder. Note that the cost result is still quite low and that the spacing part of the cost function dominated this run. The blade was theoretically inspected with ease. Its gently sloping surface is similar to the equiorder surfaces from the start. The blade with some twist was also inspected easily.

A low frequency fringe image should be expected where the curve of the equiorder surfaces with fringe orders equal to -3.5 and -4.5 cross the object. One dark fringe is expected for the flat object before optimization. Two dark fringes are expected for the cylinder. In all optimized cases, no dark fringes should result. The flat and cylindrical objects were inspected with the physical system setup. The experimental results from before and after tailoring the equiorder surfaces are presented in Chapter 6.

6 EXPERIMENTAL RESULTS

6.1 Interferometer Setup

This chapter describes the experimental setup, procedure, and results. The experimental system was designed and built by Ruecker [33]. He describes the system calibration and testing procedure which I will go over briefly here. To reproduce the results contained in this chapter, the following procedure must be taken. The optimized interferometer parameters described in Chapter 3 are used to calibrate the system. First, the object location (0,0,567.5) is measured using a millimeter ruler. The projector location is measured to (-147.5,0,-50.0). The projection grid angle in Figure 2.1, ζ, is measured by using the laser positioning system. This system locates linear positions along the ruler lines (l,m) of the system to match the z-angle of the interferometer. The z-angle is shown in Figure 6.1.

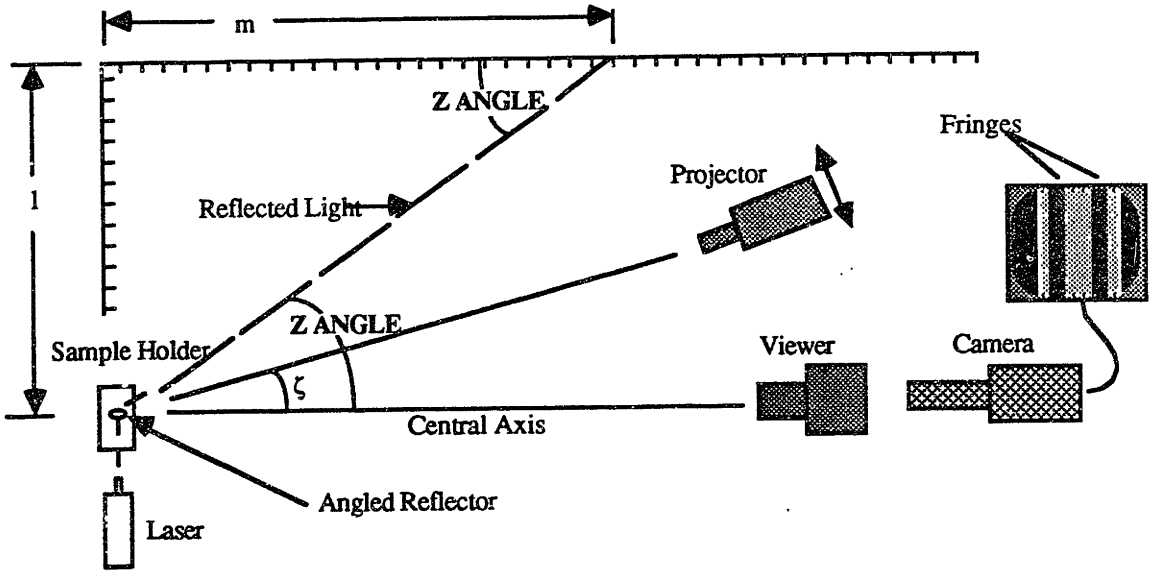

Figure 6.1: System Angular Configuration

The projecting and viewing axes are oriented with respect to a central axis. The sample holder consists of a frame and sample plate designed to hold the object. The viewer and projector are mounted on threaded rods so that they can be easily adjusted. The projecting axis can rotate with respect to the main axis. A description of the equipment making up the physical system is contained in Appendix A.

The object is positioned by inserting it into the sample holder. The holder is pivot mounted at the intersection of the projecting and viewing axes. A video camera is placed behind the image plane to view the fringe image. Projecting and viewing grids (vertical straight lines) with pitches of .5 and .58 respectively will reproduce the fringe images of the 'before optimization' results. The fringe image is seen on the vision system monitor. By aligning the sights of the projecting and viewing grids, the grid alignment is completed.

The system was measured to an accuracy of about 1/3 degree in ζ which corresponds theoretically to a shift of 17 mm in the z position of the equiorder surfaces. Contradictory to that is the physical effects of changing the ζ angle: little movement in equiorder surface position. This needs to be investigated further along with effects of other parameters on the sensitivity of the system. The system is pictured in Figure 6.2.

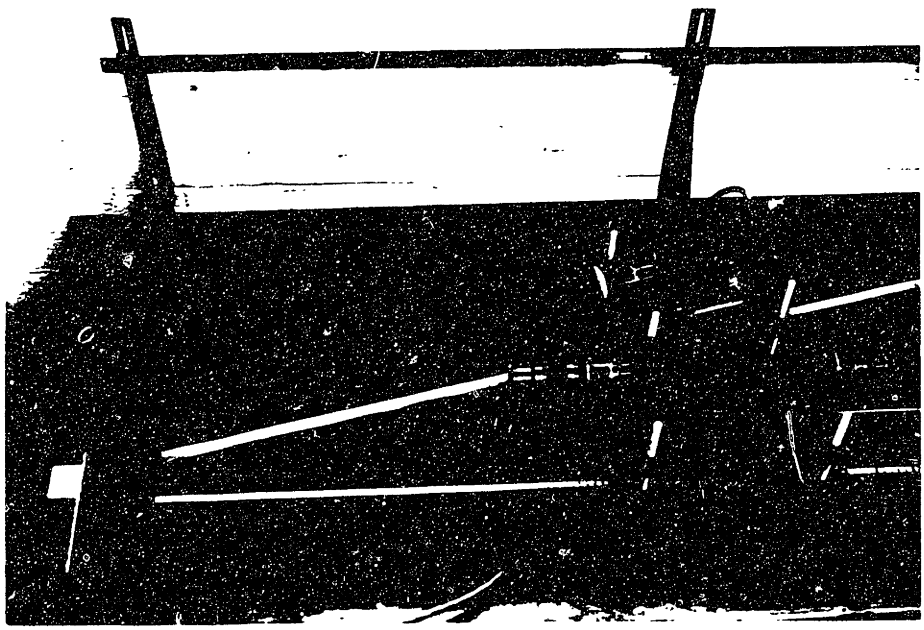

Figure 6.2: Physical System Setup

6.2 Preparation of Slides

A number of ways were investigated to produce the proper grids for experimentation. A proper grid requires a high contrast between light and dark lines. Industries typically use glass slides with a metal etching in order to achieve the desired effect. This process is often times too costly for experimental purposes; therefore, other methods were investigated including electrochemical etching, photochemical etching, laser cutting, metal slitting, photographical slides, milling, and electroforming [9,35]. Photographically producing slides was chosen because of it's simplicity, flexibility, and cost.

Photographically producing slides is easily done using a 35mm camera with a macro lens allows grid sizes to vary. Also, slide film and processing is economical. The Polaroid Polagraph 35mm instant black and white slide film with high contrast was used. It was easy to use and offered a higher contrast than standard black and white film. The film has a resolution of 90 line pairs per millimeter corresponding to a pitch of .011 mm which is more than sufficient for the grids generated by a standard laser printer with a minimum printing line width of .254 mm. Taking the pictures in bright, natural light on either automatic or manula mode produces good results. This kind of film is manually processed using the Polaroid Autoprocessor found at most professional camera stores.

Typical slides are plastic and tend to melt in the hot tungsten light projector. Glass mounts for the slides are small pieces of glass surrounded by a strong plastic. These also melt under the extreme heat of the projector. These problems were solved by manufacturing glass pieces that were cut to fit the interferometer. These glass pieces were created to house the plastic film. The film is sandwiched between two glass squares and then fused together either by a metal clip or by adhesive. This method has been found to be effective and inexpensive. However, there does exist a minor difficulty in positioning the slide.

6.3 Results

The results are pictures of the fringes observed on the vision system monitor during inspections with the objects described in chapter 5: a flat plate and a cylindrical object. These are the objects which could be physically manufactured within the research time frame of this project.

6.3.1 Flat Object

From the equiorder surface plots of Chapter 5, one fringe should be expected before optimization with the flat object. Figure 6.3 shows the fringe image resulting on the vision system. The image after optimization is shown in Figure 6.4.

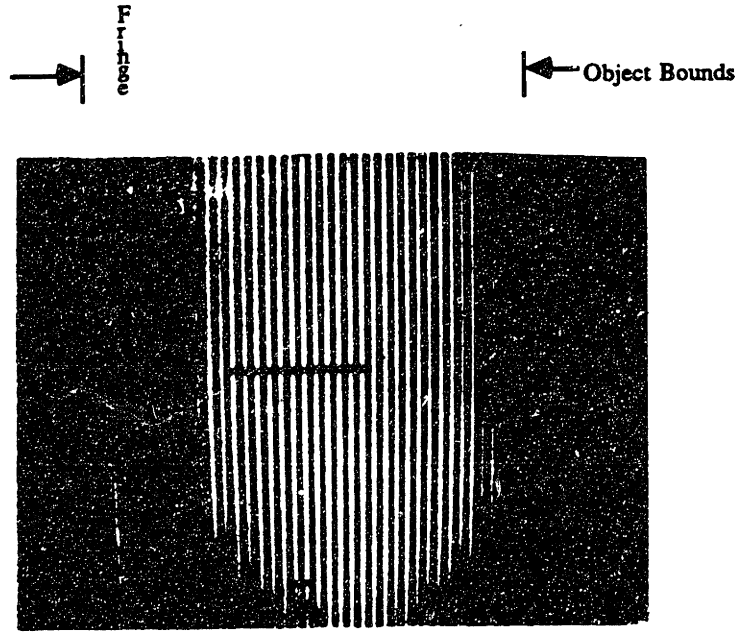

Figure 6.3: Vision System Image Before Optimization - Flat Object

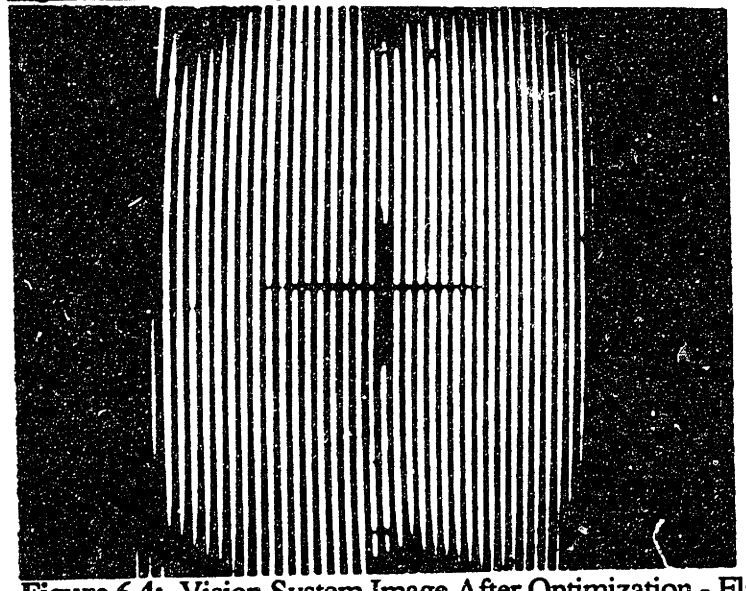

Figure 6.4: Vision System Image After Optimization - Flat Object

6.3.2 Cylindrical Object

From the equiorder surface plots of Chapter 5, two fringes should be expected before optimization with the cylindrical object. Figure 6.5 shows the fringe image resulting on the vision system. The image after optimization is shown in Figure 6.6.

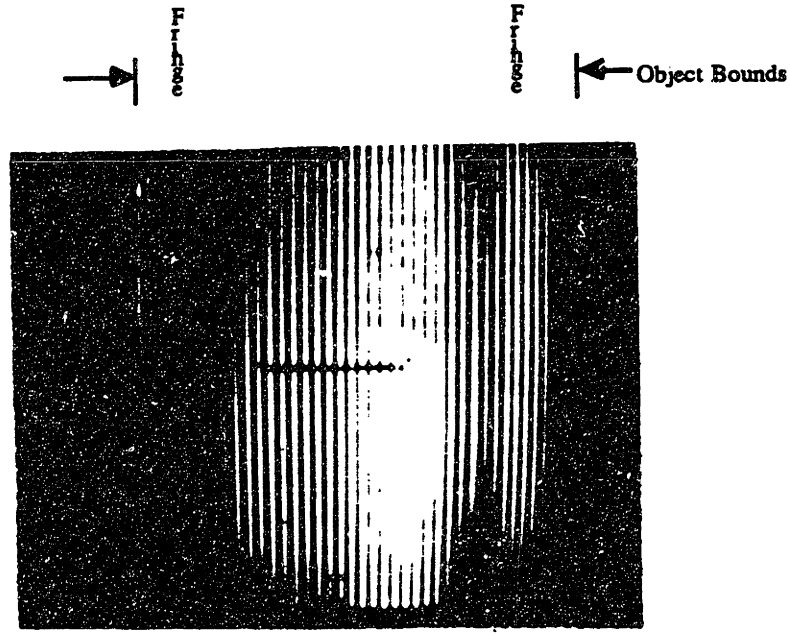

Figure 6.5: Vision System Image Before Optimization - Cylinder

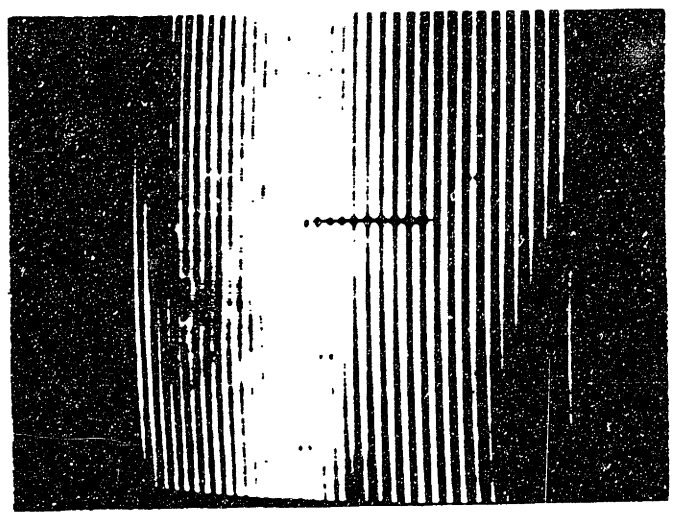

Figure 6.6: Vision System Image After Optimization - Cylinder

The results were verified by reconstructing the equiorder surfaces in another manner. A flat plate was positioned in the sample holder and the optimized grids for the cylinder were placed in the interferometer. By shifting the flat plate forward in a series of steps, the location of the dark fringes can be observed on the image plane and compared to the equiorder surfaces obtained theoretically. Figure 6.7 shows the comparison between theoretical and experimental equiorder surfaces obtained by this method.

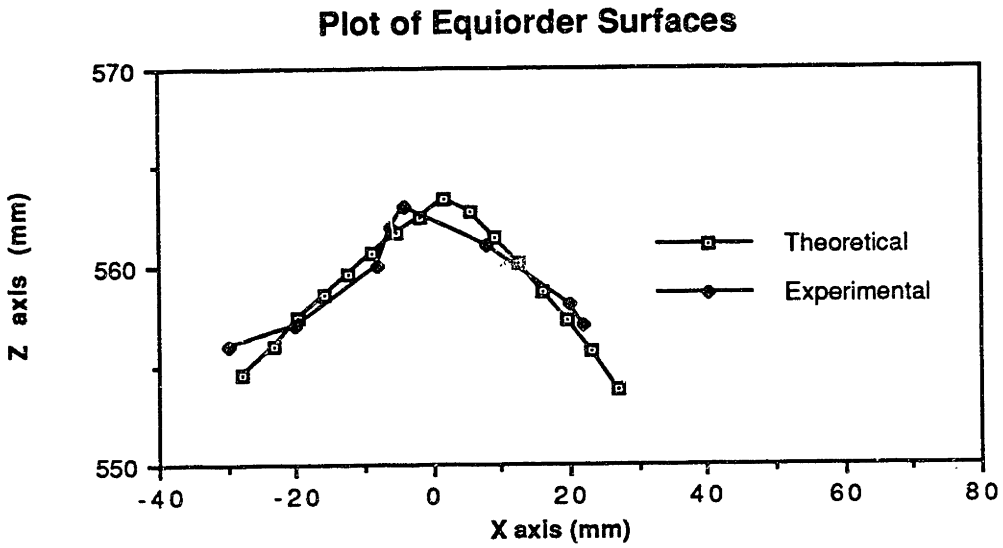

Figure 6.7: Theoretical vs. Experimental Equiorder Surfaces

6.4 Discussion

The experimental results match the theoretical results with success. However, there were some difficulties with the physical system. First, calibrating the system was difficult and resulted in inaccuracies in positioning the interferometer and grids. This resulted in difficulty in obtaining the correct fringe image. Note that the fringe is easiest seen when the fringes are moving. Secondly, the depth of field of the projecting lense is critical for inspection of objects with extreme curvature. By increasing the depth of field, the intensity of the light passing through the lense is decreased resulting in a poor fringe image at the image plane.

The system was tested against known theoretical cases and proved to work. This shows great promise for the technique in the inspection of surface form. With properly designed equipment, the system setup could be calibrated more easily.

7 CONCLUSIONS AND RECOMMENDATIONS

The method of tailoring equiorder surfaces presented in this thesis, the Method of Splines, is a promising technique for object inspection. By using the technique, Moiré interferometry as a method of inspection has been extended to inspection of surfaces with a general curvature. The technique is quite flexible and practical. Equiorder surfaces were shown to match a variety of objects under inspection. The grid optimization program is easily changed and allows a variety of inputs. Thus, the method is a great research tool in investigating Moiré interferometry phenomena. The experimental grids were photographically produced quickly and with little cost. A few questions still remain which, if answered, would strengthen the technique even further.

First, experimentally, the system needs to be calibrated in an accurate manner. With the present system, this is quite difficult. The system contains too many degrees of freedom which increase the time of calibration and accuracy of the system. A detailed analysis of the effects of the system parameters on the resulting equiorder surfaces should be performed. The system is very sensitive to too many adjustments. Also, the current method of sandwiching the photographic slides is coarse. A series of scribes or masks should be placed on the glass for positioning the slides. The depth of focus becomes a problem when the curvature of the object under inspection becomes great. Extension rings and high depth of field lenses should be used to insure the maximum light transmittance for high depth of field.

Theoretically, the time of computation for grid optimization was quite long. Other optimization techniques, such as a gradient method to find local minima, could be looked into to decrease the time of optimization. Other methods of tailoring equiorder surfaces could be investigated though the current method is quite flexible. One recommendation is that the interpolation between splines should be modified from the current linear method to a nonlinear method. This would decrease inconsistencies in grid plots and result in smooth transistions at principal spline control point regions.

BIBLIOGRAPHY

[1] Ahlberg, J.H., *Theory of Splines and Their Applications*, Academic Press, New York, 1967.

[2] Atkinson, B.M. and Heywood, P.W., "Automated Inspection - The Challenge of Vision", *Proc. 6th International Conf. on Automated Inspection and Product Control*, 1982, pp. 173-178.

[3] Bézier, P., *Numerical Control: Mathematics and Applications*, J. Wiley Press, New York, 1972.

[4] Box, M.J., "A Comparison of Several Current Optimization Methods", *Computer Journal*, Vol. 9, 1966, pp. 67-77.

[5] Brooks, R.E., and Heflinger, L.O., "Moiré Gauging Using Optical Interference Patterns", *Applied Optics*, vol. 8, no. 5, May 1969, pp. 935-939.

[6] Chiang, C., "Moiré Topography", *Applied Optics*, vol. 14, no. 1, 1975, pp. 177.

[7] De Boor, C., *A Practical Guide to Splines*, Springer-Verlay Press, New York, 1978.

[8] Dubowsky, S., "A New Approach for the Automated Inspection of 3-Dimensional Manufactured Parts", *The Seventh Israel Convention and Exhibition on CAD/CAM and Robotics*, Tel-Aviv, November 19-21, 1985 (invited keynote paper).

[9] *Electrochemical Machining*, edited by A.E. De Barr and D.A. Oliver, American Elsivier Publishing Co., Inc., 1968.

[10] Fox, R.L., *Optimization Methods for Engineering Design*, Addison-Wesley Publishing Co., 1971.

[11] Gasvik, K.J., "Moiré Techniques by Means of Digital Image Processing", *Applied Optics*, vol. 22, no. 23, 1983, pp. 3543.

[12] Guild, J., *Diffraction Gratings as Measuring Scales*, Oxford University Press, London, 1960.

[13] Harding, K.G., and Harris, J.S., "Projection Moiré Interferometer for Vibration Analysis", *Applied Optics*, vol. 22, no.6, 1983, pp. 856.

[14] Harding, K.G., and Tait, R., "Moiré Techniques Applied to Automated Inspection of Machined Parts", *Vision '86, Conf. Proc.*, June 1986, pp. 2-1.

[15] Hill, D.A., " The Measurement of Light for Inspection", *Proc. 7th International Conf. on Automated Inspection and Product Control*, March, 1985, pp. 219-230.

[16] Idesawa, M., Yatagi, T., and Soma, T, "Scanning Moiré Method and Automatic Measurement of 3-D Shapes", *Applied Optics*, vol. 16, no. 8, 1977, pp. 2152.

[17] *IMSL Library Reference Manual*, 9th Edition, International Math and Science Libraries, Houston, TX, 1982.

[18] Indebetouw, G., "Profile Measurement Using Projection of Running Fringes", *Applied Optics*, vol. 17, no. 18, 1978, pp. 2930.

[19] Lapidus, S., "New Techniques for Industrial Vision Inspection", Technical Paper MS84-162, MVA/SME, 1984.

[20] Leonard, R.J., *Application of Moiré Techniques to Manufacturing Inspection*, Master of Science Thesis, Department of Mechanical Engineering, MIT, 1985.

[21] Lord Rayleigh (John William Strutt), *Scientific Papers by Lord Rayleigh*, vol. 1, Dover Publications, 1964, pp. 1869-1881.

[22] McCollum, A.J., Batchelor, B.G. and Cotter, S.M., " Three-Dimensional Optical Sensing", *Proc. 7th International Conf. on Automated Inspection and Product Control*, March, 1985, pp.161-175.

[23] Meissner, L.P. and Organick, E.I., *Fortran 77*, Addison-Wesley Pub. Co., 1982.

[24] Moens, L., *Automated Three-Dimensional Inspection of Single Curvature Surfaces UsingMoiré Interferometry*, Master of Science Thesis, Department of Mechanical Engineering, MIT, 1987.

[25] *Moiré Array Experimental Patterns*, Dover Publications, 1986.

[26] Mortenson, M.E., *Geometric Modeling*, John Wiley & Sons, Inc., 1985.

[27] Murray, A.L., *Devolopment of Computer-Based Methods for the Design of Automated Inspection Systems Using Moiré Interferometry*, Master of Science Thesis, Department of Mechanical Engineering, MIT, 1986.

[28] Norris, M.A., *Spatially Optimal Path Planning for Robotic Manipulators with Obstacle Avoidance and Joint Motion Constraints*, Bachelor of Science Thesis, Department of Mechanical Engineering, MIT, 1985.

[29] Oster, Gerald, *The Science of Moiré Patterns*, Edmund Scientific Co., 1969.

[30] Powell, M.J.D., *Approximation Theory and Methods*, Cambridge University Press, New York, 1981.

[31] Reid, G.T., Rixon, R.C. and Marshall, S.J., " 3-D Machine Vision for Automatic Measurement of Complex Shapes", *Proc. 7th International Conf. on Automated Inspection and Product Control*, March, 1985, pp. 129-138.

[32] Rothbart, H.A., *Mechanical Design and Systems Handbook*, Magraw Hill, New York, 1985.

[33] Ruecker, L., "*Using the Moiré Testing Assembly* ", MIT Paper, 1988.

[34] Rustagi, J.S., *Optimizing Methods in Statistics*, Academic Press, New York,1979.

[35] Rykalin, N., Uglov, A. and Kokora, A., *Laser Machining and Welding*, Mir Publishers, Moscow, 1978.

[36] Schumaker, L.L., *Spline Functions: Basic Theory*, Wiley Press, 1981.

[37] Sikora, J., "Deflections of Rotating Marine Propellers Using Projection-Grating Moiré Techniques", *Experimental Mechanics*, December, 1981, pp.456-460.

[38] Simmons, J.P., Jr., "A Miniaturized Three Dimensional Vision System for Real Time Measurements", *Vision '86, Conf. Proc.*, June 1986, pp. 2-77.

[39] Strang, G., *Introduction to Applied Mathematics*, Wellesley-Cambridge Press, 1986.

[40] Sullivan, M., *A Demonstration of the Feasibility of a Moiré Fringe Based Method for Inspection*, Bachelor of Science Thesis, Department of Mechanical Engineering, MIT, June 1985.

[41] Tse, M.K., *Nondestructive Evaluation and Quality Engineering*, 1988.

[42] Wander, J.M., *The Application of Moiré Interferometry to Automated 3-Dimensional Inspection,* Master of Science Thesis, Department of Mechanical Engineering, MIT, 1985.

[43] Yokozeki, S., and Mihara, S., "Moiré Interferometry", *Applied Optics*, vol. 18, no. 8, 1979, pp. 1275.

APPENDIX A: Description of the Moiré Testing Equipment

The following equipment is part of the testing assembly:

- Newport MP1000 Moiré Projector and Viewer Rack with a matching Oriel 12V Transformer;
- Matsushita CPD Camera;
- Oriel 79253 He-Ne Gas Laser;
- Makinon 135mm 1:2.8 lens (Projector Lens);
- Vivitar 135mm 1:2.8 lens (Viewer Lens);
- Nikon PK-13 27.5mm extension rings.

The vision system atteached to the system is an Automatix Autovision II. In addition, supporting hardware such as cables, a power supply, and ruler markings used to calibrate the system are needed.